Master Thesis, c960370

Blood Flow in Microchannels

Lennart Bitsch

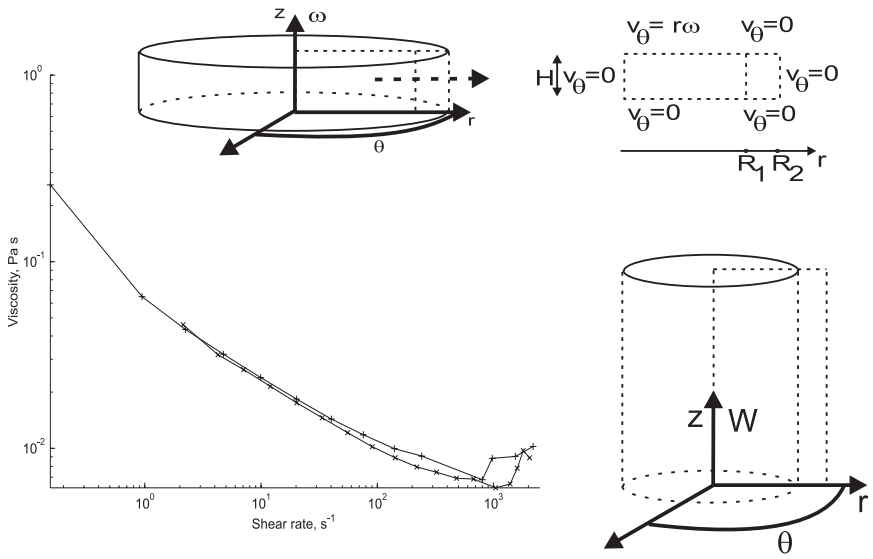

Supervisors: Henrik Bruus (1), Goran Goranović (1), and Peter Szabo (2)

(1) Mikroelektronik Centret - MIC
(2) Dansk Polymercenter/Institut for Kemiteknik
Technical University of Denmark

3rd September 2002

Abstract

Modelling of blood flow on the micrometer scale is a challenging task due to its non-Newtonian behavior, and because of the small dimensions which makes the continuum assumption problematic. The problem can be approached by the theory of generalized Newtonian fluids, where the apparent viscosity is described as a function of the scalar invariants of the shear rate tensor.

The present report contains a review on flow and rheological properties of blood. In this work the nonlinear character of the constitutive equation has been measured using a rotational rheometer. The measurements have been fitted to a simple power law model, and used as a constitutive equation for CFD-simulations in simple microtubes. By means of a parallel plate geometry, it was the intention to investigate how the viscosity depends on the gap size between the shearing plates. However, due to the instrument it was difficult to obtain reliable results at small gap sizes.

Resumé

Modellering af blodstrømme i mikrometerskala er en udfordrende opgave på grund af dens ikke newtonske opførsel, og de små dimensioner der kan gøre kontinuums antagelsen problematisk. Problemet kan tilnærmes vha. den generaliserede newtonske model, hvor den tilsyneladende viskositet er givet som en funktion af forskydningshastigheds tensorens invariante.

Denne rapport indeholder en oversigt over strømnings of reologiske egenskaber af blod. I dette arbejde er den ikke newtonske karakter af den konstitutive ligning bestemt vha. et rotations reometer. Målingerne er fitted til en simpel potens lov model, og er blevet brugt som en konstitutiv ligning til CFD-simuleringer i simple mikrorør. Vha. en parallel pladegeometri var det hensigten at undersøge viscositetens afhængighed af afstanden mellem den stationære og bevægelige plade. Eksperimentet var dog mindre succesfuldt.

Preface

This thesis is the product of eight months of study on blood; its morphology, its rheological properties and how it behaves in microchannels. My background for this project is five years of study at the Technical University of Denmark (DTU) and the University of Liverpool with a profile in chemistry and mathematical modelling.

The project was carried out at Mikroelektronik Centret (MIC) in collaboration with Dansk Polymer Center, both situated at DTU. Mikroelektronik Centret is a multidisciplinary research center based on a variety of different teams all working in the field of nano- and microtechnology. The two teams related to this project is the Micro Total Analysis System (μTAS), and Science & Education (S&E).

The μTAS group at MIC was founded in 1999, but in general μTAS refer to a concept of miniaturizing chemical analysis systems. However, as also will become evident from this thesis, miniaturizing is not just to scale down the system. In these small dimensions some physical concepts known from the macroscopic world cease to be valid.

In literature related to this subject, there are different traditions for handling the term *micro* as a prefix or a separate word. When we speak about, e.g., microchannels, microreactors and micromixers, we really mean components with length scales in the submillimeter range. However, as pointed out by Klavs Jensen [13], *micro* as a prefix does in general designate systems that originally were developed in the electronics industry. These techniques has later expanded to other fields like chemistry and biology. This integration has yielded a variety of advances that was not possible with the conventional techniques in the macroscopic domain. In accordance with many other authors, and to emphasize that we are describing systems related to this still expanding area of science, I will in this report use *micro* as a prefix, and write the words closed up. From this point of view, the Mikroelektronik Center was also designed to fabricate microelectronic devices, but the focus has merely changed to flow chips, analysis systems, and bio-arrays.

In the μTAS group a lot of ideas and designs have already emerged, on the basis of knowledge from scientists with various backgrounds, but until now a fundamental, theoretical understanding of microfluidic systems has been lacking. Hence, the S&E-team was involved to change the state of af-

fairs. A fundamental understanding of the system is necessary to circumvent some of the problems that emerge, when we scale down a system. For example, high shear rates can be damaging for living cells. How do we estimate this property, and are some designs more appropriate than others?

As a master student, it has been an exciting challenge to be on the forefront in this new field. Being a pioneer requires an ability to work independently, and it have sometimes been necessary to make decisions, where the knowledge on the outcome and consequences have been limited. Therefore, as I started this study, there were no well-defined problem, and this report reflects to a high extent how I worked through the project, and defined problems as I came along.

This project is a primer on blood studies at MIC and the polymer center, which means that nobody had any theoretical knowledge on blood rheology, or practical experience on how to handle blood in a laboratory. Accurate experiments requires a certain amount of experience. How do we measure hematocrit, how do we avoid that the cells are sticking to the pipette wall, and how do we prevent hemolysis?

To get advice on how to perform experiments with blood, I have taken contact to Poul Bennekou and Lars Ole Simonsen from the August Krogh Institute at the University of Copenhagen, as they handle blood routinely in their laboratories. Even though my experimental work has been relatively simple, and has ignored some of the problems mentioned, the discussion has been very supporting through the entire process. The collaboration has been extended to more than the practical issue of blood in the laboratory, and I am very thankful for the support, ideas and inspiration they have provided.

In general, this collaboration is a good example of cross-disciplinarity, which is an important factor for the success in developing microfluidic systems. Engineers have the knowledge on how to design and fabricate devices. Pharmacologist and physiologists have an insight into the living organism, and the experience to locate what is actually valuable information.

MIC is now about to establish a theory group on micro- and nanofluidics. Led by my supervisors, Henrik Bruus and Goran Goranvić, *Modelling of Blood Flow in Microchannels* is one of four in the first batch of master theses in the simulation group. I started up along with three other students, Mads Jakob Jensen, Anders Brask, and Flemming Rytter Hansen, each with their own defined projects. Their topics were *Bubbles in Microchannels*, *Principles of Electroosmotic Pumps*, and *Dispersion in Electrokinetically and Pressure Driven Microflows*, respectively. All together these four topics are concerned with a very central part of simulations on microfluidics, and should form a solid basis for future work at MIC. Their support and sharing of knowledge have been a great advantage for the thesis, and invaluable for keeping up the spirit during the project. I would like to address a special thanks to Goran Goranović who persuaded us to write these theses at MIC, and who set up the initial frame for this project. Also a thanks to Peter Szabo and Dansk

Polymercenter/Institut for Kemiteknik who provided the facilities for the rheological study.

Again, I wish to thank my supervisors at MIC and the Polymer Center for their patience, and willingness to discuss my problems, occasionally on unappropriate times.

Contents

List of Figures

Notations and Symbols

Vectors are denoted by boldface roman as for example the velocity vector, $\mathbf{v}$. For computational purposes a vector can be represented as a sum,

$$\mathbf{v} = \sum_{i=1}^{3} v_i \hat{\mathbf{k}}_i, \tag{1}$$

where $\hat{\mathbf{k}}_i$ is the unit vector in the ith direction. Second order tensors are distinguished by boldface greek. The dyadic product between two vectors is also a tensor for example,

$$\begin{aligned} \mathbf{vv} &= \sum_{i=1}^{3} v_i \hat{\mathbf{k}}_i \sum_{j=1}^{3} v_j \hat{\mathbf{k}}_j \\ &= \sum_{i=1}^{3} \sum_{j=1}^{3} \hat{\mathbf{k}}_i \hat{\mathbf{k}}_j v_i v_j. \end{aligned} \tag{2}$$

$\hat{\mathbf{k}}_i \hat{\mathbf{k}}_j$ is the unit dyad, and should not be confused with the dot product $\hat{\mathbf{k}}_i \cdot \hat{\mathbf{k}}_j = \delta_{ij}$.

A: Hamaker constant. The Hamaker constant has a typical value between 10^{-19} and 10^{-20} J [18].
D: diffusion constant
$\mathbf{F}$: force vector
G: relaxation modulus in oscillatory flow
k: Boltzmann constant 1.38066×10^{-23} J/K
$\hat{\mathbf{k}}_i$: unit vector in the i-direction
$\hat{\mathbf{k}}_i \hat{\mathbf{k}}_j$: the unit dyad
M: Young's modulus
N_A: the Avogadro constant $6.02 \times 10^{23}\,\mathrm{mol}^{-1}$
$\dot{Q}$: volume flow rate.
$\mathbf{S}$: vector for volume forces
$\mathbf{v}$: velocity vector
T: absolute temperature

$\mathcal{T}$:torque
x_i: coordinate on the ith axis
δ_{ij}: The Kronecker delta
ζ: ζ-potential
η: non-Newtonian viscosity
η^*: complex viscosity in oscillatory flow
λ: parameter for relaxation time in oscillatory flow, and viscosity parameter in the Power Law(Blood) model.
μ: Newtonian viscosity
ϕ: phase factor in oscillatory flow
ρ: density
ω: angular velocity
Ω: frequency in oscillatory flow

Chapter 1

Introduction

The concept of a micro total analysis system (μTAS) is not just to miniaturize conventional chemical systems, but also to take advantage of new features that emerge when we go to the microrange, or even smaller dimensions. A μTAS is assembled of units with different operations such as micropumps, micromixers, microreactors, and detecting units.

The key idea of a microfluidic system analyzing blood is: A blood sample comes in, gets analyzed, and a result comes out. In order to develop these systems, it will be necessary to establish mathematical models describing the transport of blood, and this thesis is a primer at MIC on this topic.

Microfluidics is a multidisciplinary field of research, and as a consequence this project is overlapping with two different areas. Firstly, the project involves experimental work with blood in a laboratory, which requires some knowledge on blood's physiological properties. Secondly, we have blood's rheology, and numerical simulations on flow in simple channels.

1.1 The structure of the thesis

According to the British Society of Rheology, rheology can be defined as the science of deformation and flow of matter, where fluids exhibiting Hookean and Newtonian behavior are excluded. In the study of blood flow the literature can be divided into two main classes; one is concerned with the rheological properties of blood in microchannels and capillaries, and the other is focused on how blood constitutive parameters can be related to the physical condition of a patient.

In *Biomechanics* Fung [10] outlines how a given biomechanical problem, such as the one at hand, could be studied. As mentioned, this study is concerned with the flow of blood not in a biological system, but in small channels and gaps of a material, which is not a natural environment for blood. However, even though our problem is not purely biological, Fung's approach is very general, and will therefore serve as a rough guideline in this

study. The following list is a modification or refinement of the tasks, that should be considered in a biomechanical study.

1. Study the morphology of the chosen geometries. What kind of material is it, and what are the dimensions?
2. Find or determine the mechanical properties of blood. Do they depend on shear rate, composition, time, and the surrounding material.
3. Based on the fundamental laws, establish the set of governing equations.
4. Set realistic boundary and initial conditions. Even if the problem is steady, appropriate initial conditions can be crucial in obtaining a converged solution.
5. Test the result with real experiments.
6. If necessary, refine theory or experiments.
7. If theory and experimental work is in agreement, consider consequences and applications.

In this chapter we will take a look on the phenomenology of non-Newtonian liquids to get a qualitative understanding of what kind of flows we might expect. In Chapter 2 we will introduce the underlying physics of fluids and how we in general can analyze and express a system in a mathematical model.

After two preliminary Chapters we will follow Fung's model more directly. In Chapter 3 we study the morphology and rheology of blood, in relation to flow in geometries in the submillimeter range. With background in this study we will in Chapter 4 investigate the flow properties further, as we perform our own measurements with a rotational rheometer. Our approach to the problem is the continuum assumption, where blood is regarded as a homogeneous fluid, and in microtubes this assumption can be a problem.

In very small tubes, blood can be modelled by considering individual cells, but in tubes with $100\,\mu$m in diameter and a large number of cells this approach would not be appropriate. Therefore, one of the objectives of the work was to investigate down to what size the continuum assumption would be a good approximation, i.e., in how small channels can we model the flow by means of a constitutive equation?

Unfortunately, these experiments turned out to be more difficult than expected. Measurements of rheological parameters at small dimensions requires an instrument with a very high precision. During the experiments it was discovered that the rotational plate was slightly skewed. Therefore, this

method was not appropriate to investigate gap size dependence, but we did obtain a macroscopic constitutive equation. When the measurement technique is not appropriate, it is necessary to search for alternative methods. A possible way of obtaining more reliable measurements, is also presented in Chapter 4.

In Chapter 5 we use the obtained constitutive equation to model a blood flow in a simple tube. Furthermore, our model is compared with results from other studies on blood flow in micro channels.

Even though the experimental part was not quite successful, I will round off this report by looking at some of the opportunities in microfluidic systems analyzing blood. Systems where a thorough understanding of fluid dynamics and mass transport in microsystems will be a helpful tool in the realization process.

1.2 Phenomenology of non-Newtonian liquids

Blood is known to be a non-Newtonian fluid. The distinction between Newtonian and non-Newtonian fluids is based on Newtons law of viscosity

$$\boldsymbol{\tau} = \mu\dot{\boldsymbol{\gamma}}, \tag{1.1}$$

where μ is the Newtonian viscosity, τ is the shear stress, and $\dot{\gamma}$ is the shear rate. The properties are measured in Pa s, Pa, and s^{-1}, respectively. If a fluid obeys Eq. (1.1) it is Newtonian. A central concept in rheology is the shear rate tensor. The shear rate is a measure for the deformation of a fluid, and in technical terms it is the gradient of the flow field

$$\dot{\boldsymbol{\gamma}} = \frac{1}{2}\left(\boldsymbol{\nabla}\mathbf{v} + (\boldsymbol{\nabla}\mathbf{v})^{\mathbf{T}}\right), \tag{1.2}$$

where $\mathbf{v}$ is the velocity vector and superscript T denotes the transposed. The term fluid has a different meaning in different fields of science, but in continuum mechanics we mean matter that is able to flow. According to Probstein [18] the non-Newtonian liquids can be categorized as follows:

1. Time-independent fluids in which the shear stress is a nonlinear one-to-one function of the shear rate.

2. Time dependent fluids in which the shear stress is not a one-to-one function of the shear rate, but depends on the shear stress history of the fluid.

3. Viscoelastic fluids that have both viscous and elastic properties in which the shear stress depends upon both the shear rate and strain. The elastic character introduces a time-dependent behavior or "memory" to such fluids.

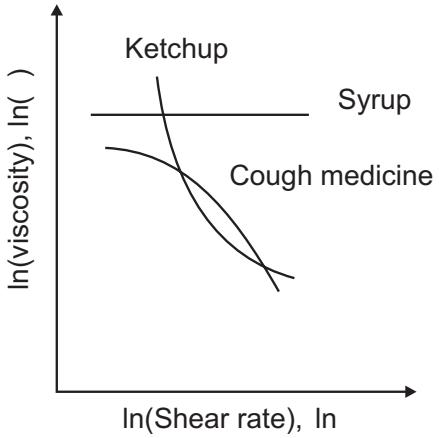

Figure 1.1: The figure shows the viscosity for fluids known from everyday life. For syrup, a Newtonian fluid, it is obvious that if the shear rate is swept up and down the viscosity function will fall on the same line, hence, the constant viscosity is time-independent and a one-to-one function. For ketchup and cough medicine, non-Newtonian fluids, the viscosity is not constant, but if the reverse sweep gives the same curve, then it is also a time-independent, one-to-one function. The curves are only intended to show characteristics, and the figure is just a redraw from Responses' homepage [19].

.

The first group concerns the so-called generalized Newtonian fluids for which the material properties are independent of time. By a one-to-one function is meant a function which assigns only one function value to each value of the independent variable. For the generalized Newtonian fluid, the viscosity is a one-to-one function of the shear rate. In the case of linearity between the shear rate and shear stress, the fluid is Newtonian.

Figure 1.1 shows trends of viscosities for different materials known from the everyday. Ketchup and cough medicine are both dependent on the shear rate, but the plot does not show anything about time or history dependence. To get this kind of information we would need to perform consecutive measurements. If the curves are not coinciding, the shear stress is dependent on time or shear rate history.

Syrup is a Newtonian liquid, and, therefore, the viscosity remains constant as the shear rate is changed. Evidently, syrups viscosity is a time-independent, one-to-one function. To get a better feeling for the consequences of non-Newtonian behavior it can be instructive to think about ketchup. When we dip a chip in ketchup the applied stress is high and the viscosity of the fluid is low. As the chip is moving from the ketchup towards the mouth the shear stresses are low, and the viscosity high. Therefore, the ketchup does hopefully not drip on the shirt.

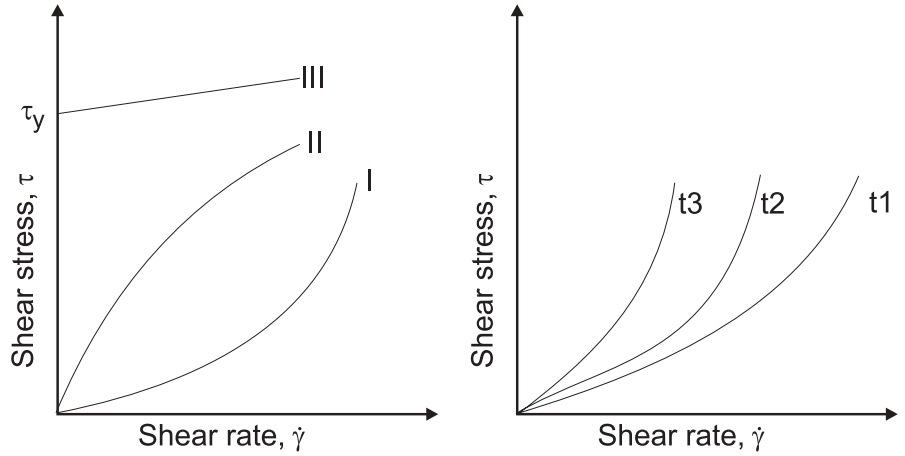

Figure 1.2: Illustration of different non-Newtonian properties. Panel (a) shows three fluids: (I) a shear thickening , and (II) a shear thinning liquid. Curve (III) is for a Bingham fluid, where τ_y is the yield stress [18]. Panel (b) shows the characteristic behavior of a rheopectic fluid. The shear stress is seen as a function of the shear rate for different times $t_1 < t_2 < t_3$. The viscosity, the slope $\eta = d\tau/d\dot{\gamma}$, is increasing with time.

To illustrate the nature of generalized Newtonian fluids, three distinct cases are represented in Fig. 1.2(a). Depending on whether the viscosity is increasing or decreasing, the fluid is said to be shear thickening (I) or shear thinning (II). The apparent viscosity is found as the slope of the shear stress shear rate plots. The curve labelled (III) represents the Bingham fluid model. This kind of material has properties of both a solid and a Newtonian liquid. When the applied stress is below some critical value denoted the yield stress $\boldsymbol{\tau_y}$, the material obeys Hooke's law, which in general applies to small deformations in solids. Hooke's law states that

$$\boldsymbol{\tau} = M\boldsymbol{\gamma}, \tag{1.3}$$

where $\boldsymbol{\gamma}$ is the strain and M is Young's modulus. If, however, the yield stress is exceeded, we observe a fluid flow. The cases are to be thought of as characteristics, and one fluid can easily exhibit more than one of the mentioned behaviors.

The second group involves shear stress functions that are not single-valued with respect to the shear rate. These are systems with a relatively long relaxation time, which implies that two following measurements of the shear rate yields different results. The viscosity is dependent on time and shear history.

If the viscosity increases with time, the fluid is rheopectic. Conversely, if it is a decreasing function of time, it is thixotropic. This same classification

is used if the change in viscosity is due to the applied stress. The important thing is that the viscosity remains changed for a measurable time, when the stress is turned off. Figure 1.2(b) shows the typical characteristics for a rheopectic fluid.

The last group is described as viscoelastic fluids. This property is often observed for concentrated polymeric solutions. In synthetic polymer solutions the long and branched molecules have very strong interactions, and will therefore pull in each other when a large stress is applied; this is the reason for the elastic behavior. For smaller shear rates, the molecules have time to relax, and have in this way also a viscous behavior. A qualitative difference between a Newtonian and a viscoelastic fluid can be observed in the case of a sudden contraction. For the Newtonian liquid the streamlines will go straight into the narrow channel, whereas a vortex develops in the case of a viscoelastic fluid. The phenomenon was studied by Giesekus for an aqueous polyacrylamide solution at a low Reynolds number. This particular and other interesting features of non-Newtonian liquids is reviewed by Bird et al.[3].

At the close of this section, we will take a look on two different classes of non-Newtonian fluids, and briefly list some of the other properties that influence the flow behavior. Polymer solutions and suspensions are both categorized as non-Newtonian fluids, but there are some qualitative differences.

A polymer is often considered as a long synthetic chain assembled by several identical monomers. However, biological molecules such as DNA and proteins are also polymers even though the constituent monomers has some variation. The difference between the two classes is therefore more dependent on the medium than the primary structure or sequence of the molecules.

When we talk about a solution, the medium and the molecule in consideration are of the same phase, i.e., a polar solute dissolved in a polar solvent. Qualitatively, this means that the molecules do not fold up and therefore have a large surface to volume ratio. On the contrary, non-polar molecules suspended in a polar, aqueous medium tend to decrease their surface to volume ratio, which results in a spherical shape. In conclusion, the same molecule can be suspended in one medium and dissolved in another.

More general, a suspension is a distribution of particles, droplets or aerosols in a medium of a different phase. Blood, which is the main study of this project, is roughly a suspension of cells in water. Probstein [18] has listed some of the most important parameters for the two different systems.

- Polymer solutions are dependent on concentration, temperature, molecular weight, and structure of the long chain molecule. The most important parameter is the length of the polymer chain. The polymer and the solvent are in the same phase.

- On the contrary, suspensions are dependent on solids loading, particle shape and size distribution. The single most important parameter is the volume fraction. The particle or macromolecule and the suspending medium are in different phases.

Chapter 2

Physics of Fluids

Biomechanics can be considered as an application or subfield of the more general theory of continuum physics. Continuum physics relies on the fundamental equations of classical physics, and an additional set of assumptions. As phrased by Y. C. Fung [11], *The determination of the internal condition of a body in response to external forces is what continuum mechanics is about.* A body will, in this report, be considered only in flow problems and is therefore a fluid.

In this section we will introduce the general theory, which is required to model a fluid flow. We will also discuss the required assumptions, as in particular the continuum assumption becomes tenuous at small length scales.

Certain dimensionless numbers are used to characterize the state or behavior of a fluid in a specific geometry, i.e., the Reynolds number is used as a measure for the possibility of turbulence in a flow. We will briefly present a list of dimensionless numbers.

At the close of this section, we will consider some of the requirements to model complex fluids in complex geometries. Compared to a Newtonian fluid, the complexity is due to a different interaction between individual fluid elements, and it can therefore be built into the constitutive equation. We will therefore take a closer look on the possibilities of incorporating shear rate dependence and normal forces. This is illustrated by the generalized Newtonian fluid and the Criminale-Ericksen-Filbey (CEF) equation.

2.1 Continuum physics

The foundation for continuum physics is the equations of classical physics. Furthermore, there are three extra axioms or assumptions, which have to be fulfilled, in order to consider the system as a continuum. The formulation of the axioms are highly inspired by Fung [11].

1. A body of finite size can be considered a continuum, if it satisfies

the requirements of the continuum assumption: Under deformation neighboring particles in the body remain neighbors.

2. The stress and shear rate field can be defined everywhere in the body.

3. At any point in the body the stress depends only on the immediate strain or shear rate at the same point.

First, we shall define some of the newly introduced words. The real number system is continuous. Between two numbers on a coordinate axis, we can always pick a third number. If we consider a distribution of molecules in a real system, we know the molecules will be assigned discrete values on the real number axis. Therefore, a central idea in this theory is to take a real discrete system into a continuous mathematical system. In this report the mathematical system will be referred to as a *continuum*.

A *material particle* is the smallest part of a continuum, and it is in general much larger than the molecules and particles within the system. The minimum size of a material particle is related to the uncertainty on the physical quantities of the real system. If we for example consider the distribution of density in real matter, it will start to fluctuate when the material particle becomes increasingly small.

Roughly a real matter can be expressed as a continuum if it satisfies the requirements of the continuum assumption. The continuum assumption states that any point in a real system can be assigned values of physical properties with a relatively small error. In the case of density, we could consider a set of decreasing subspaces Ω_1, Ω_2, ... Ω_n, where Ω_{n-1} enclose Ω_n and all enclose the point P, see Fig. 2.1(a). To each of the subspaces we assign a mass M_n and a volume V_n. The density of a subspace is then defined as M_n/V_n. Furthermore, it is assumed that there is a limit $V_n \to V_L$

$$\left| \rho_P - \frac{M_n}{V_n} \right| < \epsilon, \tag{2.1}$$

where ϵ is a small number. The quantity ρ_P is the density at the point P with the acceptable variability ϵ in a limit V_L. In this way all physical quantities can be defined.

Axiom no 1 states that the material particles will be neighbors at all times. For a fluid flow, the material particles will be stationary, if we disregard rigid body motion, i.e, the geometry is not moving. However, the properties of the particles will change in time.

Axiom no 2 states that stress and shear rate can be defined in a similar way as we defined the density.

Axiom no 3 states that the stress is dependent on the shear rate at the very same point, this axiom will be expressed in the constitutive equation.

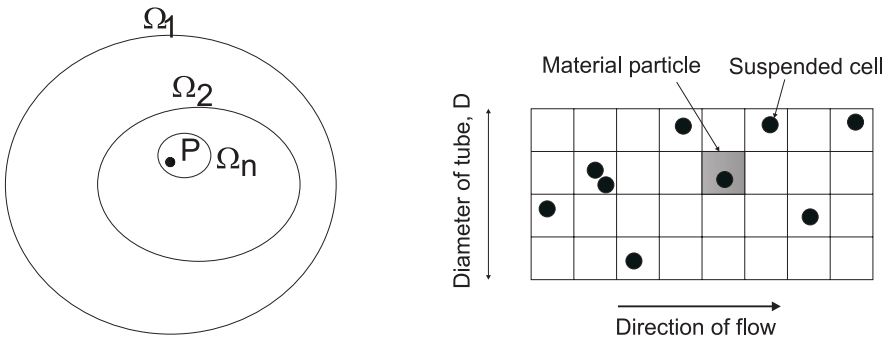

(a) (b)

Figure 2.1: In panel (a) is seen a series of decreasing subset Ω_n. They all enclose the point P and Ω_{n+1} encloses Ω_{n+1}. The figure is used to express the continuum assumption in Eq. (2.14). Panel (b) shows a grid of material particle in a section of a microchannel. The black balls represents suspended blood cells. One of the material particles is shaded for reference in the text.

To illustrate the consequence of the continuum assumption in relation to this work and microfluidics in general, we will consider blood in a microtube. Down to what dimension can blood be expressed as a continuum?

Figure 2.1(b) shows a suspension of blood cells in a microtube. The minimum size of a material particle is related to the relative error of the density. If the material in consideration is in a gaseous phase, we observe a large fluctuation for the density of a material particle if the dimensions of the body approaches the inter-molecular distance.

The relative error for the number of blood cells $\langle N_i \rangle$ in a material particle is given by

$$r = \frac{\Delta N_i}{\langle N_i \rangle}, \tag{2.2}$$

where ΔN_i is the fluctuation. The subscript i is referring to a particular material particle. For the purpose of calculating the relative error, we shall consider a binomial distribution of N identical and noninteracting cells in the shaded box in Fig. 2.1(b). The shaded box designates a particular material particle. The probability that a particle will be in the box is denoted P_i. For the binomial distribution we can write the mean $\langle N \rangle$ and standard deviation σ_i as

$$\langle N_i \rangle = NP_i, \tag{2.3}$$

and

$$\sigma_i = \Delta N_i = \sqrt{P_i(1 - P_i)N}. \tag{2.4}$$

The probability P_i depends on the position and the number of material particles or discretization. If $P_i \ll 1$ Eq. (2.2) yields

$$r \approx \frac{\sqrt{P_i N}}{N P_i} = \frac{1}{\sqrt{\langle N_i \rangle}} \tag{2.5}$$

If we consider water, the number of molecules in a fluid volume is in the order of the Avogadro constant. The number can be calculated as

$$N_{\text{molecules}} = M N_A = 55\,\text{molL}^{-1} \times 6 \times 10^{23}\,\text{mol}^{-1} = 3 \times 10^{25}\,\text{L}^{-1} = 3 \times 10^{28}\,\text{m}^{-3}, \tag{2.6}$$

where M is the molarity of water and N_A the Avogadro constant. If we choose a relative error $r = 0.01$, we can calculate the required volume of a material particle V_{mp}

$$V_{\text{mp}} = \frac{1}{N_{\text{molecules}} r^2} = \frac{1}{3 \times 10^{28}\,\text{m}^{-3} 0.01^2} = 3 \times 10^{-25}\,\text{m}^3 \simeq (7nm)^3, \tag{2.7}$$

i.e., a cube with side length $\sim 7\,\text{nm}$. This means that the continuum assumption for condensed water is becoming critical, when we go to a dimension ten times the size of a water molecule. The diameter of a water molecule is about 0.3 nm.

If we consider blood, we would expect the material particles to be larger, as the largest dimension of a red blood cell is $8\,\mu$m. The concentration of blood cells in a fluid volume of blood is $5 \times 10^6\,\mu\text{L}^{-1}$. If we do the same calculations for blood as for water, we obtain that the length of a material particle is $130\,\mu$m.

In conclusion, we can say that the continuum assumption is dependent on the relative size of three length scales

$$\ell_{\text{Real particle}} \ll \ell_{\text{mp}} \ll \ell_{\text{System}}. \tag{2.8}$$

When the size of a the system, i.e, the channel width, approaches the size of a real particle, the assumption is starting to fall apart.

A rule of thumb says [23] that the size of a the system for a condensed matter should be 10 times the size of the largest molecule. In blood the far most abundant of the cells are the red blood cells. Therefore, at dimensions below $70\,\mu$m the assumption that the physical quantities are continuous becomes questionable.

It is noticed that there is a slight disagreement between the two ways of estimating the limit for the continuity assumption. However, both methods indicate that we should be cautious in the micrometer range.

2.2 The governing equations

In the present work, we consider materials without gradients in temperature, and the conserved quantities of interest are therefore mass and momentum.

These two conserved quantities leads to the continuity equation and the equation of motion. A third equation, the constitutive equation, relates the shear rate with the shear stress, and we have a set of equations that completely determines a shear flow.

The sign in the equation of motion can vary between the different textbooks because of a different notation in the definition of the stress tensor. Of course, the dynamics of a system should be invariant to conventions, and we shall therefore resume the basic assumptions stated by Fung [11].

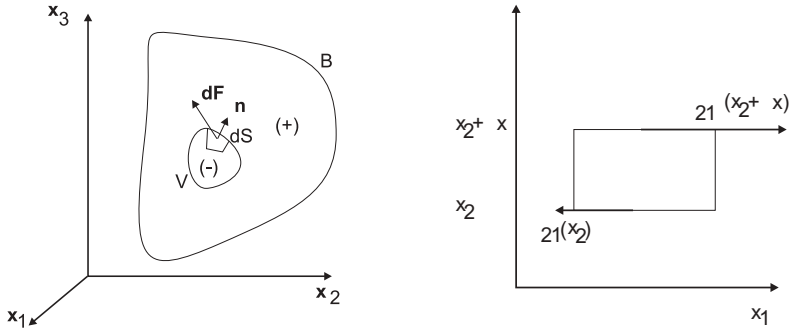

(a) (b)

Figure 2.2: Panel (a): The force $d\mathbf{F}$ on a small surface element dS, exerted by the fluid on the positive side. Panel (b): A stress component is considered positive if the outward normal vector and the stress vector both points in the positive or negative direction.

Consider a material bounded by the surface B, as shown in Fig 2.2(a). Define an arbitrary volume V within B, and let it be bounded by a surface S. A small element on this surface dS is assigned a normal vector $\mathbf{n}$, and d$\mathbf{F}$ represents the force exerted by the surrounding fluid on the fluid inside the surface. To distinguish outside and inside, the normal vector points always outward, and the fluid on the outside shall be referred to as the positive side.

In general, the magnitude of a surface force is dependent on the size of the surface. The stress tensor is therefore defined as the force per unit surface in the limit of an infinitesimal surface element,

$$\tau_{ij} = \frac{dF_j}{dS_i}. \tag{2.9}$$

As the volume V is arbitrary the stress tensor is defined for any surface in the fluid, down to the size of a material particle. A quick note on the sign convention for the stress tensor, in Fig. 2.2(b) is sketched a volume element in a Couette flow. In such a flow the velocity in the x_1 direction is an increasing function of x_2

$$v_1 = \dot{\gamma}_{21} x_2, \qquad v_2 = v_3 = 0, \tag{2.10}$$

where v_1 denotes the velocities in the x_1 direction, etc. A component in the stress tensor, for a given plane, is considered positive if the corresponding component of the outward normal vector is pointing in the same direction. In the figure, both stress vectors are positive, but due to the increasing velocity the stress is larger at $x_2 + \Delta x_2$. Newton's equation is therefore expressed as

$$\tau_{21} = \mu \frac{dv_1}{dx_2}, \tag{2.11}$$

where μ is the Newtonian viscosity. Bird [3] et al. consider the force exerted by the negative side upon the fluid on the positive side, which results in a negative τ_{21} in Eq. (2.11).

2.3 The equation of continuity

The continuity equation is derived on the assumption of mass conservation. Again, we consider the volume V fixed in space, sketched in figure 2.2(a). The rate of change of mass in V should equal the flux through the surface, and we can therefore write

$$\frac{\partial}{\partial t} \int_V \rho dV = - \int_S \mathbf{n} \cdot \rho \mathbf{v} dS. \tag{2.12}$$

On the left hand side, the limits of V are independent of time, and the integral is therefore interchangeable with the differential operator. Using Gauss' theorem yields

$$\frac{\partial \rho}{\partial t} = -\boldsymbol{\nabla} \cdot (\rho \mathbf{v}). \tag{2.13}$$

A more convenient form can be obtained after differentiation of the right hand side and rearranging:

$$\frac{D\rho}{Dt} = \frac{\partial \rho}{\partial t} + \mathbf{v} \cdot \boldsymbol{\nabla} \rho = -\rho \boldsymbol{\nabla} \cdot \mathbf{v}, \tag{2.14}$$

where D/Dt is the material derivative. Using the material derivative implies that we observe changes as we follow a fluid volume instead of considering a volume fixed in the initial frame.

Fluids that are constant in time and homogenous along the streamlines are said to be incompressible. For these fluids the continuity equation, Eq. (2.14), reduces to $\boldsymbol{\nabla} \cdot \mathbf{v} = 0$.

2.4 The equation of motion

The equation of motion is derived in a similar manner, but one needs to include a few more terms. The conserved quantity is momentum, and we shall set up the balance equation in terms of *momentum per unit time*. The basic

idea is that the fluid volume V is exchanging momentum with its surroundings via surface and volume forces. In surface forces we include molecular friction by the tensor $\boldsymbol{\tau}$, convection by the tensor $\mathbf{vv}$ and pressure as the scalar P. Volume forces are, for example, gravity, electrical, and magnetic forces. We shall denote them all by the vector $\mathbf{S}$. Using the same arguments as before, the volume is fixed and Gauss' theorem gives the equation of motion, here expressed in vector notation

$$\frac{\partial \rho \mathbf{v}}{\partial t} + \boldsymbol{\nabla} \cdot (\rho \mathbf{vv}) = \boldsymbol{\nabla} \cdot \boldsymbol{\tau} - \boldsymbol{\nabla} P + \mathbf{S}. \tag{2.15}$$

For an incompressible fluid the expression can be simplified by noting that

$$\boldsymbol{\nabla} \cdot (\mathbf{vv}) = (\mathbf{v} \cdot \boldsymbol{\nabla})\mathbf{v} + \mathbf{v}(\boldsymbol{\nabla} \cdot \mathbf{v}) = (\mathbf{v} \cdot \boldsymbol{\nabla})\mathbf{v}. \tag{2.16}$$

Inserting Eq. (2.16) into Eq. (2.15) gives

$$\rho \left[\frac{\partial \mathbf{v}}{\partial t} + (\mathbf{v} \cdot \boldsymbol{\nabla})\mathbf{v} \right] = \boldsymbol{\nabla} \cdot \boldsymbol{\tau} - \boldsymbol{\nabla} P + \mathbf{S}. \tag{2.17}$$

2.5 The Navier-Stokes equation for an incompressible flow

A large number of important liquids have a Newtonian behavior, which means the relation between shear stress and shear rate is constant. The shear stress is a symmetric, isotropic, and second order tensor. It can therefore be expressed by two invariants [11]

$$\tau_{ij} = \frac{1}{2}\lambda \dot{\gamma}_{kk} \delta_{ij} + \mu \dot{\gamma} = \frac{1}{2}\lambda (\boldsymbol{\nabla} \cdot \mathbf{v}) \delta_{ij} + \mu \dot{\gamma} = \mu \dot{\gamma}, \tag{2.18}$$

where λ and μ are scalars. The last equality is obtained when the flow is incompressible. Substituting Eq. (2.18) into Eq. (2.17) we obtain the dynamical equation for a Newtonian, isotropic, and incompressible flow

$$\rho \left[\frac{\partial \mathbf{v}}{\partial t} + (\mathbf{v} \cdot \boldsymbol{\nabla})\mathbf{v} \right] = \mu \boldsymbol{\nabla}^2 \mathbf{v} - \boldsymbol{\nabla} P + \mathbf{S}. \tag{2.19}$$

This equation is The Navier-Stokes equation for an incompressible flow, with μ denoting the Newtonian viscosity.

2.6 Flow at low Reynolds number

In traditional engineering problems, turbulent flow is the most common flow type. In microfluidics, however, the small dimensions suppresses the development of turbulence, and the flow is said to be laminar. In what regime we find the system is dependent on the ratio between momentum transported by convection and momentum transported by viscous diffusion [18]. This balance is expressed in Reynolds number

$$Re = \frac{\rho \overline{v}^2/d}{\mu \overline{v}/d^2} = \frac{\overline{v}\rho d}{\mu}, \tag{2.20}$$

where d is a characteristic dimension of the geometry, μ the Newtonian viscosity and $\overline{v}$ is the mean velocity. Small numbers are for example obtained when the viscosity is high or the dimension is small. Under these conditions the development of turbulence is suppressed, and we have a laminar flow. According to Pedersen [16] low Reynolds numbers in a tube flow is below 580, and high numbers are above 750, when the characteristic dimension d is the tube diameter.

To get a better feeling of the conditions in microfluidics, it is instructive to take a closer look on the significance of the viscosity and diameter in a tube flow. A typical flow rate and dimension for a micro fabricated device is $\dot{Q} = 10\,\mu\text{L s}^{-1}$ and $d = 100\,\mu\text{m}$, which results in a mean velocity $\overline{v} = 1.3\,\text{m s}^{-1}$. For a system containing water the corresponding Reynolds number is $(1.3\,\text{m s}^{-1} \times 1003\,\text{kg m}^{-3} \times 10^{-4}\,\text{m})/(8.55 \times 10^{-4}\,\text{Pa s}) = 150$, clearly a laminar flow. Considering the same system with $d = 1\,\text{cm}$ increases Reynolds number by two orders of magnitude. If the increasing dimension should be balanced out solely by a change in viscosity, we would have $\mu = 85.5 \times 10^{-3}\,\text{Pa s}$: a fluid more viscous than syrup.

In general, dimensionless numbers appears from the governing equations and can be used to determine the dominating forces in a system. We have earlier divided the forces into surface and volume forces, but, when considering dimensionless numbers, it is more appropriate with a more detailed categorization. Probstein [18] suggests that the governing forces in a suspension can be divided into colloidal and viscous forces, when we consider mass transport of particular species. Viscous forces are as usual related to friction between neighboring molecules, whereas the second class includes Brownian motion, surface forces and electrostatic repulsion forces.

As mentioned, at a low Reynolds number momentum transport is dominated by viscous forces, and convection has only a little influence. In the same way is the Peclet number indicating if forces related to Brownian motion are more important than viscous forces. A more detailed derivation of the numbers can be found in a textbook of Probstein [18].

- The Peclet number: the ratio between dissipated and kinetic energy

$$Pe = \frac{\mu\dot{\gamma}a^3}{kT}. \tag{2.21}$$

- The shear-repulsion number: the ratio between convective and electrostatic repulsive force

$$N_{SR} = \frac{\mu a^2\dot{\gamma}}{\epsilon\zeta^2}. \tag{2.22}$$

- The shear-attraction number: the ratio between viscous energy and van der Waals attractive energy

$$N_{SA} = \frac{\mu a^3\dot{\gamma}}{A}. \tag{2.23}$$

Here is μ the viscosity of the suspending medium, a is the particle radius and separation between the particles, k Boltzmann's constant, T the temperature, ϵ the vacuum permeability, ζ the zeta-potential and A is the Hamaker constant. The regions at numbers low or high compared to unity are referred to as the low and high shear limit.

The dimensionless numbers establish a framework, which is helpful in order to analyze the governing forces in a flow problem. In the present work we will be most concerned with the Reynolds number.

2.7 Shear limit behavior

For rigid particle suspensions, the shear thinning effect is only observed in the colloidal domain, i.e., particles with a diameter in the range from $1 - 1000\,\text{nm}$, see Evans[9]. This kind of suspensions start of in a Newtonian region, whereafter it enters a shear thinning region, and then again reaches a plateau. A suspension can be adjusted with an electrolyte in such a way that surface forces can be neglected. In this case the system will be governed by viscous forces and Brownian motion, and the Peclet number is the essential parameter. In Fig. 2.3 is seen the relative viscosity as a function of the reduced shear stress, which, similar to the Peclet number, is the relation between viscous and Brownian forces. In the experiment different sizes of colloidal particles, and different Newtonian fluids were used.

The results shows that at low shear rates, where the Brownian motion is dominant, the viscosity is constant. As the Brownian forces becomes less important compared to the shear stress, the viscosity drops, and reaches a plateau when diffusion can be neglected. Coarse particles do not show this behavior, as the viscous forces always will be dominant. Furthermore, the concentration has to be rather high. Otherwise, the distance between the molecules is large, and friction due to random motion has no influence.

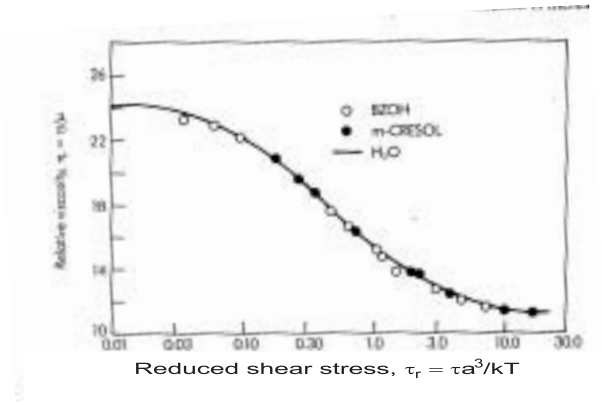

Figure 2.3: The relative viscosity for different sized particles in different Newtonian fluids. On the x-axis is seen the relative shear stress, where τ is the measured stress. This last parameter is essentially the Peclet number; the relation between viscous and Brownian forces, see Probstein [18].

.

2.8 Generalized Newtonian fluids and normal forces

As already discussed, some fluids have a shear rate dependent viscosity, but some can also exhibit even more complex flow properties due to normal forces. To see how some of these phenomena can be explained, we can

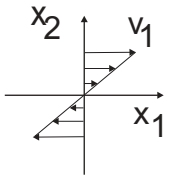

Figure 2.4: The flow field in a Couette flow is invariant to a 180^o rotation around the x_3-axis. The arrows are symbolizing the velocity in the x_1 direction.

.

consider the simple Couette flow. In general, the stress tensor has nine components, but, as it is symmetric, only six are independent. Furthermore, as seen in Fig. 2.4 the velocity field is symmetric to a 180^o rotation around the x_3-axis in a Couette flow. If the stress tensor only depends on the flow field, i.e., the material is isotropic, it will also be symmetric to the same rotation, and there is only four independent entries left,

$$\boldsymbol{\tau} = \begin{bmatrix} \tau_{11} & \tau_{12} & 0 \\ \tau_{12} & \tau_{22} & 0 \\ 0 & 0 & \tau_{33} \end{bmatrix}. \tag{2.24}$$

Eq. (2.24) shows that we have to consider the magnitude of normal stresses, when we are dealing with non-Newtonian fluids.

The Criminale-Ericksen-Filbey equation, (CEF), is a suitable constitutive equation for a steady shear flow

$$\boldsymbol{\tau} = \begin{bmatrix} (\psi_1 + \psi_2)\dot{\gamma}^2 & \eta\dot{\gamma} & 0 \\ \eta\dot{\gamma} & \psi_2\dot{\gamma}^2 & 0 \\ 0 & 0 & 0 \end{bmatrix}, \tag{2.25}$$

where $\dot{\gamma}$ is the shear rate, η is the apparent viscosity, ψ_1 and ψ_2 are the so-called first and second material function, respectively. Eq. 2.25 is for a simple Couette flow, but a more general CEF-equation can be seen in the textbook of Bird et al. [3], by the use of so-called convected derivatives.

The material functions are also referred to as the *viscometric functions*. By means of the CEF-equation they can all be measured in a rheometer, however, ψ_2 are often so small that it is difficult to obtain a reliable result.

The first and second material functions relates the normal components of the stress tensor to the shear rate. As mentioned in section 1.2 one of the effects of the normal forces or elastic properties can be seen in the secondary flow in a geometry with a sudden contraction. However, as we at

this point have very little knowledge on these properties, we will leave this discussion by noting that there are other material functions than the viscosity. Furthermore, as blood is a non-Newtonian liquid, its flow properties can probably not be explained by viscosity alone in complex geometries.

For many engineering purposes normal forces are negligible and the CEF-equation reduces to a generalized Newtonian fluid. This model is a simple extension of the theory for Newtonian fluids, as the viscosity instead of being a constant, is a scalar function of the scalar invariants of the shear rate tensor

$$\boldsymbol{\tau} = \eta(|\dot{\boldsymbol{\gamma}}|)\,\dot{\boldsymbol{\gamma}}, \tag{2.26}$$

where $|\dot{\boldsymbol{\gamma}}|$ is the magnitude of the shear rate tensor. The magnitude is defined as

$$|\dot{\boldsymbol{\gamma}}| = \sqrt{\frac{1}{2}\sum_{i=1}^{3}\sum_{j=1}^{3}\dot{\gamma}_{ij}\dot{\gamma}_{ij}}. \tag{2.27}$$

The generalized Newtonian fluid applies to an incompressible shear flow [3].

Chapter 3

Blood

3.1 Composition of blood

Blood is the fluid transporting oxygen, carbon dioxide, nutrients, salts, hormones, metabolites and many other components that make it possible to maintain life. From a rheological point of view, the most important constituents are plasma and the red blood cells (RBCs). Meaning, RBCs take up about half the volume of *whole blood*, and have a significant influence on the flow. The term whole blood is used for blood that has not been modified in any physical sense, e.g, defibrinated. In some experiments fibrinogen is removed to prevent blood clotting.

Plasma consists of 90 %(w/w) water, 7 %(w/w) is proteins, and it behaves like a Newtonian fluid with a constant viscosity on 1.2×10^{-3} Pa s [10]. The specific gravity of plasma is 1.026, and 1.090 for RBCs. The cells are as mentioned mainly RBCs, the parameter used for modelling purposes is the hematocrit level, which is the volume fraction that RBCs occupy. The average hematocrit is $40 - 52\%$ for men, and $35 - 47\%$ for women. When blood is left undisturbed, the cells start to coagulate. The process is called blood clotting, and is initiated by the plasma protein fibrinogen. Table 3.1 shows the contents of blood.

In many rheological experiments whole blood is treated with an anticoagulant, heparin, EDTA or citrate. EDTA and citrate binds calcium ions, blood clotting factor IV, in a complex. Heparin is a negatively charged polysaccharide that enhances the activity of antitrombin III, which is a plasma protein that inhibits thrombin, factor II. Blood used for transfusions is often anticoagulated with sodium citrate, as it is a natural component in the body, see Stryer [22]. However, EDTA is recommended for rheological measurements, as it has the least effect on the viscosity. Citrate tends to shrink the Red Cells by removal of water, see Lowe and Barbenel [15]. There are all together 13 factors in the blood clotting cascade, and in principle the clotting process could be stopped at any of these stages. As a note of warn-

Table 3.1: The constituents of human whole blood.

	Composition		Concentration
Plasma	Water 90%(w/w)$^{(1)}$		
	Proteins 7%(w/w)$^{(1)}$	Albumins	$4.5 - 5.7 \times 10^{-5}\,\mathrm{g}\,\mu\mathrm{L}^{-1}$ $^{(2)}$
		Globulins	$1.3 - 2.5 \times 10^{-5}\,\mathrm{g}\,\mu\mathrm{L}^{-1}$ $^{(2)}$
		Fibrinogen	$1.3 - 2.5 \times 10^{-5}\,\mathrm{g}\,\mu\mathrm{L}^{-1}$ $^{(2)}$
	Salts, dissolved gases, hormones, glucose, metabolites, nutrients		
Cellular components	Red blood cells	$7\,\mu$m	$3.6 - 5.4 \times 10^{6}\,\mu\mathrm{L}^{-1}$
	White blood cells	$8 - 20\,\mu$m	$5 - 10 \times 10^{3}\,\mu\mathrm{L}^{-1}$
	Platelets	$1 - 2\,\mu$m	$1.5 - 4.0 \times 10^{5}\,\mu\mathrm{L}^{-1}$

Notes: $^{(1)}$ denotes data from Fung [10], $^{(2)}$ West and Todd [30]. All other data are taken from Solomon et al. [21]. In literature there is some variation of the listed values. For example, the mean value of the red blood cell may vary between $7 - 8\,\mu$m.

ing, the number of the factor does not refer to its number as participant in the cascade of processes leading to clotting.

3.2 Macroscopic rheological properties of blood

The rheological properties of blood in a shear flow are outlined in a textbook by Y.C. Fung [10]. In order to get an impression of the behavior of blood in a shear flow, some of the key features are resumed here. The shear rate is defined as a measure of the deformation of the liquid

$$\dot{\gamma} = \frac{1}{2}\dot{\gamma}_{\mathrm{old}} = \frac{1}{2}\left(\frac{dv_i}{dx_j} + \frac{dv_j}{dx_i}\right), \tag{3.1}$$

where v_i is the velocity in the x_i direction. In some of the figures, the shear rate $\dot{\gamma}$, was calculated according to an old convention, and it is twice the value used in literature today. It shall be noted in the relevant figures, where the old convention is used. Whenever $\dot{\gamma}$ appears in the main text in this report, it shall refer to the new convention. As seen in Fig. 3.1, the viscosity

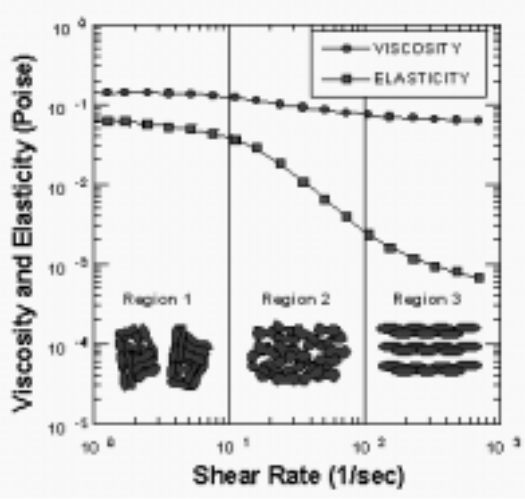

Figure 3.1: The viscoelastic behavior of blood with a hematocrit at 31 and 2 Hz measured in an oscillating flow. In the bottom of the picture is seen an illustration of the arrangement of red blood cells. The figure was taken from the Vilastic Scientific's homepage [28]. However, a similar experiment can be studied in a paper by Liepsch et al. [14].

of blood can be divided into three regions. At low shear rates, the viscosity is constant, and then it drops until it again reaches a constant plateau. When the viscosity of a liquid is a decreasing function of the shear rate, it is said to be shear thinning. In the figure, it is also indicated that, on a microscopic level, the shear thinning is caused by the break down of aggregates and a cell layering of the RBCs. This internal organization of the cells reduces the friction.

Figure 3.2(a) shows how the apparent viscosity, the relation between shear stress and shear rate, increases with the hematocrit. It is seen that human whole blood (HWB) has a higher viscosity than HWB without fibrinogen, a protein important for cell aggregation. HWB's viscosity without fibrinogen is higher than the one for washed cells in a Ringer solution. A Ringer solution is a buffered isotonic salt solution, which means the cells are suspended in a medium with near physiological conditions, 150 mM NaCl. In the washing process the plasma is substituted with Ringers solution, and the viscosity is therefore lowered.

At zero hematocrit all the fluids behaves Newtonian. At small shear rates cell aggregation has a large influence on the viscosity. For a hematocrit at 45%, the difference between $\bullet$, x, and $\circ$ is more pronounced at small shear rates, compared to hematocrits at zero and 90%. Meaning, the effect of cell aggregation is largest at moderate hematocrits.

Figure 3.2(b) shows the importance of aggregation and deformation of RBCs for a hematocrit at 45%. The hematocrit where the aggregation effect

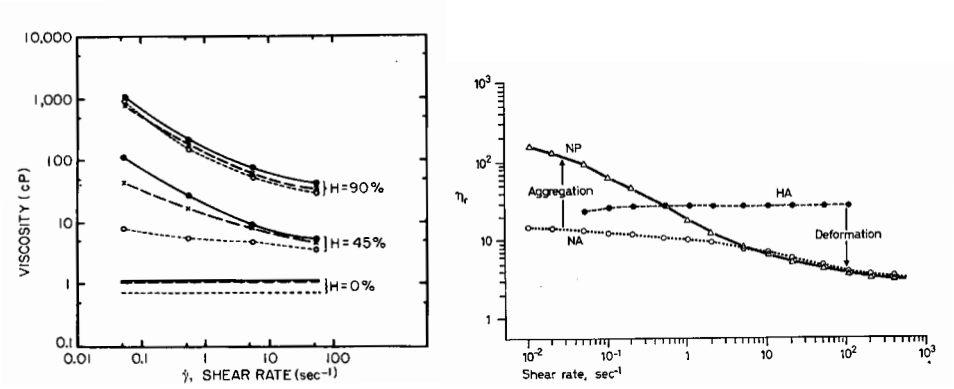

(a) (b)

Figure 3.2: Panel (a): The viscosity shear rate relations in whole blood (•), defibrinated blood (x), and washed cells in a Ringer solution ($\circ$). H is the hematocrit, the old shear rate convention was used. Panel (b): relation between relative apparent viscosity and shear rate in three types of suspensions, where the hematocrit is 45%. NP is a normal RBC suspension, in NA fibrinogen is removed, and in HA the cells are hardened, from Fung [10].

was seen to be large.

When HWB is compared to a suspension of hardened cells, a large difference in viscosity is seen at high shear rates. In other words, at high shear rates the deformability is important for the shear thinning effect.

At low shear rates is another comparison with defibrinated blood. The figure shows that cell aggregation has a large influence on the viscosity at low shear rates. It may be noticed that a suspension of hardened cells has a Newtonian behavior.

A fit of a constitutive equation to viscosity data is seen in Fig. 3.3(a). For hematocrits below 39% blood can be described by Casson's equation:

$$\sqrt{\boldsymbol{\tau}} = \sqrt{\boldsymbol{\tau_y}} + \sqrt{\eta\dot{\boldsymbol{\gamma}}}, \tag{3.2}$$

where $\boldsymbol{\tau}$ is the shear stress, $\boldsymbol{\tau_y}$ the yield stress, η the apparent viscosity, and $\dot{\boldsymbol{\gamma}}$ the shear rate. However, the validity of the equation is also limited to small values of the shear rate.

The yield stress is increasing with hematocrit, Fig. 3.3(b), but the magnitude of the stresses are very small, about $0.05\,\mathrm{dyne\,cm^{-2}}$ or 5×10^{-3} Pa. For comparison, the same pressure would be exerted by $50\,\mu$L of water spread out on a square centimeter. The figure is just to show the magnitude of the yield stress, in this context it is less important that the data points fit a straight line, if the yield stress is plotted to the power of 1/3.

At high shear rates blood behaves Newtonian. The Newtonian range can be seen to the right of the dashed line in Fig. 3.4(a). Meaning, different features of the constitutive equations are needed to model the blood flow

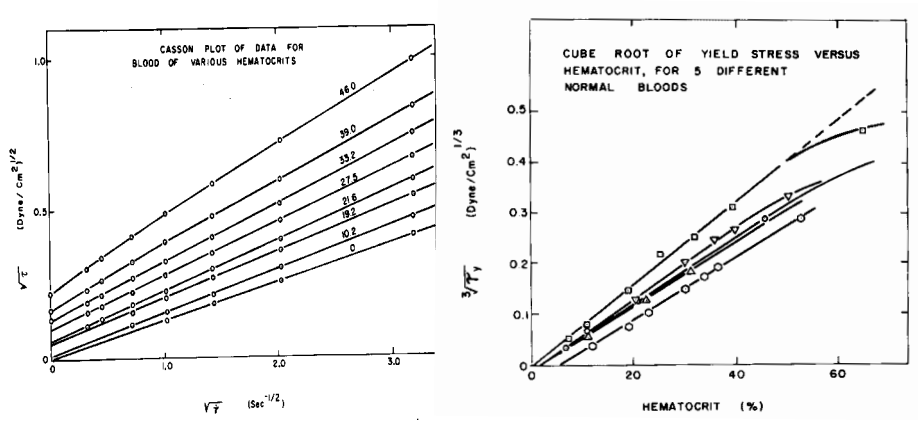

(a) (b)

Figure 3.3: All the shear rates in the figures are with respect to the old convention 3.1. Panel (a): In the figure it is seen a Casson plot of data for blood. The Casson equation is valid at small shear rates ($\dot{\gamma}_{old} < 10$), and hematocrit less than 39%. Panel (b): variation of yield stress of blood with hematocrit, from Fung [10].

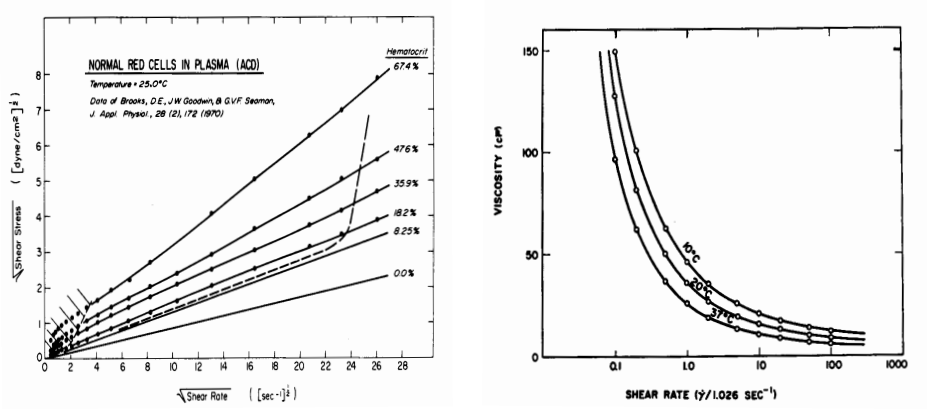

(a) (b)

Figure 3.4: All the shear rates in the figures are with respect to the old convention Eq. 3.1. Panel (a): the part of the data to the right of the dashed line are in the Newtonian region. The Newtonian region starts, for high hematocrits, at about $\sqrt{\dot{\gamma}_{old}} = 24\,\mathrm{s}^{-1/2}$. For hematocrits at 0 and 8.25% the actual data points are not seen. Panel (b): The influence of temperature on the viscosity for human whole blood. The effect increases when the shear rate decreases, from Fung [10].

over a large range of the shear rate. Compared to Fig. 3.3(a) this figure shows the viscosity at higher shear rates, where the Casson model breaks down. Figure 3.4(b) shows that the viscosity decreases with temperature, like liquids in general. Compared to high shear rates the temperature effect is larger at small shear rates.

3.3 Deformability of red blood cells

As plasma is showing the Newtonian characteristics, it is evident that the red blood cells are responsible for the non-Newtonian behavior. Red blood cells are relatively big in the sense that their Brownian motion has little effect on the flow. Blood is shear thinning, meaning the viscosity decreases with increasing shear rate. This phenomenon can be explained by the blood cells ability to align and deform in the flow.

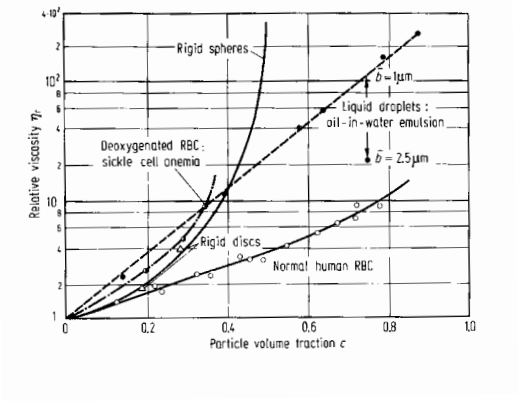

Figure 3.5: Relative viscosity of human blood at 25 °C as a function of red cell volume fraction, compared to that of suspensions of rigid latex spheres, rigid disks, droplets, and sickled RBCs (rigid, from Fung [10].

.

In Fig. 3.5 can be seen a comparison of different kinds of particles; even though liquid droplets of oil dispersed in water show higher viscosity than normal blood, they are comparable. The flow of oil droplets in water is, as for blood, maintained at very high volume fractions. Therefore, we may conclude that droplets and RBCs have a similar elastic behavior. The deformability of the RBCs makes blood a remarkable fluid. It is seen, when the volume fraction is more than 50%, most other fluids will stop to flow. Blood, however, can maintain the flow until hematocrits of 98%. Still, a suspension of oil droplets is more viscous than a suspension of red cells. It is therefore believed that a RBC is more deformable than a droplet.

Blood cells are responsible for the shear thinning effect, and the physical explanation for this phenomenon is the cells flexibility and tendency to align with the flow. The red cells align in such a way that the largest dimension is paralleled with the direction of the flow; the fraction of aligned cells increases with the shear rate. Figure 3.6(a) shows the orientation of a single RBC in a highly diluted suspension, where the particles do not interact. The fraction of aligned cells are seen to increase with the shear rate, which is in contrast

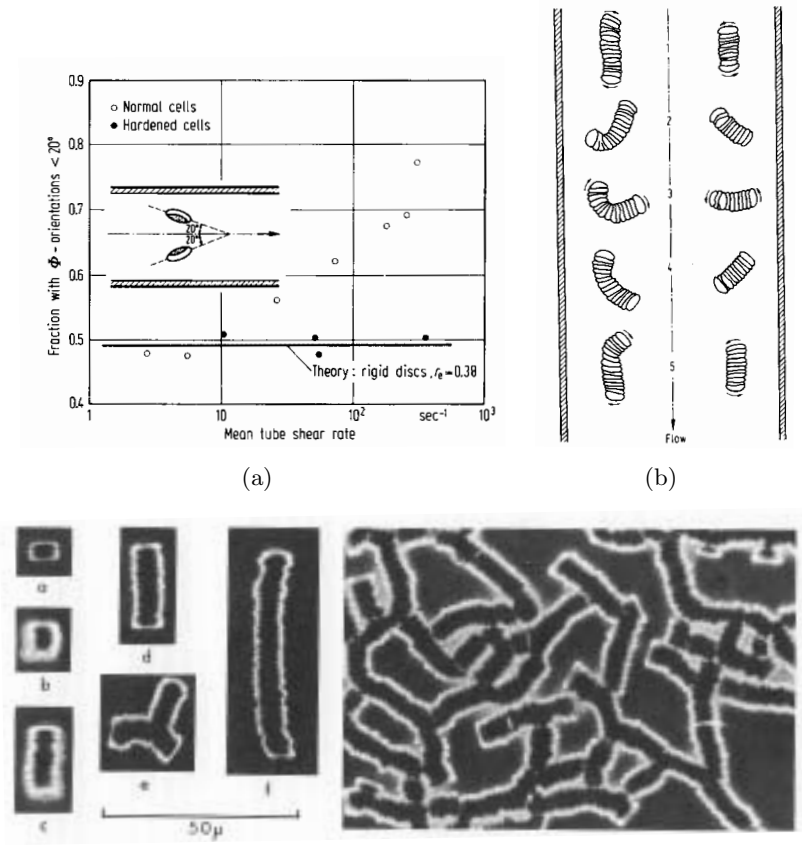

(a) (b)

(c)

Figure 3.6: The pictures are obtained by a high powered microscope. Panel (a): The figure shows that RBCs aligns better in a shear flow than hardened RBCs. Panel (b): The tumbling of a single rouleaux in a shear flow. Tumbling of rouleaux increase the viscosity. Panel (c): Microscopic picture of rouleaux, the RBCs form large chains resembling a stack of coins. It is also noticed that rouleaux are capable of forming fairly large and complex patterns, from Fung [10].

to the findings of the hardened cells shown in the same figure.

Figure 3.6(b) shows the tumbling of two rouleaux in a diluted suspension, hematocrit less than ten. Rouleaux are aggregates of blood that can be broken down to single cells at high shear rates. The large viscosity at low shear rates is a consequence of the tumbling. When the rouleaux is broken down, the contribution to the viscosity is decreased. The smaller parts do not disturb the flow to the same extent, as the larger aggregate.

In Fig. 3.6(c) is shown a microscopic picture of different forms of rouleaux. The formation of these aggregates are dependent on the presence of fibrinogen and albumin. Rouleaux formation should not be confused with blood clotting, the latter process is totally irreversible.

Even though blood seems to have the same function in all mammals there are apparently some differences. For example, in bovine blood the cells do not form rouleaux. Therefore it will deviate less from a Newtonian liquid than HWB. In order to analyze blood of other species in microsystems, it would therefore be necessary to study the nature of these blood types in more details.

3.4 Various constitutive equations

From a modelling point of view, it is necessary to know what constitutive equation can describe the deformations in the fluid. By the constitutive equation we establish a relation between specific fluid properties and the dynamical equations. The figures 3.3(a) and 3.4(a) are indicating that the Casson equation might be applicable at low shear rates, and hematocrits smaller than 39. However, at shear rates above $5\,\mathrm{s}^{-1}$ it is starting to deviate, and another model is required until the Newtonian region is reached. In the literature, different kinds of constitutive equations have been suggested. Zhang and Kuang [31] have made a study, where they fitted a large variety of constitutive equations to measurements obtained in a concentric cylinder. By means of a least squares fit they concluded that the Quemada, Bi-exponent and L-K equations were the best applicable for human and canine blood. Some of the equations can be seen in Table 3.2.

Many of these equations are established for clinical purposes, as a constitutive equation contains information of the rigidity of a blood cell. For example, the parameters in the Bi-exponent equation have subscripts A and D. They are related to aggregation and deformability, and can be used to make a patient diagnosis. Blood rheology in the macroscopic domain has been used extensively for that purpose, see for example [15]. However, we shall only be concerned with a few of these equations, and for more details literature should be consulted.

Table 3.2: The table contains different blood constitutive equations. The shear rates $\dot{\gamma}$ are all expressed by the new convention. All other variables are blood constitutive parameters. The intention of this table is to give an impression of the available constitutive equations. For a detailed description, the literature should be consulted [31].

Equation	Expression for τ	Parameters	Valid $\dot{\gamma}$-range (s^{-1})
Quemada	$\eta_\infty\left(\frac{1+\vartheta}{\chi+\vartheta}\right)^2\dot{\gamma}$	$\vartheta = \theta\dot{\gamma}$	0.87-118
		$\chi = \left(\frac{\eta_\infty}{\eta_0}\right)^2$	
Bi-exponent	$\left(\eta_e + \eta_D e^{-\sqrt{t_D\dot{\gamma}}} + \eta_A e^{-\sqrt{t_A\dot{\gamma}}}\right)\dot{\gamma}$		0.87-118
K-L	$\tau_y + \eta_p(\alpha_1\dot{\gamma} + a_2\sqrt{\dot{\gamma}})$		0.2-180
Casson	$\sqrt{\tau_y} + \sqrt{\eta\dot{\gamma}}$, for $\tau > \tau_y$		$0-5^{(}1)$
	no flow, for $\tau > \tau_y$		$0-5^{(1)}$
Wang	$\eta_p(\beta_1\dot{\gamma} + \beta_2\sqrt{\dot{\gamma}})$		
Powerlaw	$m(\dot{\gamma})^n$		
Walburn	$c_1 e^{(c_2 H + \frac{c_4 TPMA}{H^2})}\dot{\gamma}^{(1-c_3 H)}$		0.03-110
Weaver	$log\eta_p + (0.03 - 0.0076 log\dot{\gamma})H$		0.03-120
Newtonian	$\mu\dot{\gamma}$		from $144^{(2)}$

(1) According to Zhang and Kuang [31] the shear rate should be $10\,s^{-1}$. However, in Fung [10] this value is corresponding to the old notation of shear rate. In this report it shall be attempted only to use shear rates defined according to the new notation, Eq. (3.1). In the references they are not always careful in defining the shear rate, which is a point of confusion. The Casson equation is valid for hematocrits less than 40%, whereas the Walburn equation is applicable until at least 50%. (2) In Fig. 3.4(a) it was seen that blood behaved Newtonian at high shear rates.

3.5 Constitutive equations in microtubes - dependence on shear rate

As the shear flow, so far, can not be described by a single constitutive equation, it is necessary to have information on the magnitude of the shear rate in the tubes. In microtubes, the flow is always laminar, and an approximation to the velocity profile for blood can be obtained by means of the equation of motion and Newton's constitutive equation.

Assuming the suspension is an incompressible fluid, the equation of mo-

tion in cylindrical coordinates is found to be

$$0 = -\frac{1}{r}\frac{d}{dr}\left(r\tau_{rz} - \frac{dP}{dz}\right). \tag{3.3}$$

The full solution for the differential equation is

$$\tau_{rz} = \frac{c}{r} - \frac{r}{2}\frac{dP}{dz}, \tag{3.4}$$

where c must be zero to avoid nonphysical properties for $r \to 0$. Combining Newtons constitutive equation,

$$\tau_{rz} = \mu\frac{dv_z}{dr}, \tag{3.5}$$

and Eq. (3.4) gives an expression for the shear rate

$$\frac{dv_z}{dr} = \frac{r}{2\mu}\frac{dP}{dz}. \tag{3.6}$$

As the pressure gradient dP/dz is negative for a flow in the positive direction, the shear rate is zero for $r = 0$, and negative for $r > 0$. The shear rate as a function of the radius is shown in Fig. 3.7.

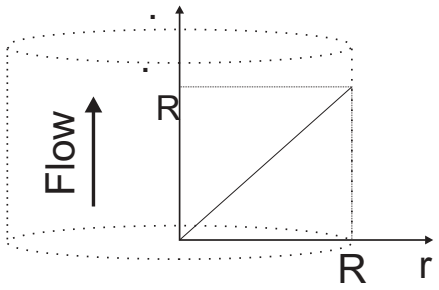

Figure 3.7: The figure shows the shear rate for a Newtonian fluid as a function of r in the tube. Because a single constitutive equation might not be valid in the entire range of the shear rate, there can be some complications in modelling the blood flow.

Even though the analysis was obtained on the Newtonian assumption, Eq. (3.6) shows that we can have a great span of shear rates in the tube, therefore, it can be difficult to find a single constitutive equation, that can be applied in the entire interval. At low shear rates the Casson equation is valid, and at high shear rates blood is showing a Newtonian behavior.

3.6 Velocity profile and cell-distribution in narrow tubes

It was noted in Fig. 3.5 that the normal RBCs showed large deviations from hardened cells, and similarities with an oil in water emulsion, in particular

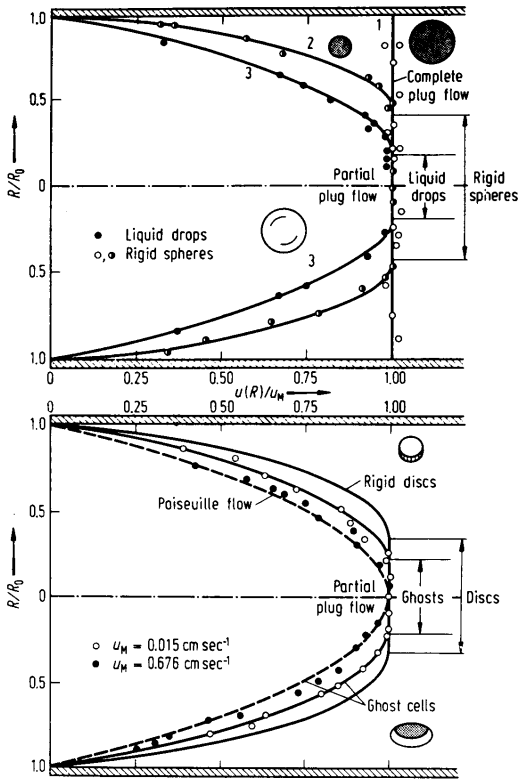

Figure 3.8: Measurements of velocity profiles for blood flow in a tube with a diameter of about 70 μm. Measurements are indicated by points, solid lines are best fit, and the dashed line is a calculated parabolic profile. Upper panel: velocity profiles for a suspension of rigid spheres, and an oil in water emulsion. Lower panel: velocity profiles for ghost cells at two different volume flow rates. A ghost cell is a red blood cell where hemoglobin has been removed. It is seen that the profile is blunted at low shear rates, i.e., when the flow rate is low, from Fung [10].

.

as the droplet fraction was increased. In Table 3.2 it was seen that different regions of shear rate required different kinds of equations for the shear stress. Another way of comparing the different systems could be a study of the velocity profiles in a microtube, as they provide information of the constitutive equation.

Figure 3.8 shows the velocity profile for rigid spheres, an emulsion of oil droplets in water and ghost cells at two different flow rates. Ghost cells are unpigmented RBCs that are traceable in a microscope. A ghost is a cell where the hemoglobin has been removed.

The width of the tube is about 70 μm. Unfortunately, the exact radius of the tube is not available in the literature, but we can get an estimate as we know the size of a cell. The relation between the diameter of a ghost

cell and the tube diameter is $d_{\text{cell}}/d_{\text{tube}} = 0.105$. If the size of a ghost cell is assumed to be the same as a RBC, namely $7\,\mu$m, the tube diameter is $67\,\mu$m.

When the particle to tube ratio is above 0.04, and the volume concentration is beyond 0.2, the velocity profile of the rigid spheres went from a parabola shaped profile into a profile showing a plug flow, resembling the movement of a solid plug in the middle of the tube. This means that the fluid attains a solidlike behavior at low shear rates. Furthermore, for rigid spheres the profile is independent of the flow rate.

An oil in water emulsion also shows deviation from the parabola shape, Fig. 3.8. However, if the flow rate is increased the degree of blunting decreases and a parabolic shape is obtained.

In this aspect, ghost cells resemble an emulsion. The shear rate can be controlled by the applied pressure, and at low shear rates the profile is blunted, but the bluntedness vanishes at high shear rates.

Still, Fig. 3.5 showed that the viscosity of blood cells, at any concentration, was lower than the viscosity of the emulsion. The only reasonable explanation is that RBCs are more deformable than liquid drops. If a droplet is left undisturbed, it assumes a spherical shape, as it reduces the surface to volume ratio. When the droplet is inserted into a shear flow the surface area is stretched, which requires energy. It is believed that the biconcave shape of a red blood cell makes it possible to deform the cells without increasing the surface area, meaning that RBCs do not disturb the flow to the same degree as liquid droplets.

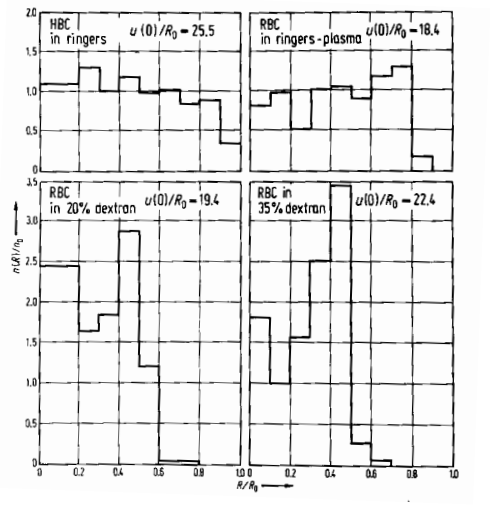

Figure 3.9: The density distribution of cells in a shear flow. On the ordinate axis is written the number of cells per cm^3 $n(R)$ divided by the syringe reservoir concentration n_0. The abscissa axis shows the different intervals of $0.1 \times R_0$ wherein the cells were counted. The observation were made 1 cm downstream of the reservoir. The tube radius: $R_0 = 41.5\,\mu$m. The mean tube shear rate $u(0)/R_0$ were approximately the same in each suspension. With the highest viscosity first, the relative viscosity of the solutions are dextran 35%, dextran 20%, ringers-plasma and ringers, from Fung [10].

Let us summarize some of the features of RBCs. At low shear rates they form aggregates, and develop nonparabolic velocity profiles in a tube flow. They are easily deformed at high shear rates, and are more flexible than liquid drops. Another interesting feature is the cells tendency to migrate away from solid surfaces. This phenomenon, referred to as the wall-effect, is also due to the deformability of the cells. The wall-effect is observed for liquid spheres, and at high shear rates it is also observed for rigid spheres. Figure 3.9 shows the distribution of cells from the center to the wall in a microtube of width $83\,\mu$m. The concentration of cells are increasing towards the direction of the center. It is also seen that the effect is more pronounced when the viscosity of the suspending liquid is increased. The viscosity of the solutions decreases in the following order, 35%-dextran, 20%-dextran, plasma-Ringers solution, and Ringers solution.

3.7 The Fahraeus-Lindquist effect

Fahraeus and Lindquist discovered in 1931 that the viscosity decreases when blood is flowing into a tube with a diameter smaller than $500\,\mu$m, i.e, the viscosity were lower in the viscometer tube than in the feed reservoir. This effect is known as the Fahraeus-Lindquist effect. Fahraeus investigated the

phenomenon further, and found that the lower viscosity was due to a decreasing hematocrit. According to Fung [10], Barbee and Cokelet investigated this problem more extensively with flow rates where Newtonian behavior is expected. Using the geometry shown in Fig. 3.10, Barbee and Cokelet showed that the Fahraeus effect could be measured for tubes with a radius between 29 and 221 μm. This phenomenon can be connected with the theory of a cell free layer close to the wall. The cell free layer becomes increasingly important in small dimensions.

Barbee and Cokelet also found that the hematocrit in the viscometer tube increased linearly with the hematocrit in the feeding reservoir. These results can be seen in Fig. 3.11(a). The figure shows the relative hematocrit as a function of the hematocrit in the feed reservoir for different sized micro tubes. To investigate the resistance of blood in microchannels they also measured the shear stress at the wall, as a function of the mean velocity divided by the tube radius. The wall shear rate is given by

$$\tau_w = \frac{R}{2}\frac{\Delta P}{L}, \tag{3.7}$$

and as we are in the Newtonian regime the flow rate can be calculated by the Hagen-Poiseuilles equation

$$\dot{Q} = \frac{\pi R^4}{8\mu}\frac{\Delta P}{L} = \bar{v}\pi R^2, \tag{3.8}$$

where $\bar{v}$ is the mean velocity. If we combine the Eqs. (3.7) and (3.8), we find that the shear stress only depends on the mean velocity $\bar{v}$, the viscosity μ, and the radius R

$$\tau_w = \frac{4\mu\bar{v}}{R} = 4\mu\bar{U}. \tag{3.9}$$

Figure 3.11(b) shows an agreement with what is predicted by Eq. (3.9). At these high through puts the shear stress at the wall is only dependent on

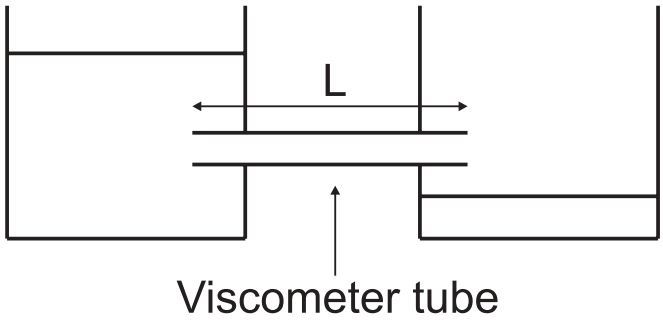

Figure 3.10: The figure shows the geometry used by Barbee and Cokelet when they studied the Fahraeus effect

.

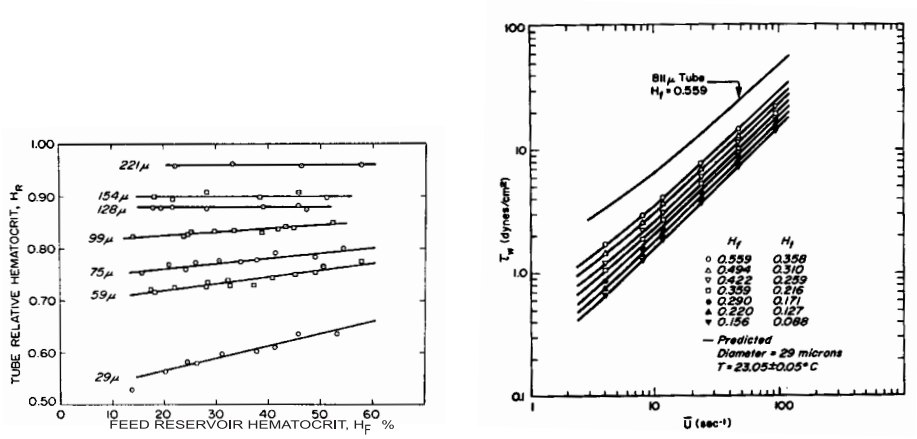

(a) (b)

Figure 3.11: Illustrating the Fahraeus effect. Panel (a): The tube relative hematocrit as a function of the feed hematocrit. The relative hematocrit is the ratio between the hematocrit in the tube and the feed reservoir. Panel (b): The shear stress at the wall as a function of the mean velocity divided by the radius in a 29 μm and a 811 μm diameter tube. The symbols are actual flow data for the smaller tube, and the solid lines represents flow data obtained in the 811 μm tube, when the tube hematocrit is the same. An 811 μm tube is considered as a macroscopic dimension. As the shear stress is the same in the two tubes, when the hematocrit is the same, there is no effect on the viscosity due to different tube diameter. The measurements are performed at high shear rates, i.e., in the Newtonian range, from Fung [10].

the viscosity, and the mean velocity divided by the tube radius, $\bar{U} = \bar{v}/R$. When blood is fed into the large tube, the hematocrit in the tube is the same as in the feed reservoir. On the contrary, in the small tube hematocrit is reduced from its feed value H_f till its tube value H_t, and the viscosity appears smaller. However, if the hematocrit is the same in the two different sized tubes, the viscosity is also the same.

3.8 Hemolysis

When living cells are suspended in a medium with a lower osmotic concentration than the interior of the cell, it will swell and lyse due to the osmotic effect. Lysis can also appear if the cells are exposed to large shear stresses. According to [5] large shear stresses corresponds to shear rates in the range $30 - 90 \times 10^3\,\mathrm{s}^{-1}$, but the damage also depends on the exposure time. Different surfaces might also have an influence on hemolysis, but we have, however, not addressed this problem. Hemolysis can experimentally be monitored by measuring the concentration of hemoglobin released to the extracellular medium.

Chapter 4

Experimental Work

The experimental part of this project involves measurements of blood's viscosity in a shear flow with a rotational rheometer. Since blood is a particulate fluid, it could be expected that the constitutive equation was dependent on the gap between the shearing plates. For the investigation of gap dependency we used a parallel plate geometry. The gap size was varied between 70 and 1000 μm. However, analysis carried out after the measurements showed that only measurements at 1000 μm were valid. Before the actual measurements are presented, we will briefly introduce the used instruments, and the formulas that enable us to calculate the viscosity for a non-Newtonian fluid.

4.1 Preparation of blood samples

For the measurements we used a portion of outdated whole human blood, delivered from the blood bank at *Rigshospitalet* [17]. Biological samples that are potentially harmful should be handled in a class 3 laboratory [6], which is a facility that MIC does not have yet. Outdated blood from a hospital is screened for HIV, hepatitis C, and other diseases, and the potential risk of handling the sample in a standard laboratory is therefore minimal.

To be able to reproduce data, it is necessary to know the hematocrit. The hematocrit can be measured in a microhematocrit centrifuge. However, at the present time MIC is not equipped with such an instrument. It was, therefore, chosen only to make measurements on the non-diluted sample from the hospital.

The blood had a hematocrit at about 60%, and was anticoagulated with sodium citrate. After use the equipment was washed in water and disinfected with ethanol. The blood was stored at 4 °C. The rheometer has a built-in thermoelement, Peltier element, on the stationary wall, which ensures a constant temperature during the measurements. An elevation of the sample temperature from 4 to 20 °C is obtained within a minute.

From a rheological point of view, blood is a complex fluid, and it was

therefore chosen also to perform measurements with two non-particulate Newtonian fluids. With this control we can trace effects due to the measuring technique. The reference fluids was water and an engine oil, with a lower and higher viscosity than blood, respectively.

Furthermore, during the project it was found that one of the geometries was damaged. That is to say, the plate in the parallel plate geometry was skewed in such a way that it made small wobbles from side to side under operation. This is clearly a problem for the accuracy of the measurements.

4.2 Techniques for measuring viscosity

The rhoemetry was performed with an AR 2000 Advanced Rheometer from TA-instruments, which can measure fluid properties in various geometries.

In the software it was possible to select different procedures, depending on the properties to be measured. For these measurements we used the *creep* and *flow* procedure. In the *creep* procedure a constant shear stress is specified, and the duration for the experiment. When the stress is applied, the flow field develops in time. This kind of measurements was used to examine the time dependence of the viscosity.

For the *flow* procedure a stress interval, and a tolerance for viscosity is specified. In this way we obtain the steady state shearing viscosities for different shear rates. A steady state was chosen as a 5 % tolerance in three consecutive measurements of 10 s.

The rheometer is torque controlled. However, it is also possible to specify a shear rate, as the instrument is able to calculate the required torque for a given shear rate. For fluids with small viscosities it is recommended to use the stress controlled sweep.

The valid torque range for the rheometer is from 0.1 to $2 \times 10^5\,\mu$Nm. To ensure that we are operating in a proper interval, it can be helpful to show data of the torque next to the viscosity, when the results are analyzed. Close to the limits the data will be more scattered and less reliable.

4.2.1 The concentric cylinders rheometer

Figure 4.1 shows the concentric cylinder geometry. In this geometry both *creep* flow and *flow* experiments was performed, on blood only. The inner cylinder is rotating, and the instrument registers the applied torque and angular velocity.

The geometry requires a sample size of about 10 mL. The lid, not shown on the figure, on top of the cup provides an atmosphere with a high humidity, and no problems were observed with skin formation in the blood air interface, which is a problem observed in the parallel disk geometry.

A rheometer can measure the normal forces, torque $\mathcal{T}$, and angular velocity ω. The torque is related to the shear stress, and the angular velocity

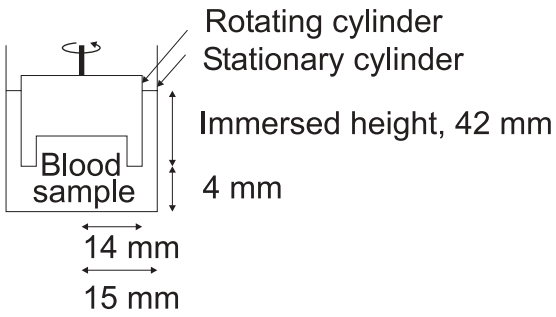

Figure 4.1: Sketch of the recessed concentric aluminum cylinders

is related to the shear rate. Thus, we have all the necessary properties to calculate the viscosity. The torque on the inner cylinder in a cylindrical coordinate system is given by

$$\mathcal{T} = R_1 \int_0^{2\pi} \int_0^H \tau_{r\theta} \, dz \, d\theta = 2\pi R_1 \int_0^H \eta\dot{\gamma} \, dz. \tag{4.1}$$

We shall not be concerned with normal forces, even though it might have some influence in complex geometries such as a sudden contraction.

We shall derive an expression for the viscosity as a function of the torque and angular velocity, when it is assumed that the gap ϵ between the inner and outer radius is small

$$R_2 - R_1 = \epsilon, \; R_1 \ll \epsilon, \tag{4.2}$$

where ϵ is a small number. A consequence is that the velocity field can be assumed to decrease linearly between the two plates, i.e., the shear rate is constant.

The equation of motion for the circular annular flow is

$$0 = \frac{1}{r^2} \frac{d}{dr}(r^2 \tau_{r\theta}), \tag{4.3}$$

with the solution

$$\tau_{r\theta} = \frac{c}{r^2}. \tag{4.4}$$

where c is a constant of integration. The stress expression for the generalized Newtonian fluid in cylindrical coordinates is

$$\tau_{r\theta} = \eta \, \dot{\gamma}, \tag{4.5}$$

where

$$\dot{\gamma} = r \frac{d}{dr} \frac{v_\theta}{r}. \tag{4.6}$$

Combining the Eqs. (4.3) and (4.5) gives a nonlinear ordinary inhomogeneous first order differential equation

$$\frac{dv_\theta}{dr} - \frac{v_\theta}{r} = \frac{c_1}{\eta r^2}, \tag{4.7}$$

with boundary conditions

$$v_\theta(R_1) = \omega R_1, \quad v_\theta(R_2) = 0. \tag{4.8}$$

Because of the small distance between the cylinders the velocity field is decreasing linearly in the radial distance, which means the viscosity is constant. This is true for a Newtonian liquid, but the assumption will probably be more critical as the nonlinearity of the constitutive equation increases. The assumption could be studied analytically. However, we shall assume it as a good simplification, and Eq. (4.7) reduces to a linear problem with the solution

$$v_\theta(r) = r\left[\frac{\omega(R_1R_2)^2}{R_2^2 - R_1^2}\left(\frac{r^2 - R_1^2}{(R_1 r)^2}\right) + \omega\right], \tag{4.9}$$

where the shear rate is

$$\dot{\gamma} = \frac{2\omega R_1^2 R_2^2}{R_2^2 - R_1^2}\frac{1}{r^2}. \tag{4.10}$$

Remembering $\dot{\gamma}$ is in cylindrical coordinates, the approximation in Eq. (4.2) gives

$$\dot{\gamma} = \frac{\omega R_1}{R_2 - R_1}, \tag{4.11}$$

and the relation for the apparent viscosity can be expressed as

$$\eta(\dot{\gamma}) = \frac{\mathcal{T}}{2\pi H \dot{\gamma} R_1}, \tag{4.12}$$

where H is the immersed height of the inner cylinder.

4.2.2 The parallel disk rheometer

In the parallel disk geometry, Fig. 4.2, there were performed *flow* experiments for different gap sizes 1000, 500, 250, 100 and 70 μm, where 1000 μm is expected to yield the same results as for the concentric cylinders. Therefore, gap sizes above this value is considered as being in the macroscopic range, which means that we measure a bulk property. As mentioned, the geometry was damaged and two Newtonian fluids were used as a control.

In the manual for the rheometer [23], it is pointed out that the geometry should be properly loaded as shown in Fig. 4.2. However, for blood it was necessary with an extra spill to prevent sticking of the rotating plate. Otherwise, a skin started to form in the air fluid interface. For low viscous fluids the effect of an overfilled geometry is small. It is assumed that the incorrect

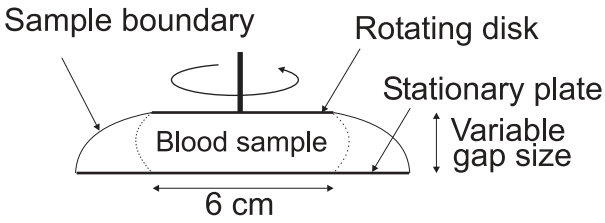

Figure 4.2: Sketch of the parallel aluminum disk rheometer. The dotted line is indicating the boundary, when the rheometer is filled correctly, i.e, the sample is exactly covered by the rotating disk. In the experiments, the rheometer was overfilled to prevent influence from skin formation.

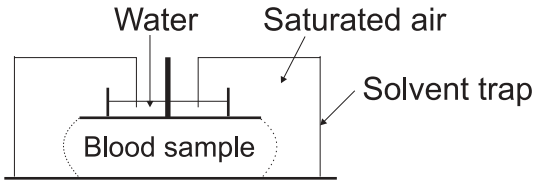

Figure 4.3: Sketch of the solvent trap. For more details on the specific geometry, see Fig. 4.2.

loading of the geometry had a negligible influence on the measurements. The skin formation on the liquid-gas interface could probably be avoided, if the surrounding air was saturated with water vapor. For this purpose TA-instruments have developed a solvent trap as sketched in Fig. 4.3. However, the solvent trap was not available in the laboratory. It was chosen not to request for a solvent trap, as the problem was solved by overfilling the rheometer. It was also tried to shield the rheometer with aluminum foil to reduce convection, but the effect seemed to be minimal.

The parallel disk is a somewhat more complex geometry than the concentric cylinders, as the flow field is variable in both the radial and axial direction. We shall derive an expression for the relation between apparent viscosity and torque assuming that the components of the velocity vector is given by

$$v_\theta(r,z) = r\omega(z), \quad v_r = v_z = 0 \tag{4.13}$$

in a cylindrical coordinate system. A more detailed derivation can be seen in Bird et al. [3]. As v_θ is linearly dependent on r, the $\dot{\gamma}_{r\theta}$ component

disappears from the shear rate tensor

$$\begin{aligned}\dot{\boldsymbol{\gamma}} &= \frac{1}{2}\left[(\boldsymbol{\nabla}\mathbf{v}) + (\boldsymbol{\nabla}\mathbf{v})^T\right] \\ &= \frac{1}{2}\left[\begin{pmatrix} 0 & \frac{dv_\theta}{dr} & 0 \\ -\frac{v_\theta}{r} & 0 & 0 \\ 0 & \frac{dv_\theta}{dz} & 0 \end{pmatrix} + \begin{pmatrix} 0 & -\frac{v_\theta}{r} & 0 \\ \frac{dv_\theta}{dr} & 0 & \frac{dv_\theta}{dz} \\ 0 & 0 & 0 \end{pmatrix}\right] \\ &= \frac{1}{2}\begin{pmatrix} 0 & 0 & 0 \\ 0 & 0 & \frac{dv_\theta}{dz} \\ 0 & \frac{dv_\theta}{dz} & 0 \end{pmatrix} \end{aligned} \tag{4.14}$$

As the only nonzero value of the stress tensor is the rz entry, the θ component of the dynamical equation is

$$0 = \frac{d\tau_{z\theta}}{dz} = \frac{d\eta\dot{\gamma}}{dz}, \tag{4.15}$$

which states that the shear rate is independent of z. From Eq. (4.13) we have

$$\dot{\gamma}_{z\theta} = \frac{r\omega}{H}. \tag{4.16}$$

The shear rate varies in the radial direction. Let $\dot{\gamma}_R$ be the shear rate at the rim, $r = R$.

$$\frac{\dot{\gamma}}{\dot{\gamma}_R} = \frac{r}{R}. \tag{4.17}$$

The required torque to maintain a steady flow is given by

$$\mathcal{T} = \int_0^\pi \int_0^R \tau_{z\theta} r^2 dr = 2\pi \int_0^R \eta\dot{\gamma} r^2 dr = \frac{2\pi R^3}{\dot{\gamma}_R^3} \int_0^{\dot{\gamma}_R} \eta\dot{\gamma}^3 d\dot{\gamma}. \tag{4.18}$$

Differentiating after $\dot{\gamma}$ and isolating η leads to

$$\eta(\dot{\gamma}_R) = \frac{\mathcal{T}}{2\pi R^3 \dot{\gamma}_R}\Big(3 + \frac{1}{2\pi R^3}\frac{d\ln\mathcal{T}}{d\ln\dot{\gamma}_R}\Big). \tag{4.19}$$

This is the basis for obtaining the non-Newtonian viscosity from the measured torque and shear rate in a parallel disk geometry.

4.3 Performed measurements

Let us start with a short overview of the experiments. Firstly, I performed measurements in a creep flow to investigate time dependence of the viscosity. In a creep flow we measure the viscosity at a constant applied shear stress. Secondly, I investigated the gap size dependence of the viscosity in a parallel disk geometry. However, measurements on Newtonian fluids showed that the uncertainty on small gap sizes was to large. Still, a constitutive equation for whole human blood was obtained in the macroscopic regime.

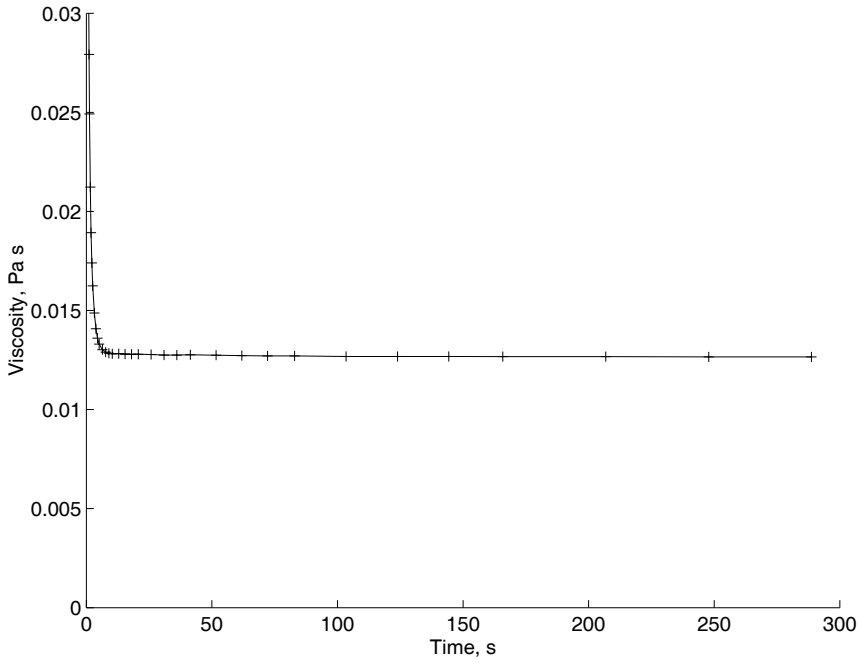

Figure 4.4: Concentric cylinders geometry, creep flow. The maximum shear rate is 2370 s^{-1}. The viscosity for a shear rate at 2370 s^{-1} is constant over 300 s

.

4.3.1 Hemolysis monitored by viscosity in a creep flow

The red blood cells contributes significantly to bloods viscosity. As it is known that cells can lyse or rupture due to shear stress, it is, as a first approach, a good idea to test the blood in a *creep* experiment. If the viscosity is constant over time there is probably only little hemolysis.

In Fig. 4.4 it is seen that the viscosity is constant for a 30 kPa applied stress in 300 s. The final shear rate is 2370 s^{-1}, and is obtained after 210 s. In conclusion, there is no detectable hemolysis due to the shear or contact with the non-biological, aluminum surface.

4.3.2 Measurements of viscosity down to microrange

One of the objectives of this project, was to investigate if we could measure any changes in the viscosity, when the system is taken from the macroscopic to the microscopic range.

With an undamaged instrument there should not be any problems in obtaining the steady shear viscosity with a rotating disk. However, the actual skewness was small and it was therefore not recognized from the beginning. After the first set of measurements some unexpected characteristics was discovered at high shear rates, and it was therefore decided to make additional

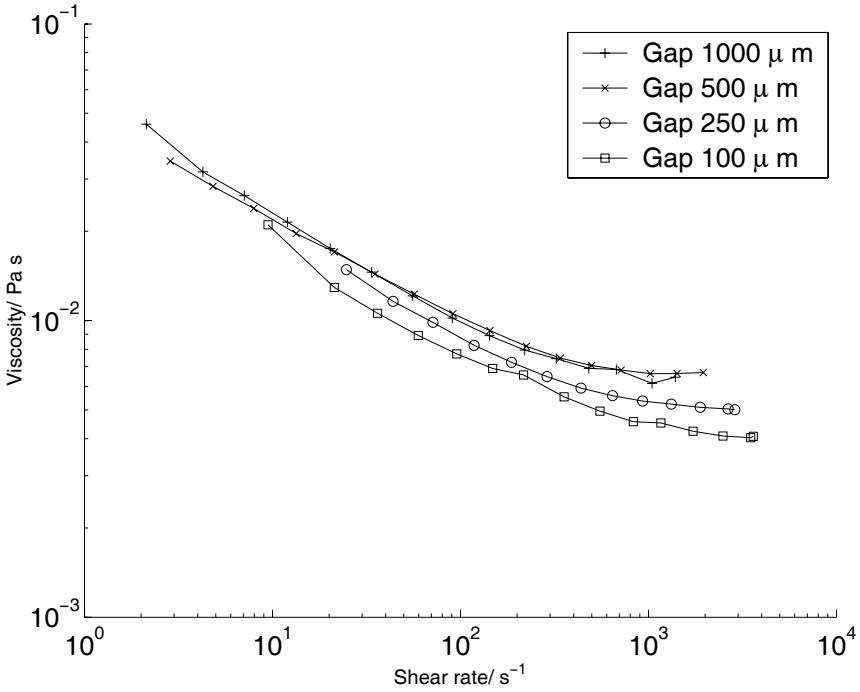

Figure 4.5: The figure shows the viscosity of blood as a function of the shear rate for different gaps between the shearing plates at 20 °C.The hematocrit is 60. The figure indicates that there might be a systematic drop in the viscosity with decreasing gap size. However, this effect was also observed for water, Fig. 4.6.

experiments on a Newtonian fluids to test the uncertainty of the rheometer. From these measurements, it was found that this approach had to be modified to study the gap size dependency. Figure 4.5 shows the viscosity measurements for whole human blood at different gap sizes. It is noticed that the viscosity is shear thinning as was expected. According to the figure it is also seen that the viscosity is decreasing with the gap size even at high shear rates. However, Barbee and Cokelet [10] showed that, at high shear rates, the viscosity of blood in different sized microtubes only depends on the hematocrit and mean velocity divided by the tube radius. This contradiction suggests that there could be an artefact due to the measuring method.

Figure 4.6 shows water's viscosity as a function of the shear rate for different gap sizes. The viscosity of water is $10^{-3}\,\mathrm{Pa\,s}$. For a gap size of $1000\,\mu$m there is a wobble at small shear rates, and at $200\,\mathrm{s}^{-1}$ the viscosity increases due to inertial effects, i.e., a secondary flow is developing.

For $H = 500\,\mu$m and $H = 250\,\mu$m the inertial effects are suppressed, but there is still unacceptable wobbles at low shear rates due to the skewed instrument. For $H = 100\,\mu$m the viscosity is significantly lowered, which

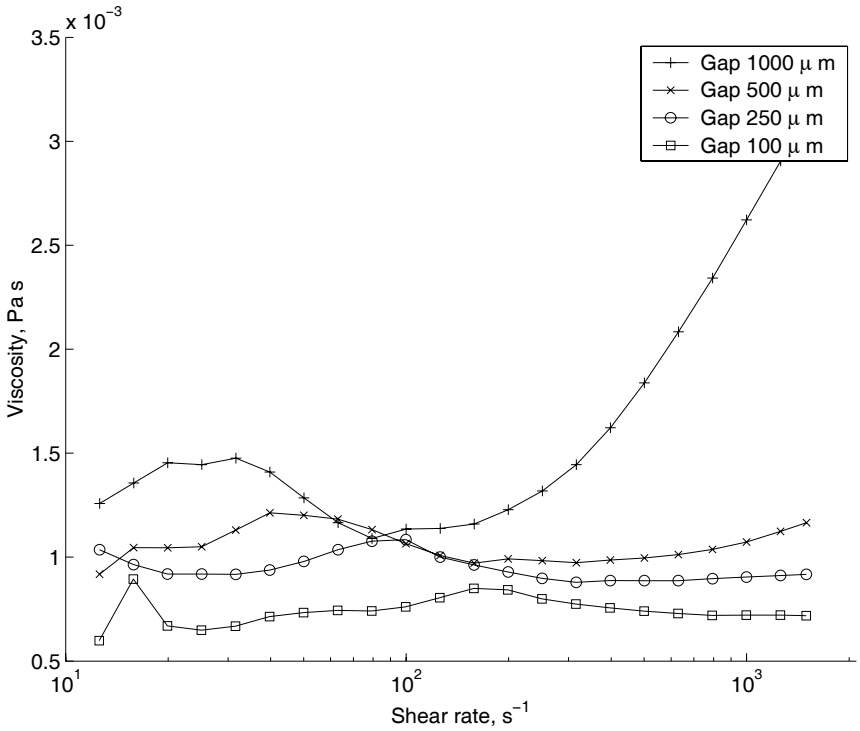

Figure 4.6: The figure shows the viscosity of water as a function of the shear rate for different gap sizes. The temperature was 20 °C. Water is a Newtonian liquid and should be independent of the gap size. However, a small but systematic wobble seems to appear in the data. The wobble travels to the right, as the gap size decreases. As water molecules are very small compared to the gap size, it is expected that we measure the bulk properties at any of the chosen gap sizes. Therefore it is unexpected that there seems to be a systematic drop in the viscosity with decreasing gap size. A skewed disk could be the reason. For a 1000 μm gap inertial effects are observed above 200 s^{-1}. The points are connected to guide the eye.

means the data in this range are not reliable.

Figure 4.7 shows the viscosity measurements for a Newtonian engine oil. It is somewhat easier to get more stable data for a fluid with a higher viscosity. The viscosity of the oil is higher than for blood, and suppresses the inertial effect even at a 1000 μm gap size. However, Fig. 4.7 indicates that the measurements for $H = 250\,\mu$m is unreliable.

Taking the former measurements into account, the uncertainty of the rheometer is to large, and we can not draw any conclusions about the gap size dependency. This approach with the available geometries has shown unappropriate to investigate gap size dependency.

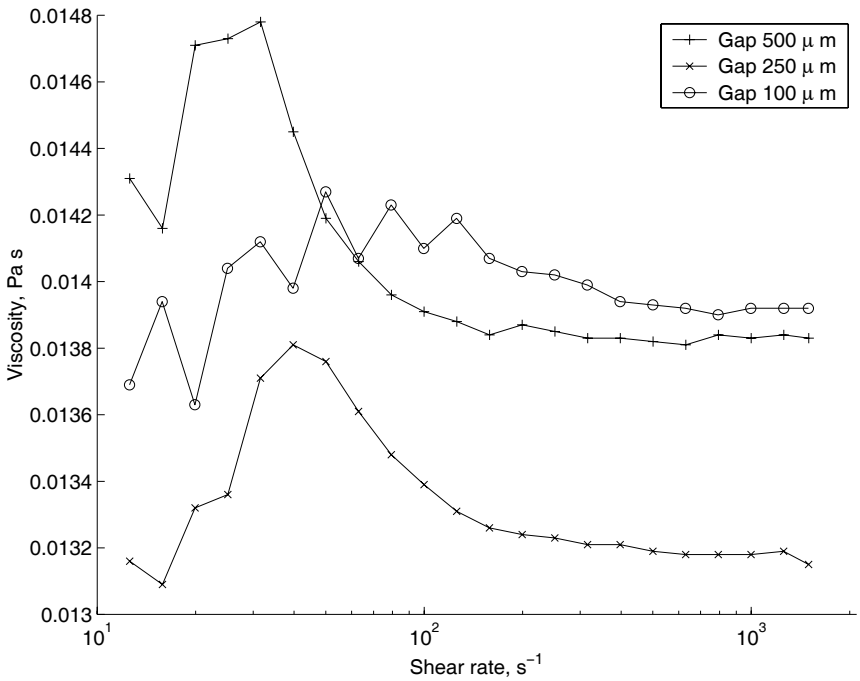

Figure 4.7: The figure shows the viscosity of an engine oil for different gaps between the shearing plates at 20 °C. The fluid is Newtonian and non-particulate, which means the viscosity should be constant and independent of the gap size. In contrast to the viscosity of water in Fig. 4.6, the viscosity of the oil does not drop with decreasing gap size. Anyhow, there is still a systematic wobble on the graphs. The two figures, Fig. 4.6 and 4.7, indicates that any apparent gap size dependence might be due to the rheometer. Furthermore, the wobbles introduce an uncertainty that have to be considered. The data points are connected to guide the eye.

4.3.3 Obtaining parameters for the constitutive equation

For a modelling purpose the constitutive equation is the link between material properties and flow behavior. In the foregoing section, it was seen that the uncertainty for the measurements increased, when the gap size was decreased. Anyhow, we may still expect some validity for gap sizes above $500\,\mu$m. When we are measuring the macroscopic viscosity, the results should be independent of the chosen geometry. In Fig. 4.8 is seen a comparison between measurements on blood in the concentric cylinders and in the parallel disk geometry for $H = 1000\,\mu$m. The results are in a fine agreement, and we shall therefore derive a constitutive equation from the concentric cylinder data. Fitting a power law model in the range of $0.95 - 140\,\mathrm{s}^{-1}$ gives

$$\tau = 0.057\,\dot{\gamma}^{0.623}. \tag{4.20}$$

To see if the magnitude and non-Newtonianness of our blood measure-

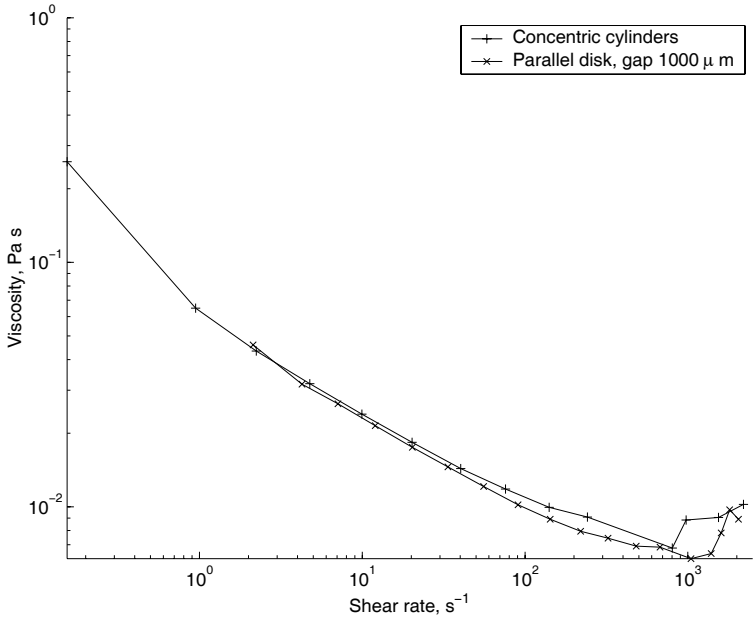

Figure 4.8: A comparison between measurements on blood from two different geometries, concentric cylinders and parallel disk. The temperature was 20 °C and the hematocrit was 60. As the viscosity is independent of the geometry, we interpret these curves as being the bulk viscosity for blood. The program TA Data Analysis from TA instruments was used to make a least squares fit. In the range $0.95 - 140\,\mathrm{s}^{-1}$ it was found reasonable to fit the data to a power law.

ments is comparable with similar measurements in the literature, I have collected a selection of constitutive equations in Fig. 4.9. The figure shows that the results from the concentric cylinders are comparable, but somewhat more non-Newtonian than measurements from the literature. The most similar curve is Walburn and Schneck's best two variable model (BTVM) with a hematocrit at 70 %. The hematocrit is 10 % higher than our sample. However, the BTVM is derived for blood at 37 °C instead of 20 °C. It is noticed that results from oscillating rheometers are less non-Newtonian compared to measurements with a rotational geometry. We will take a closer look on fluid properties in an oscillatory flow, in the following section.

4.4 Viscoelastic properties of blood

When a strategy or an approach turns out to be inappropriate, it is necessary to refine theory or experiments. As seen in Fig. 4.9, some viscosity measurements are obtained in an oscillating tube flow. If the viscosity can be obtained by small amplitude oscillatory measurements in the parallel disk geometry, it might be possible to avoid artifacts due to the skewness.

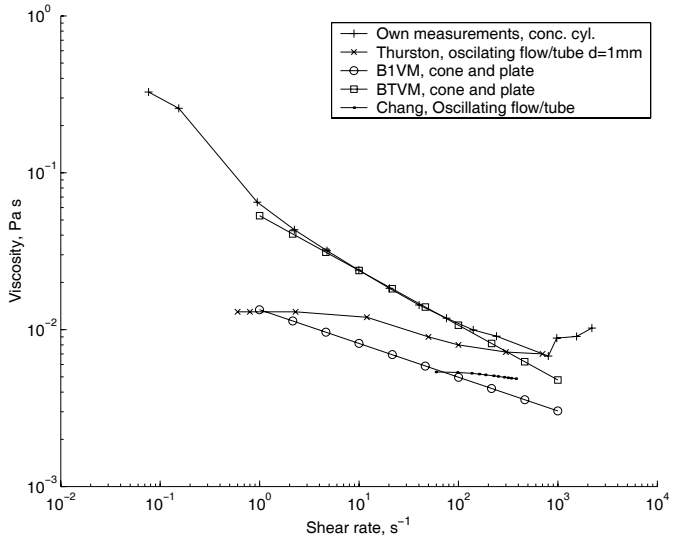

Figure 4.9: Comparison of present results with the literature. The curves are not supposed to be identical as they are measured on different samples. Own measurements: Human blood, $Hem = 60\,\%$, $T = 20\,^{\circ}\mathrm{C}$. Thurston [24]: Human blood, $Hem = 45\,\%$, $T = 22\,^{\circ}\mathrm{C}$. Chang et al.[5]: Defibrinated Sheep blood, $Hem = 41\,\%$, $T = 23\,^{\circ}\mathrm{C}$. BTVM, Walburn and Schneck [29]: Human blood, $T = 37\,^{\circ}\mathrm{C}$, $Hem = 70\,\%$. B1VM, Walburn and Schneck [29]: Human blood, $T = 37\,^{\circ}\mathrm{C}$, $Hem = 35 - 50\,\%$.

However, it was also noticed in the figure that viscosities measured in the rotational flow were slightly more non-Newtonian. In this section, we shall take a closer look on the differences between the viscoelastic shearing viscosity η_V and the shearing viscosity η_s.

Viscoelastic properties can be measured in an oscillatory flow and reveals information about energy stored and dissipated in the system. Furthermore, if the measurements can be combined with an appropriate model, it is possible to obtain a better understanding of relaxation times for the fluid in consideration. In this section, we will briefly introduce the theory of small amplitude oscillatory flow and apply a spring-dashpot model for blood. Additionally we will discuss the relation between the shearing viscosity η_s, low shear rate frequency dependent viscoelasticity $\eta^*(\Omega)$, and the shear rate dependent viscoelasticity $\eta^*(\dot{\gamma})$. This relation can according to Thurston [25] be described by a degradation formula, which models the degradation of aggregates, rouleaux.

As it became evident in the previous section, rotational viscometric measurements ceased to be valid when the gap size between the rotating disk and stationary plate became small. This was due to a skewness in the disk, and the motivation for looking at small amplitude oscillatory flow was to find a way to minimize this effect. In contrast to a rotating disk, a small

amplitude oscillating disk is measuring over the same point.

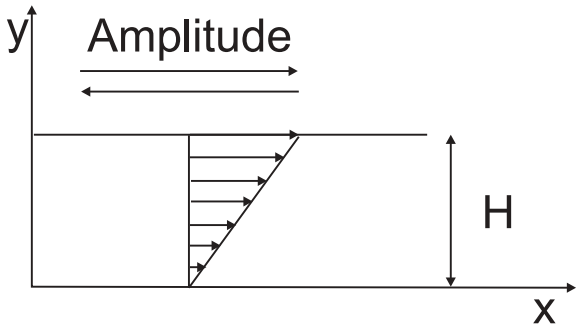

Figure 4.10: The figure shows the velocity profile of a small amplitude oscillatory flow between to parallel plates. When the amplitude is small the velocity profile is instantaneous.

.

Figure 4.10 shows the instantaneous velocity profile in a small amplitude oscillatory flow between two plates. If the fluid is Newtonian the shear rate and shear stress will be in phase. However, for blood the shear stress is shifted with the phase ϕ,

$$\dot{\gamma} = \dot{\gamma}^o \cos(\Omega t), \tag{4.21}$$

$$\tau = A(\Omega)\dot{\gamma}^o \cos(\Omega t - \phi), \quad \text{and} \tag{4.22}$$

$$0 \leq \phi \leq \frac{\pi}{2}, \tag{4.23}$$

where $\dot{\gamma}^0$ is the shear rate amplitude, Ω the frequency and A is a frequency dependent function. The criterium for linearity is

$$\frac{\Omega \rho H^2}{2\eta_0} \ll 1, \tag{4.24}$$

where η_0 is the viscosity at small frequencies [3]. For calculational purposes the shear stress is expressed with complex notation

$$\tau = \mathrm{Re}\left\{A(\Omega)\dot{\gamma}^o e^{i(\Omega t - \phi)}\right\} = \mathrm{Re}\left\{\tau^o e^{i\Omega t}\right\}. \tag{4.25}$$

A common feature for the linear viscoelastic model is that the shear stress can be expressed by an integral of the relaxation modulus G and the shear rate

$$\tau = \int_{-\infty}^{t} G(t - t')\dot{\gamma}\, dt'. \tag{4.26}$$

We will later verify Eq. (4.26) by noting that it is satisfied for the generalized Maxwell model, but it is, however, a general structure for the solution of a

first order inhomogeneous differential equation. The complex viscosity η^* is obtained as the relation between the complex shear stress, and shear rate

$$\eta^* = \frac{\tau^*}{\dot{\gamma}^*} = \frac{\tau^o}{\dot{\gamma}^o}, \tag{4.27}$$

where superscript o indicates an amplitude. τ^o is in general complex, $\dot{\gamma}^o$ is real, and the complex shear rate and shear stress are defined as

$$\tau^* = \tau^o e^{i\Omega t'} \quad \text{,and} \quad \dot{\gamma}^* = \dot{\gamma}^o e^{i\Omega t'}, \tag{4.28}$$

respectively. We will now derive an expression for the complex viscosity by means of the relaxation modulus G. Substituting with $s = (t - t')$ Eq. (4.26) can be rewritten as

$$\begin{aligned} \tau &= -\int_{\infty}^{0} G(s)\dot{\gamma^o}\mathrm{Re}\left\{e^{i\Omega(t-s)}\right\} ds \\ &= \dot{\gamma}^o \mathrm{Re}\left\{e^{i\Omega t}\right\} \int_0^{\infty} G(s)\mathrm{Re}\left\{e^{-i\Omega s}\right\} ds. \end{aligned} \tag{4.29}$$

The complex shear stress is then

$$\tau^* = \dot{\gamma}^o e^{i\Omega t} \int_0^{\infty} G(s) e^{-i\Omega s} ds = \dot{\gamma}^* \eta^*, \tag{4.30}$$

where η^* is identified as

$$\eta^* = \int_0^{\infty} G(s) e^{-i\Omega s} ds. \tag{4.31}$$

4.4.1 A generalized Maxwell model for blood

A Maxwell body is a component in a mechanical system, which is composed of a dashpot and a spring to resemble friction and conservation of energy, respectively. A general Maxwell model is a series of Maxwell bodies connected in parallel. The model we shall use for blood is shown by Thurston [25] and is seen in Fig. 4.11. It is a generalized Maxwell model with the addition of one extra dashpot, to represent the viscosity at infinite shear rates. The velocity of a Maxwell body is given by

$$\dot{x} = \dot{x}_k + \dot{x}_\eta = \frac{\dot{F}}{k} + \frac{F}{\eta}, \tag{4.32}$$

where x_k and x_η is the velocity of the individual components. A standard solution to this linear ordinary first order inhomogeneous differential equation is

$$F = e^{-\int \frac{k}{\eta} dt} \left[\int k\dot{x} e^{\frac{k}{\eta} t'} dt' + K \right] = e^{-\frac{1}{\lambda} t'} \left[\int k\dot{x} e^{\frac{1}{\lambda} t'} dt' + K \right], \tag{4.33}$$

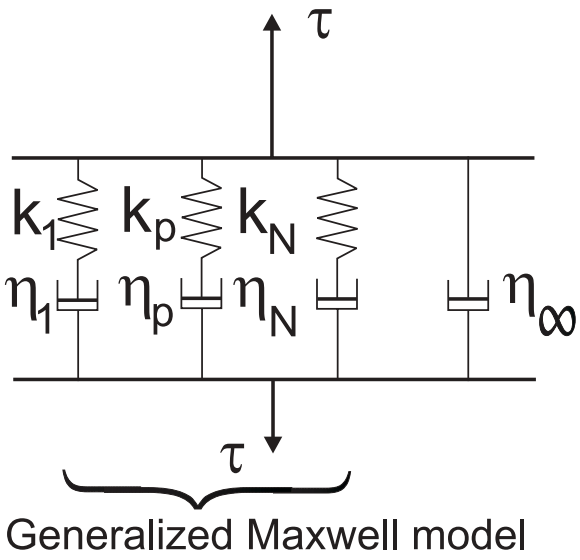

Figure 4.11: The figure shows a generalized Maxwell model, where an extra dashpot has been added to model the shear limit behavior. N is the total number of Maxwell bodies.

.

where λ is a time relaxation parameter $\lambda = k/\eta$. If we choose the limits $-\infty \leq t' \leq t$, and $F = 0$ at $t = -\infty$ then the integration constant must vanish, $K = 0$. Changing the equation from terms of force to stress and inserting the limits into Eq. (4.33) gives

$$\tau = e^{-\frac{t}{\lambda}} \int_{-\infty}^{t} k\dot{\gamma} e^{\frac{t'}{\lambda}} dt' = \int_{-\infty}^{t} k\dot{\gamma} e^{\frac{-(t-t')}{\lambda}} dt'. \tag{4.34}$$

Substituting $s = t - t'$ into Eq. (4.34) and changing to complex notation yields

$$\tau^* = \dot{\gamma}^o e^{i\Omega t} \int_0^{\infty} k e^{-\left(\frac{s}{\lambda} + i\Omega s\right)} ds = \dot{\gamma}^* \int_0^{\infty} k e^{-\frac{s}{\lambda}} e^{-i\Omega s} ds. \tag{4.35}$$

The complex viscosity can be calculated by identifying $G_p(s)$, and evaluating Eq. (4.31)

$$G_p(s) = e^{-\frac{s}{\lambda_p}}, \text{ and } \quad \eta_p^* = \int_0^{\infty} G_p(s) e^{-i\Omega s} ds = \frac{\eta_p}{1 + i\Omega\lambda_p}, \tag{4.36}$$

where p indicates the pth Maxwell body. The total complex viscosity is given by

$$\eta^* = \eta_\infty + \sum_{p=0}^{\infty} \eta_p^*. \tag{4.37}$$

The dashpots are related to the dissipation of energy due to friction, which suggests that the shearing viscosity is

$$\eta_s = \eta_\infty + \sum_{p=0}^{\infty} \eta_p. \tag{4.38}$$

However, small amplitude oscillatory measurements only applies to small values of the shear rate, and we, therefore, need a relation to extend the parameters to higher shear rates.

For small shear rates, and small amplitudes the system is very close to what we shall refer to as a static equilibrium state. Furthermore, when $\Omega \to 0$ η_V and η_s approaches the same limiting value. For the ground state we assume that

$$\eta_o = \lim_{\Omega\to 0}\lim_{\dot\gamma\to 0} \eta_V = \lim_{\dot\gamma_s\to 0} \eta_s \quad \text{, and} \quad \lim_{\Omega\to 0}\lim_{\dot\gamma\to 0} \eta_E = 0, \tag{4.39}$$

where subscript o identifies the ground state, η_v and η_E are defined by

$$\eta^* = \eta_V - i\eta_E. \tag{4.40}$$

V is related to viscous dissipation of energy, and E to elastic storage of energy.

When the shear rate is increased, large aggregates of blood cells are broken down which reduces the viscosity. It is believed that the relaxation times λ_p of the aggregates are independent of the shear. It has been shown that these features can be modelled by the degradation function F

$$\eta_p = \eta_{o,p} F(\dot\gamma\lambda_p) \quad \text{, and} \quad k_p = k_{o,p} F(\gamma\dot\lambda_p), \tag{4.41}$$

where

$$F(\dot\gamma\lambda_p) = \frac{1}{1 + (\dot\gamma\lambda_p)^2}. \tag{4.42}$$

By means of the degradation formula and ground state values for the rheological parameters, we can calculate the value of the rheological parameters at states of dynamical equilibrium, i.e., we can estimate the steady state shearing viscosity.

To resume the key ideas of small amplitude oscillatory measurements in connection with a spring-dashpot model: Small amplitude measurements yield the complex viscosity. The infinite shearing viscosity η_∞ can be measured in a shear flow, e.g., a rotational viscometer. By the use of Eqs. (4.36) and (4.37), we can by curve fitting estimate the shear related viscosities for the individual aggregates, η_p. The total shearing viscosity is then obtained by Eq. (4.38)

One of the objectives of small amplitude oscillatory viscosity measurements was to avoid the rotational viscometer. As we need the infinite shearing viscosity to calculate the viscosity at lower shear rates, it seems like

the effects from the skewed geometry cannot be avoided. However, it was showed by Barbee and Cokelet Fig. 3.11(b) that the infinite viscosity did not depend on the size of the used geometry. The infinite viscosity could therefore be measured in any geometry.

To sum up the experiences from the experimental work, we saw that there were no significant change in viscosity over time at shear rates below $2370\,\mathrm{s}^{-1}$, which is of the same order as the shear rates in the *flow* procedure.

If a rotating geometry is chosen to investigate the viscosity's dependency on gap size, there are high demands to the precision of the rotating disk. However, we obtained a macroscopic constitutive equation.

It is possible that the experiment can be performed by small amplitude oscillatory measurements. However, shearing viscosity and viscoelastic viscosities are not the same. The viscoelastic shearing viscosity is the real part of Eq. (4.37), and the shearing viscositiy is given by Eq. (4.38). From Fig. 4.9 it was seen that viscoelastic measurements are less non-Newtonian. However, I have mention that I assume Chang et al. [5] used η_V as it has more similarities with Thurstons measurements than my own; this could also be due to the lack of fibrinogen. In general η_V is smaller than η_s. This can be seen in the paper by Thurston [25], but it is also seen indirectly from the relation

$$\eta_p^* = \frac{\eta_p}{1 + i\Omega\lambda_p}, \tag{4.43}$$

as η_V is related to $\mathrm{Re}\{\eta_p^*\}$, and η_s to η_p. When the frequency is approaching zero, the viscoelastic and shearing viscosity are converging. At high shear rates they are coinciding as all the aggregates are broken down. This is the feature of the degradation function, Eq.(4.41).

Thurston mentions [25] that the viscoelastic viscosity should be considered in a pulsatile flow, as it can be regarded as a superposition of an oscillatory and a shear flow.

Chapter 5

Numerics and Simulations

Numerical calculations is a tool to get a better understanding of a physical system, where analytical solutions can be difficult to obtain. Simulation is a term for the iterative process of obtaining a solution, and this technique has in particular proven successful for optimization and design of various devices such as pumps and engines.

Simulations can also be used as a tool to speed up the designing process of microfluidic systems. However, theory from modelling in macroscopic systems are not necessarily valid as we scale down the system. In this chapter, we shall investigate the applications of the measured constitutive equation, Eq. (4.20).

In a paper by Chang et al. [5] the power law has been used as a constitutive equation to obtain quantities of flow resistances in different microfabricated geometries. They succeeded to show that the power law can be used to predict the relation between applied pressure and volume flow rates for simple geometries. However, their studies do not show any details about velocity profiles and shear rates within the system.

Hemolysis can be induced by high shear rates, which for some purposes is an unwanted process, as for example in quantifying potassium levels [5]. A better understanding, and quantification of the shear rates in the different geometries, can be helpful in the design of microfluidic systems manipulating blood.

A problem that has to be addressed before we interpret the numerical results is validation of the CFD-code. Even if it has proven successful in some problems, it might be invalid in other cases. The success of an analytical solution is dependent on how well the real system is described by the mathematical equations. If we approach the problem with a numerical method the solution will also be dependent on the discretization of the governing equations. Even if the equations are properly discretized it can be difficult to obtain a stable solution, i.e., the residuals in the iteration procedure do not decrease. A way to ensure that the results obtained by

means of CFD are correct, is to test against analytical solutions or experimental work. Flow systems can be very complex, and it can be necessary to make a number of assumptions to solve the problem analytically. If, for the simplified case, there is an agreement between the two solutions, we have a good foundation for taking a step toward a more realistic system, where we have to rely on numerics. This shall be the approach to CFD-solutions in this report.

5.1 Computational Fluid Dynamics in CFD-ACE+

In the project we shall solve the flow problems aided by a commercial software package from CFD Research Corporation [8], CFD-ACE+ version 6.6 release 2002. The central programs of this package are CFD-GEOM, CFD-GUI, and CFD-VIEW. In general, the solution of a CFD-Problem can be divided into three elements: a pre-processor, a solver, and a post-processor. The pre-processing is handled in CFD-GEOM and CFD-GUI. The first program is for geometry and grid generation, and the latter is a graphical user interface for specifying the required fluid properties, boundary and initial conditions.

The solver is of the finite volume type. Solver options like relaxation parameters, number of iterations and interpolation schemes are also set in CFD-GUI.

During a simulation a number or a single file containing flow properties is produced, and these data can be viewed and manipulated in CFD-VIEW, the post-processor.

5.1.1 Discretization of the governing equations

The equation of motion and the continuity equation is in its most general form a set of nonlinear PDEs. The first step in the solution procedure is therefore to discretize in time and space. The transient term of Eq. (2.15) is given by

$$\rho\frac{\partial \mathbf{v}}{\partial t} = \frac{(\rho\mathbf{v})_{t+\Delta t} - (\rho\mathbf{v})_t}{\Delta t}, \tag{5.1}$$

where Δt is specified by the user. The spatial terms are discretized by dividing the geometry into a number of cells as seen in Fig. 5.1. The fluid properties are stored at each cell center. However, some properties like the stress has to be evaluated at the interface of the cells. For that purpose it is possible to choose different interpolation methods as for example the central or the upwind differencing scheme. In the former a linear dependence is assumed between the node values and in the latter the properties are assigned according to the upwind scheme. If the flow goes west, the surface

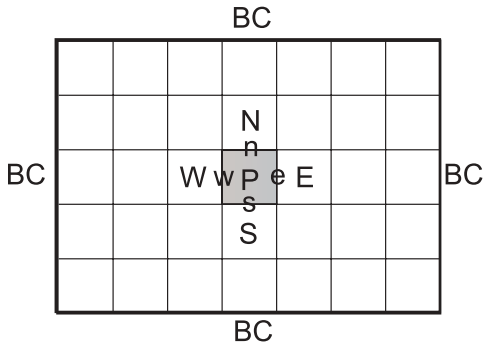

Figure 5.1: The figure shows the concept of dividing a geometry into volume elements or cells in the two dimensional case. Fluid properties are stored in each cell center. The letters N, S, E, and W refers to north, east, west, and south relative to the point P.

w is assigned the properties of P. The diffusive term is discretized as

$$\int_V \boldsymbol{\nabla} \cdot \boldsymbol{\tau} \, dV = \int_A \boldsymbol{\tau} \cdot \mathbf{n} \, \mathbf{dA} = (\mathbf{A}\tau)_\mathbf{e} - (\mathbf{A}\tau)_\mathbf{w}, \tag{5.2}$$

where e and w refers to east and west, see Fig. 5.1. A detailed description of how the partial differential equation is turned into a finite difference equation by discretizaton can be found in the CFD user manual [7].

5.1.2 Geometry and grid creation

CFD-GEOM is used for creation of geometries and grids. For many preliminary investigations 2D-simulations can provide an idea of the result for the more time consuming 3D-simulations. However, simple 3D-geometries usually described in cylindrical coordinates, can be substituted by rotating a 2D-geometry around the z-axis. To allow this kind of solutions in CFD-ACE, it is necessary to choose the so-called *swirl* feature, which enables velocity components out of the plane.

The resolution of the geometry required to obtain a meaningful solution is dependent on the length scales of the system. If rapid changes are taking place as for example close to a sudden contraction, a finer grid is necessary. Therefore, it is an advantage to have an expectation of how the flow develops.

In GEOM, two types of grid are possible: structured and unstructured. In 2D, a structured surface grid consists of a surface with 4 edges, and the size of the cells can easily be varied.

5.1.3 Implemented models for blood flow

Rheology can be a very complex matter depending on the properties of the fluid in consideration, and how much it deviate from Newtonian behavior.

If we think about blood as a continuum, a generalized Newtonian model is a relatively easy way to implement non-Newtonian behavior.

In CFD-ACE+ it is possible to construct any generalized model through the so-called *usersub* routines, and as such there is no limit to the possibilities. However, models accounting for nonlinear viscoelastic properties and normal forces are not easily applied. Implementation of normal forces would require additional terms to the equation of motion.

In the CFD-ACE+ package we investigated three different constitutive equations *Power Law (Blood)*, *Walburn and Schneck*, and *Power Law*. The latter model was modified to recover the simple power law from the experimental section, Eq. (4.20).

5.1.4 Modelling Parameters

In the preprocessing it is necessary to specify various parameters that define the problem, and parameters to obtain convergence. We shall briefly introduce the used preprocessing conditions and relaxation parameters.

The no-slip boundary condition implies that the neighboring fluid particles have the same velocity as the boundary. If the boundary is a stationary wall the velocity of the fluid is zero. No-slip is also an example of the so-called Dirichlet boundary condition, since the boundary values are specified.

If the boundary values are unknown, we can apply a Neumann boundary condition, as for example symmetry. For a symmetry condition all the gradients of all variables normal to the boundary are zero.

A fixed pressure boundary is used to keep a constant pressure drop from inlet to outlet. When a constant pressure is specified, the pressure is independent of the mass flow.

For steady state simulations it can be difficult to obtain convergence if the specified boundary values are resulting in large velocities. Therefore, it can be necessary to start with an initial condition, which is expected to be close to the final result.

The relaxation parameters of the dependent variables can also be helpful in order to obtain convergence. If the relaxation parameter is small, the same goes for the step length in the iteration procedure. Therefore, when we have large variations in our variables, convergence can be obtained by specifying a small relaxation parameter.

To calculate fluid properties at the cell interfaces, the solver can apply different interpolation schemes. This choice can also have an effect on convergence, but in this project we have only used the upwind scheme. Compared to a central difference scheme, upwind is more appropriate for flow problems [27].

5.2 Testing of CFD-ACE+

In this section we will test the validity of the CFD-code by comparison with analytical obtained results. The chosen geometries are the concentric cylinder and the parallel disk rheometer.

5.2.1 Flow between concentric cylinders

The space between two concentric cylinders is called the annular space. We will now test the CFD-code by calculating the velocity and pressure profiles, and comparing the solutions with the analytical expression. The flow field is given by the equation of motion

$$\rho\frac{v_\theta^2}{r} = -\frac{dP}{dr} \tag{5.3a}$$

$$0 = -\frac{1}{r^2}\frac{d}{dr}(r^2\tau_{r\theta}) \tag{5.3b}$$

$$0 = -\frac{dP}{dz}, \tag{5.3c}$$

where we assume that $v_r = v_z = 0$. Eq. (5.3c) states that the pressure is constant in the z-direction. However, it would increase, if we considered gravity. If we assume that the liquid is Newtonian with the boundary conditions $v_\theta(R_1) = \omega R_1$, and $v_\theta(R_2) = 0$, the solution is

$$v_\theta(r) = r\left[\frac{\omega(R_1R_2)^2}{R_2^2 - R_1^2}\left(\frac{r^2 - R_1^2}{(R_1r)^2}\right) + \omega\right], \tag{5.4}$$

where ω is the angular velocity of the inner cylinder. R_1 and R_2 are the inner and outer radii, respectively. With the boundary condition $P(R_1) = 0$, the equation

$$P = \rho\left(\frac{R_1^2\omega}{R_1 - R_2}\right)^2\left(\frac{2R_2}{r} - \frac{B^2}{2r^2} + \ln(r)\right) \tag{5.5}$$

satisfies Eq. (5.3a). If we choose a relatively low value for the angular velocity, the assumptions are expected to be valid, and the analytical result should be comparable to the result produced by CFD-ACE+.

The chosen dimensions are $R_1 = 0.014\,\mathrm{m}$, $R_2 = 0.015\,\mathrm{m}$ and $\omega = 2\,\mathrm{s}^{-1}$. A definition of the variables can be seen in Fig. 5.2. As we have a no slip condition on the walls the velocity is $v_\theta(R_1) = 2\,\mathrm{s}^{-1} \times 0.014\,\mathrm{m} = 0.028\,\mathrm{ms}^{-1}$. The outer wall is stationary implying that the velocity at R_2 is zero.

Figure 5.3(a) shows a fine agreement between the velocity profiles for the two methods. To obtain a 3D-solution we utilized axisymmetry around the z-axis. In CFD-ACE+ it is possible to have a velocity component out of the plane, when the *Swirl* feature is chosen.

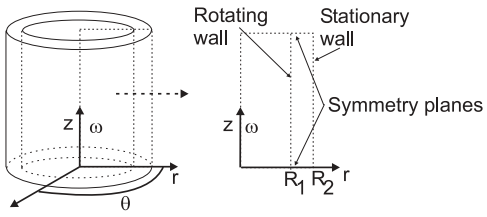

Figure 5.2: The figure shows two infinitely long concentric cylinders. The rectangular area surrounded by boundary conditions is the computational domain. A 3D-solution is obtained with axisymmetry around the z-axis.

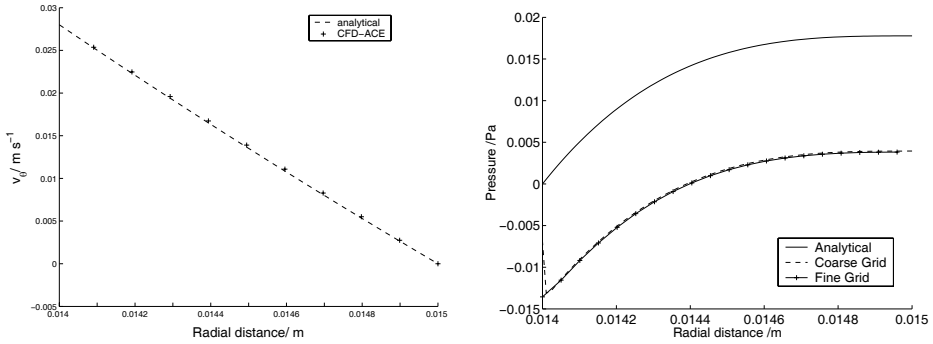

(a) (b)

Figure 5.3: Panel (a): A comparison between the velocity profiles in the annular space obtained by an analytical, and a numerical integration in CFD-ACE+. The two results coincide. The used parameters: $R_1 = 0.014\,\mathrm{m}$, $R_2 = 0.015\,\mathrm{m}$, $\omega = 2\,\mathrm{s}^{-1}$. The inner and outer wall have a no slip boundary condition. In the top and bottom symmetry was implemented, to simulate infinitely long cylinders. The profile was probed half way between the top and bottom. Furthermore, the variation in the axial direction was smaller than 0.5% of the maximum velocity. Panel (b): The fine grid size corresponds to the calculation shown in Fig. 5.3(a). The pressure profiles are not in agreement. The numerical solution is displaced with 0.013 Pa down the pressure axis, a significant fraction of the total analytical pressure. The shape of the curves are in agreement, but close to the R_1-boundary there is a nonphysical pressure drop. It is noticed that the grid size has no influence. This figure illustrates that it is necessary to be cautious, when dealing with CFD.

However, the pressure profile seen in Fig. 5.3(b), has a somewhat nonphysical drop at the R_1 boundary. It is seen that the solution is grid independent. The corresponding residuals are seen in Fig. 5.4, and they clearly show that all the variables, including the pressure, have converged. According to the user manual, residuals should drop five orders of magnitude for convergence. CFD-ACE+ is in this case reliable with respect to the velocity calculation, which it obtains from an integration of the equations of motion. The pressure is derived from the velocity data through the SIMPLEC algorithm, see the CFD user manual [7], but we have at this point no

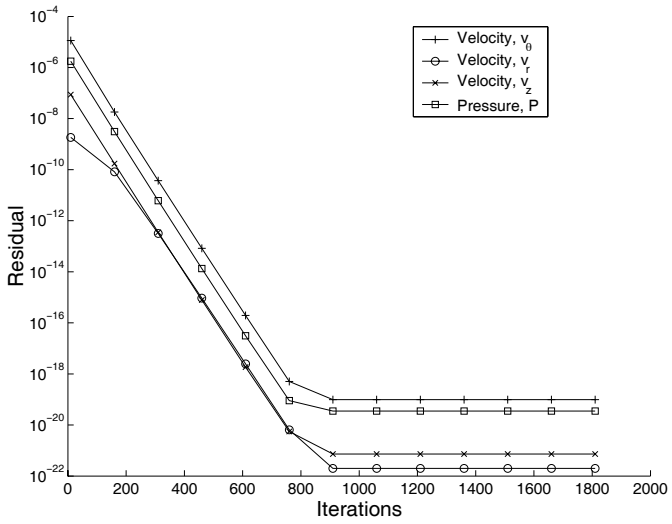

Figure 5.4: In the figure is shown the residuals from the simulations on the concentric cylinder geometry. All residuals have converged after 900 iterations. However, according to the manual a drop of five orders of magnitude should be sufficient [7].

explanation of the nonphysical pressure drop. We shall not go into details with the calculation of the pressure field, but the SIMPLEC algorithm is an iterative procedure to estimate the pressure, where the continuity equation links the equation of motion and the pressure field. The question of the pressure drop has been raised to the support group of CFD Research, but an answer has not appeared yet.

5.2.2 Flow in the parallel disk rheometer

We will now make a similar solution as we did in the former chapter. However, the parallel disk rheometer is a little more complex due to the dependencies on both r and z. At high angular velocities, secondary flow can be introduced and we shall therefore choose a low angular velocity $\omega = 2\,\mathrm{s}^{-1}$. We will use the analytical solution to verify the CFD-code. When we derived a relation between the torque and the shear rate it was assumed that v_θ increased linearly in the r direction. As a first guess, it could be imagined that an overfilled rheometer would affect this dependency. We can also use the analytical solution to investigate this issue.

The mathematical model for the rheometer is given by the θ-component of the equation of motion,

$$0 = \frac{\partial}{\partial r}\Big(\frac{1}{r}\frac{\partial}{\partial r}(rv_\theta)\Big) + \frac{\partial^2 v_\theta}{\partial z}, \tag{5.6}$$

and the boundary conditions sketched in Fig. 5.5. The flow is steady and the velocities in the radial and axial directions are neglected.

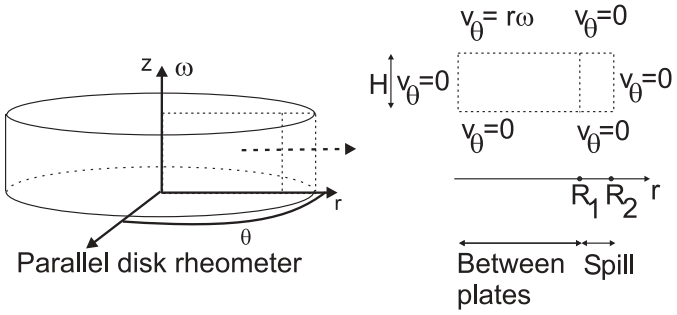

Figure 5.5: The figure shows the parallel disk rheometer. The dashed rectangle is the computational domain. A 3D-solution is obtained with axisymmetry around the z-axis. Spill refers to the blood due to overloading of the rheometer, see Fig.4.2. For $z = H$ it is noticed that the boundary condition in the r direction is discontinuous at R_1.

It is noticed that all the boundaries are homogenous, except the rotating plate. This implies that we have an unrealistic, discontinuous velocity profile at (R_1, H). However, the effect imposed by the boundary decreases with the distance from the wall, and at some z-value we expect the profile to be continuous at R_1.

We are going to solve a linear partial differential equation of second order with respect to the space variables r and z. For calculational purposes the problem is expressed in terms of the dimensionless variables

$$\tilde{v}_\theta = \frac{v_\theta}{u}, \quad \tilde{r} = \frac{r}{R_2} \quad \text{and} \quad \tilde{z} = \frac{z}{H}, \tag{5.7}$$

where u is the maximum velocity, $u = v_\theta(R_1, H)$. For notational convenience, the tildes will be dropped. Eq. (5.6) and the four required boundary conditions can now be written as

$$\begin{aligned} \frac{\partial^2 v_\theta}{\partial r^2} + \frac{1}{r}\frac{v_\theta}{r} - \frac{v_\theta}{r^2} + L^2\frac{\partial^2 v_\theta}{dz^2 0} &= 0, \\ v_\theta(0,z) = v_\theta(1,z) = v_\theta(r,0) &= 0, \\ v_\theta(r,1) &= f(r), \end{aligned} \tag{5.8}$$

where $L^2 = R_2^2 H^{-2}$. The profile f can be expressed by means of the Heaviside unit step function

$$f(r) = \omega r\, \Theta(d - r), \tag{5.9}$$

where d is the fraction between R_1 and R_2. The Heaviside step function Θ is zero for negative arguments and 1 for positive arguments. At first we obtain a partial solution by writing the velocity as a product function $v_\theta = R_n(r)Z_n(z)$

$$\frac{1}{R_n}\frac{d^2 R_n}{dr^2} + \frac{1}{R_n r}\frac{dR_n}{dr} - \frac{1}{r^2} = -L^2\frac{1}{Z_n}\frac{d^2 Z_n}{dz^2} = -k_n^2, \tag{5.10}$$

where k_n is a separation constant. The subscript n is used, as it turns out that we end up with an eigenvalue problem with an infinite number of solutions. Eq. (5.10) has to be constant as the independent variables are separated. We have two linear, second order, ordinary, differential equations

$$r^2\frac{d^2R_n}{dr^2} + r\frac{dR_n}{dr} + R_n(k_n^2r^2 - 1) = 0, \tag{5.11a}$$

$$\frac{d^2Z_n}{dz_n^2} - \left(\frac{k_n}{L}\right)^2 Z_n = 0. \tag{5.11b}$$

Eq. 5.11a is Bessel's differential equation with index 1. The second equation, Eq. (5.11b) has a solution of hyperbolic sines and cosines. However, the homogenous boundary condition in $z = 0$ implies that that the solution has to be a hyperbolic sine function, $Z(z) = C\sinh(k_nz)$.

As the operator in Eq. (5.11a) is self-adjoint, the eigenfunctions are orthogonal and forms a complete set [1]. The eigenfunctions are $R_n(r) = AJ_1(k_nr) + BY_1(k_nr)$, and have to satisfy the boundary conditions for fixed r-values. When r is approaching 0 the Y-function is unbounded, and it does not satisfy the homogenous boundary condition. The homogenous condition at $r = 1$ implies that k_n are the zeroes of J_1. Eq. (5.11b) is linear and we can therefore write the solution as a superposition of the products of R_n and Z_n

$$\begin{aligned} v_\theta(r,z) &= \sum_{n=1}^{\infty} A_nR_n(r)Z_n(z) \\ &= \sum_{n=1}^{\infty} A_n\sinh(k_nz)J_1(k_nr), \end{aligned} \tag{5.12}$$

where A_n is the expansion coefficients constant. This constant can be determined by the last boundary condition. At $z = 1$ the solution has to be $f(r)$, and we can therefore expand this profile in a Bessel series,

$$f(r) = \sum_{m=1}^{\infty} A_mJ_1(k_mr)\sinh\left(\frac{k_m}{L}\right). \tag{5.13}$$

Multiplying both sides with $rJ_1(k_nr)$, and integrating over the entire range gives

$$\int_0^1 f(r)rJ_1(k_nr)dr = A_n\sinh\left(\frac{k_n}{L}\right)J_2^2(k_n), \tag{5.14}$$

by use of the orthogonality of the Bessel function. Substituting Eq. (5.9) into Eq. (5.14) and isolating the constant yields

$$A_n = \frac{\int_0^d r^2J_1(k_nr)dr}{dJ_2^2(k_n)\sinh(\frac{k_n}{L})}. \tag{5.15}$$

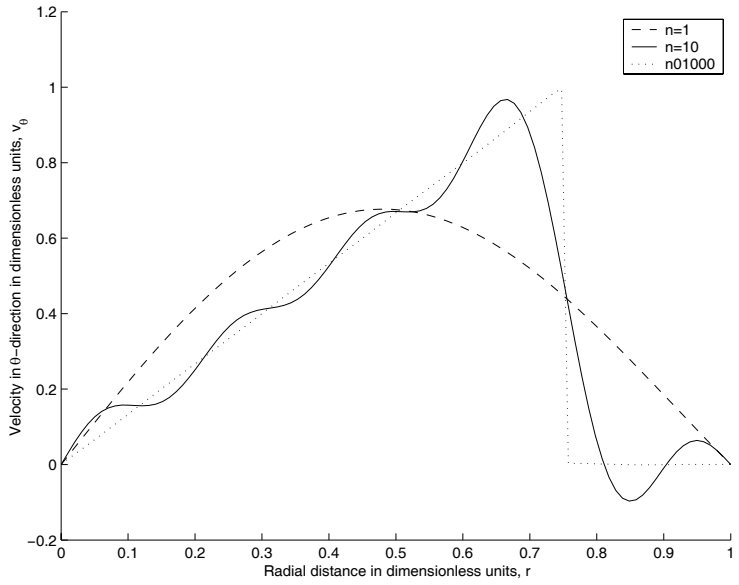

(a)

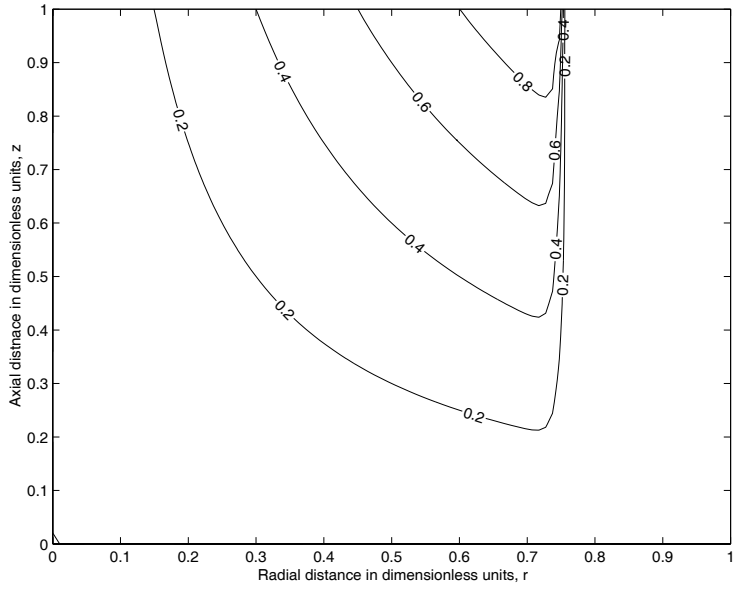

(b)

Figure 5.6: Analytical solution, Eq. (5.12), to the parallel disk rheometer in Fig. 5.5. Parameters: $z = 1$, $d = 0.75$ and $L = 40$. Panel (a): The figure shows how the solution converges as the number of terms n increases from 1 through 10 to 1000. For $n = 1000$ we obtain the profile given in Eq. (5.9). Panel (b): The figure shows a contour plot for the velocities. It is noticed that the velocity is very small for $r > 0.75$, which is in the spill region.

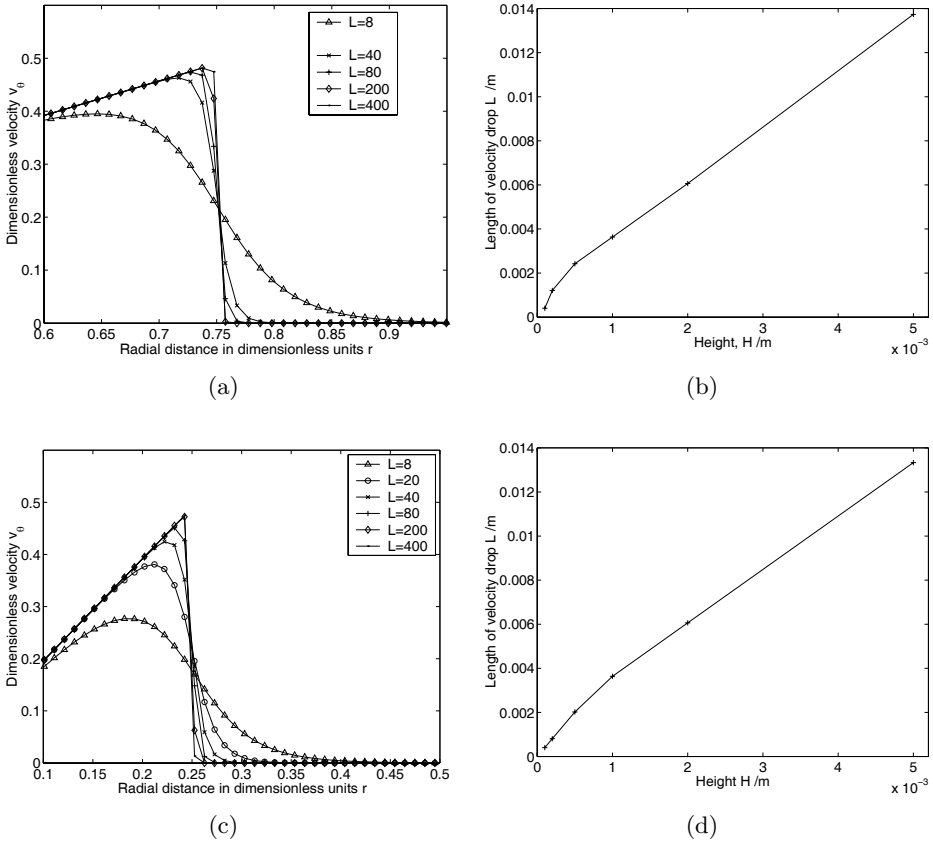

Figure 5.7: Analytical solution for the parallel disk rheometer seen in Fig. 5.5 for $z = 0.5$. With this value of z we see the profile in the middle of the two plates. For panel (a) and (b) we set $L = R_2/H = 40$ and $d = R_1/R_2 = 0.75$. Panel (a): velocity as a function of r. Technically, the drop length is defined as the distance between the maximum velocity and the first coming velocity below 0.002. Panel (b): Data points for the increasing drop length as a function of the height H. These data are extracted from the figure in (a). For panel (c) and (d) the parameters $L = 40$ and $d = 0.25$. Panel (c): the velocity as a function of r. Panel (d): drop length as a function of H. The drop length is short even at small values of d, i.e. when the distance to the end wall is increased. The data are extracted from figure (c).

Eq. (5.12) and (5.15) solves Eq. (5.8). Figure 5.6 and 5.7 are produced with the matlab script file `vel.m` seen in Appendix B. Figure 5.6(a) shows the convergence as the number of terms in the sum increases, Eq. (5.12). It is noticed that $n = 1000$ is a very good approximation to the profile at $z = 1$.

To investigate the effect of an overfilled rheometer, we can look at the velocity profile in the spill. Figure 5.7 shows how the drop length increases with the height of the rheometer. As we were operating at gap sizes or

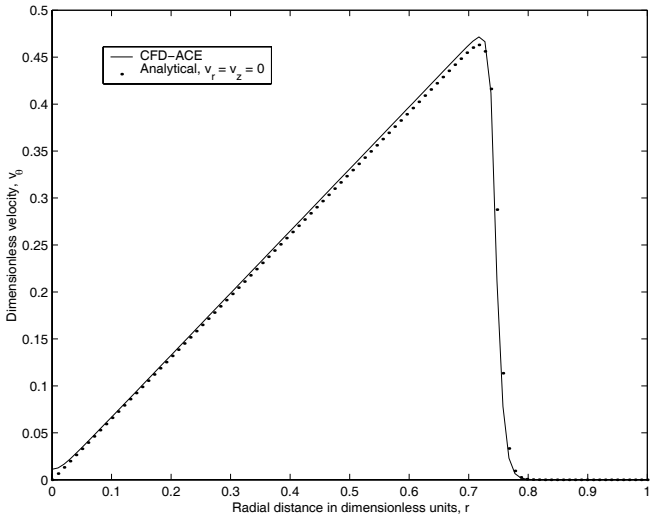

Figure 5.8: A comparison of the analytical and numerical result for the parallel disk rheometer seen in Fig. 5.5, $L = R_2/H = 40$ and $d = R_1/R_2 = 0.75$. The curves are coinciding.

heights smaller than $1000\,\mu$m, that is to say $L > 40$, the drop lengths are smaller than 4 mm. So, depending on the viscosity it does have a small effect on the required torque. It is noticed that if the gap size is small the assumption that v_θ is linearly dependent on r is acceptable. In the analytical solution we applied a no slip condition on the outer wall. However, Fig. 5.7(b) and 5.7(d) show that the distance from the boundary only has a minor effect on the drop length.

Figure 5.8 shows a comparison of the numerical and analytical solutions, and the curves are seen to coincide. In conclusion, the CFD-code has proven valid, and the assumption for v_θ seems acceptable. We could perform a more rigorous investigation of how much the overfilling of the rheometer influences the torque measurements. It would also be possible to increase the angular velocity, and study when the secondary flow becomes a significant part of the θ-directed velocity. On the other hand, it turned out that there were other problems with the rheometer, and we shall therefore not go into further details on this matter.

5.3 Investigating blood models

We shall now investigate the two default blood models in the CFD program and compare them with simple power law models. We shall not use the default models for an extensive number of simulations, but since many different constitutive equations have been suggested, we shall take a closer look on their similarities and differences. The default Power Law(Blood)[12] is

Table 5.1: Default parameters in CFD-ACE+ blood constitutive equations. Parameters in the Power Law(Blood) and Walburn and Schneck are entered in cgs units, but the output from the CFD solver is in SI-units, see Appendix C.

Parameter Power Law Blood	Value in cgs units	Parameter Walburn and Schneck	Value in cgs units
μ_∞	0.035	a_1	0.00797
$\Delta\mu$	0.25	a_2	0.0608
N_∞	1.0	a_3	377.7515
ΔN	0.45	a_4	0.00499
a	50.0	.	.
b	3.0	.	.
b	50.0	.	.
d	4.0	.	.

given by

$$\tau = \lambda\, \dot{\gamma}^{(n-1)}\, \dot{\gamma}, \tag{5.16}$$

where

$$\lambda(\dot{\gamma}) = \mu_\infty + \Delta\mu \exp\left[-\left(1 + \frac{|\dot{\gamma}|}{a}\right) \exp\left(-\frac{b}{|\dot{\gamma}|}\right)\right], \tag{5.17}$$

and

$$n(\dot{\gamma}) = n_\infty - \Delta n \exp\left[-\left(1 + \frac{|\dot{\gamma}|}{c}\right) \exp\left(-\frac{bd}{|\dot{\gamma}|}\right)\right], \tag{5.18}$$

with the default settings as in Table 5.1.

Table 5.2: Parameters for simple power law constitutive equations.

Parameter	Our Power Law	Chang's Power Law [5]
k	0.057	0.00733
n	0.623	0.932

The Walburn and Schneck model is given by

$$\tau = a_1 \exp\left(a_2 H + \frac{a_3}{H^2}\dot{\gamma}^{1-a_3 H}\right)\dot{\gamma}, \tag{5.19}$$

where the default settings are given in Table 5.1. The simple power law is

$$\tau = k\dot{\gamma}^n, \tag{5.20}$$

where measured values of k and n are listed in Table 5.2. In all studies on blood rheology shear thinning is restricted to regions at relatively low shear

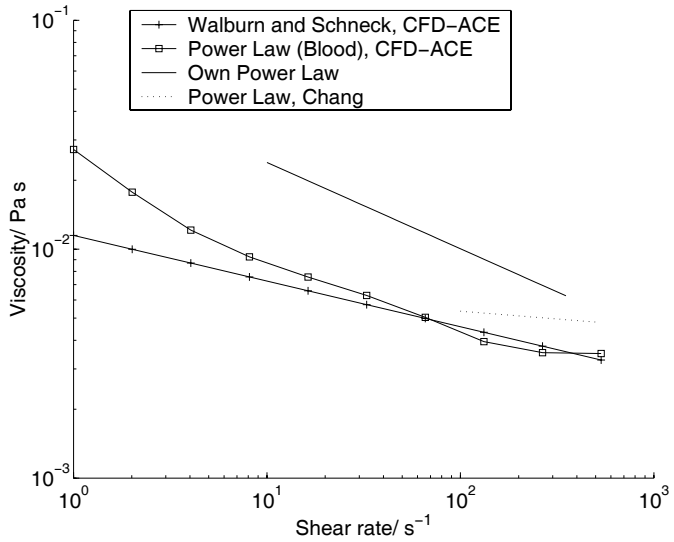

Figure 5.9: The figure shows the viscosity for different blood constitutive equations, which have been derived from different blood samples. In the preprocessor it is not possible to specify valid ranges of the non-Newtonian viscosity. Hence, the viscosity in the simple power law model keeps decreasing. For measurements performed in this project the viscosity was constant for shear rates above $300\,\mathrm{s}^{-1}$. The plotted Walburn and Schneck and Power Law (Blood) model are the default models in the CFD-ACE+ package.

rates, which means there should be a transition, where the constitutive equations switches from a power law to a Newtonian. Figure 5.9 shows the non-Newtonian viscosity for different constitutive equations. It is noticed that the Chang group measured the viscosity in an interval, where we according to our experimental results would start to expect linearity. Chang's power law is the least non-Newtonian, which probably is due to the measurement technique. The viscosity was measured in an oscillating tube, and the viscoelastic shearing viscosity η_V appear less non-Newtonian compared to the shearing viscosity η_s, see the discussion in chapter 4. Furthermore, the used blood was defibrinated sheep blood. Fibrinogen is important for rouleaux formation, and it could therefore be expected that the blood only had a small tendency to aggregate. Walburn and Schnecks model is applicable until $110\,\mathrm{s}^{-1}$.

Experimental work from this project shows that the viscosity reaches a constant level at high shear rates, $300\,\mathrm{s}^{-1}$. This problem is not addressed in the CFD-code for the simple power law model. We can get an estimate of the consequences if we look at Hagen-Poiseuilles equation for Newtonian fluids in tubes

$$\dot{Q} = \frac{\pi R^4}{8\mu}\frac{dP}{dz}, \tag{5.21}$$

where $\dot{Q}$ is the flow rate, μ the Newtonian viscosity and dP/dz the axial pressure gradient. At high shear rates the viscosity used in the calculations will be smaller than the experimental viscosity. This means, for a constant flow rate, that the pressure gradient will be underestimated. However, Chang and coworkers showed in an experiment for a shear flow in a straight microchannel that CFD-ACE+ simulations with a simple power law yielded pressure drops in agreement with the experiments [5].

The more complicated model Power Law(Blood), has the feature of recovering a Newtonian viscosity at high shear rates. However, it is derived from measurements on normal blood, which means that the hematocrit varies within the range of normal hematocrits, i.e., the hematocrit is not a constitutive parameter.

In the Walburn and Schneck model we can specify the hematocrit, but it has the disadvantage that the viscosity keeps decreasing, as a function of the shear rate. The model is derived for human whole blood at 37 °C. However, we shall in this project not be concerned with the temperature effects.

5.4 Flow in microchannels

As mentioned in the last section, when we perform the simulations, the simple power law is considered valid for infinitely large shear rates, which contradicts the experimental results. In the experiments for this project the power law ceased to be valid after $140\,\mathrm{s}^{-1}$, and the viscosity reached a constant plateau. In the paper by Chang et al. [5] the apparent viscosity was measured and fitted with a power law up till $400\,\mathrm{s}^{-1}$. When they applied the power law in simulations, the results were in a fine agreement with experimental work, if the geometry was a straight channel. This could look like a coincidence as the calculated shear rates are far beyond $400\,\mathrm{s}^{-1}$.

We will in this section apply our power law for simulations in a microtube, and show the principles of grid analysis. Furthermore, Chang's results in a microchannel will be compared with a re-simulation in a microtube with the same cross-sectional area. This is done to obtain information of the velocity and shear rate profiles. Figure 5.10 shows two different discretizations of the same grid. As seen, the cells are clustered in order to resolve the larger change in velocity close to the wall. The flow field does not change in the axial direction, and only a few grid points are necessary. High aspect ratios may lead to difficulties in convergence. However, in this case we had a fine convergence. The grid dependence analysis shows that the relative error between the coarse and fine grid is below 35%, Fig. 5.11. Furthermore, the fine grid is coinciding with the analytical solution, and we shall therefore take the fine grid as independent of discretization. In geometries of higher complexity, a more thorough analysis would be necessary. According to the *Best Practise Guidelines* by Casey and Wintergerste [4], a good grid analysis

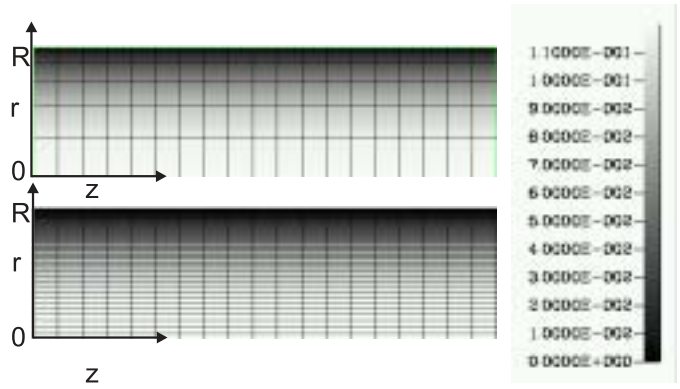

Figure 5.10: The figure shows two different grids for the cross section of a microtube, where the radius is 35 μm and the length is 12 mm. The upper figure shows the coarse discretization where the cells are clustered near the walls to account for the larger variation in the velocity. For the simulations axisymmetry was used around the z-axis. The domain is divided into 20×20 cells. The lower figure shows the finer discretization with 20×40 cells. The colorbar shows the velocity in the axial direction.

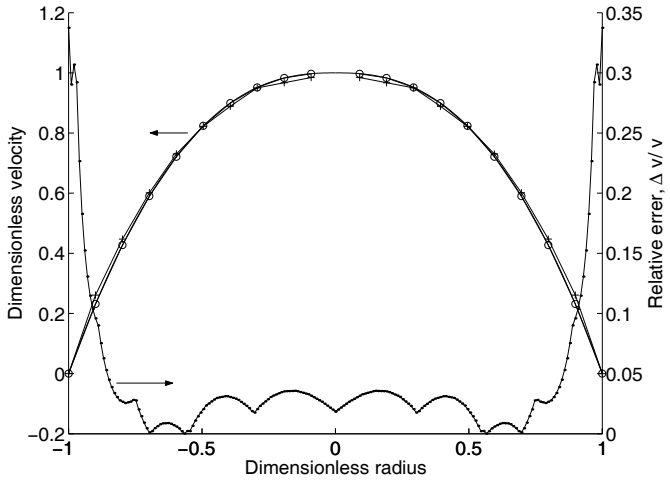

Figure 5.11: The figure shows the grid dependency of the velocity profiles in a microtube with a radius of 35 μm. Legends: ($\circ$) fine grid, (+) coarse grid, (- solid line) analytical solution. When a solution becomes independent of discretization, the geometry is properly resolved. It is noticed that the relative error between the coarse and fine grid is larger in areas with a large change in the velocity, i.e., near the wall. In this case, we consider the fine grid acceptable and shall use it for further simulations.

include at least three different resolutions for each coordinate axis. Nevertheless, as we can compare with the analytical solution, we have no reason to doubt that the fine grid is independent of discretization.

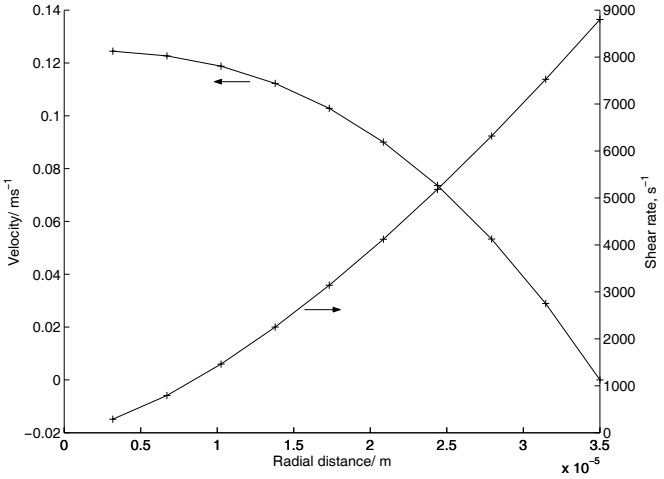

(a)

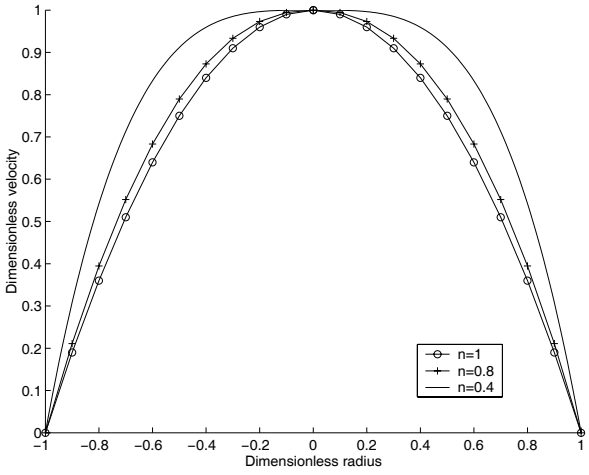

(b)

Figure 5.12: Panel(a) shows the velocity and shear rate profiles calculated on the fine grid in Fig. 5.10 using the simple power law, Eq. (4.20). The pressure drop is 16×10^3 Pa. With a density at $1003\,\mathrm{kgm}^{-3}$ the volumetric flow rate is $2.7 \times 10^{-10}\,\mathrm{m}^3\mathrm{s}^{-1}$. From fitting of the simple power law, it is known that our power law equation is valid until $140\,\mathrm{s}^{-1}$. This is not taken into account in the simulations. Panel (b) shows the effect of non-Newtonianness in the simple power law. When the power law index decreases, the profile tends to flatten. This means that we have very high shear rates close to the wall, and small shear rates in the center region.

Figure 5.12(a) shows the velocity and shear rate profile calculated on the fine grid. It is noticed that a short distance from the center we exceed the experimental shear rate range, which suggest that more than one constitutive equation is required to model blood flow in microchannels.

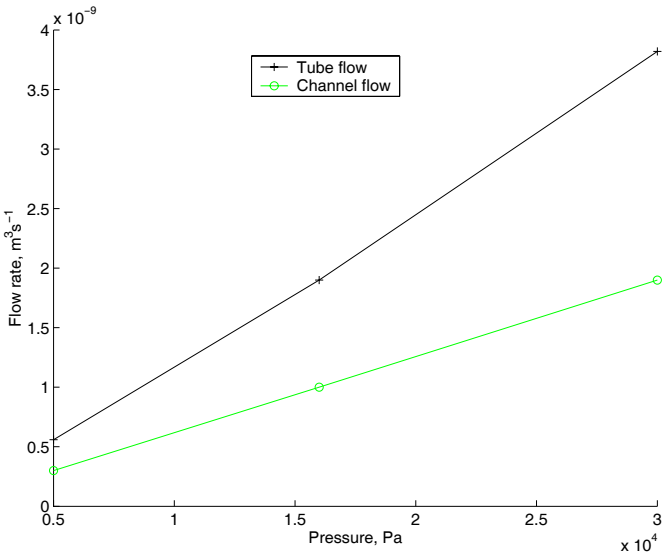

Figure 5.13: The figure shows the volume flow rate for a microchannel with dimensions $200\,\mu\text{m} \times 60\,\mu\text{m} \times 12\,\text{mm}$ and a tube with a radius of $62\,\mu\text{m}$ and 12 mm in length. The cross sectional areas are $12000\,\mu\text{m}^2$ and $12076\,\mu\text{m}^2$, respectively. The simulations on the channel are taken from Chang et al.[5], and the simulations on the tube are carried out for the present project. The results on both the channel and the tube are obtained with the Power Law from the research of Chang and coworkers.

When the non-Newtonianness for a shear thinning liquid is increasing, i.e, the index is smaller than one and approaches zero, the velocity profiles become more blunted, see Fig. 5.12(b). In Fig. 3.8 it was seen that the velocity profile for blood is blunted at low shear rates. However, it approaches the parabolic profile at high flow rates. Hence, the simple power law is not adequate to describe the velocity profile. We shall now take a closer look on the issue of valid shear rate ranges for the constitutive equation. Simulations in tubes are less time consuming than in a channel geometry, since in tubes we can use the advantage of axisymmetry. Therefore, we will make the following considerations for a tube flow.

Figure 5.13 shows a comparison between a microchannel and a microtube simulation with Chang's power law. As expected for a given pressure, the flow rate is largest in the tube due to the smaller surface to volume ratio, and the slightly larger cross sectional area. It was also pointed out by Chang et al. that the flow rate is almost linearly dependent on the pressure, as the power law index is close to one. In the paper [5] it is also noted that corresponding flow and pressure data are in a very fine agreement between simulations and experiments for simple geometries, but there is somehow a discrepancy when the geometries becomes more complex, i.e, a 90° bend. For this geometry Chang et al. show that the simulated pressures

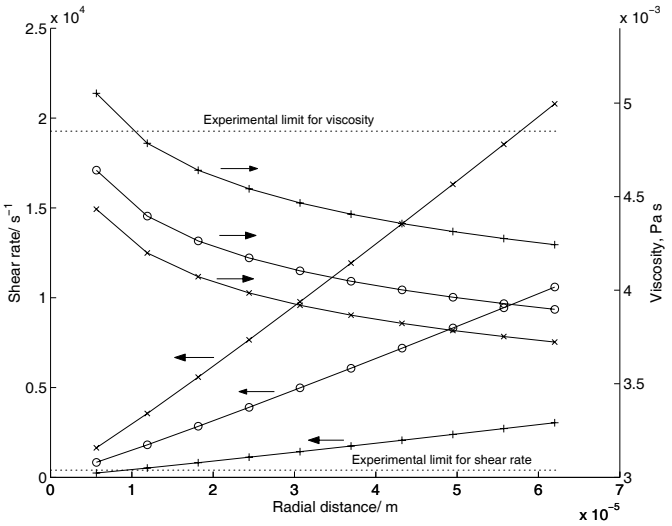

Figure 5.14: The figure shows the shear rate and viscosity in a tube with 62 μm in radius for different pressures. The simulations are performed for this project with the use of Chang's [5] Power Law, Table 5.2. The markers indicate: (+) $\Delta P = 5000\,\mathrm{Pa}$, ($\circ$) $\Delta P = 16000\,\mathrm{Pa}$, and ($\times$) $\Delta P = 30000\,\mathrm{Pa}$. The arrows indicate on what axis the values should be read. The power law is obtained from data in the shear rate range between 50 and $400\,\mathrm{s}^{-1}$. On this basis we have pictured the experimental limits as dotted lines. It is noticed that we exceed the experimental limit about 10 microns from the center. The upper experimental limit for the shear rate is $400\,\mathrm{s}^{-1}$ and the corresponding viscosity is $4.85 \times 10^{-3}\,\mathrm{Pa\,s}$ [5].

are consistently lower than the experimentally obtained. Using the power law implies that the viscosity will keep decreasing as we go to higher shear rates, Fig. 5.14. It is known that the viscosity actually reaches a constant level at high shear rates, and the simple power law should therefore fail at high shear rates. However, the equation predicts the relation between pressure and volume flow rates in a straight channel.

We can also interpret the problem from a more physical point of view, and consider blood as a fluid consisting of plasma with suspended particles. In the theory section it was seen that the cellular components of blood were migrating away from the wall, and a region of 10 μm from the wall could be almost free of cells, Fig. 3.9. Therefore, at the high shear rates near the wall we can not allow viscosities below 1.2 Pa s, the viscosity of plasma. To fulfill this requirement for Chang's equation, we can not go beyond $340 \times 10^9\,\mathrm{s}^{-1}$. After all, these shear rates should not become actual.

The shear stresses in a microfluidic system is valuable information for the designing process. When red blood cells are exposed to high shear rates they may lyse, which is an unwanted process for some applications. According to Chang et al. [5], hemolysis will occur at shear rates above $30 \times 10^3\,\mathrm{s}^{-1}$.

To sum up on the foregoing analysis, a disadvantage of the simple power

law model is that it does not reduce to a Newtonian model at high shear rates. Even at high shear rates the velocity profile will be blunted.

The Power Law(Blood) model is applicable even at high shear rates. The power law index n starts of at values smaller than one at low shear rates, shear thinning, and approaches one at higher shear rates, Eq. 5.18. The viscosity index λ is also approaching a constant value at high shear rates, Eq. 5.17. In other words, the model recovers the Newtonian model at high shear rates. Its implementation in CFD-ACE+ will be tested in the following section 5.5.

Fung [10] suggests another way to obtain a velocity profile that is blunted at small shear rates and gets progressively more Newtonian as the flow rate is increased. In a tube or channel the shear rate approaches zero at the center. For blood samples containing fibrinogen it is possible to observe yield stresses, and the idea is now to divide the tube into different regions of shear rate. Near the wall we would apply a Newtonian model, and in the middle of the tube we could choose the Casson model. According to the Casson model, blood behaves like a solid at small shear rates, and we would therefore have a plug flow in the center of the tube. As the flow rate is increased, the solid domain in the middle will decrease, and the profile will get less blunted.

By this last approach we are starting to think of blood as an inhomogeneous fluid, consisting of plasma near the wall. As the flow rate is increased the cells are squashed together in the center, due to the effect from the walls. A more extensive outline of a cell layering theory for blood in a shear flow is given by Thurston [24].

This model, where the tube is divided into shear rate regions, are implementable in CFD-ACE+, through the so-called usersub files. However, it is not covered in this project.

5.5 Simulations with default Power Law(Blood) in simple microchannel

The strength in numerical simulations in CFD-ACE+ is the possibility of simulating a flow in fairly complex geometries. Compared to the tube, we shall now take a step towards a geometry slightly more complex. In the preceding section it was seen that the default Power Law(Blood) model reduced to a Newtonian liquid at high shear rates. We will now test the CFD-package and see if this feature is obtained in the simulations. This is done by comparing velocity profiles at different flowrates.

Additionally, Chang and colleagues [5] did not take the Fahraeus effect into account, and we could therefore expect that the viscosity in their simulations are overestimated. However, they did probably also use the power law beyond the experimental limit, which means the viscosity is underes-

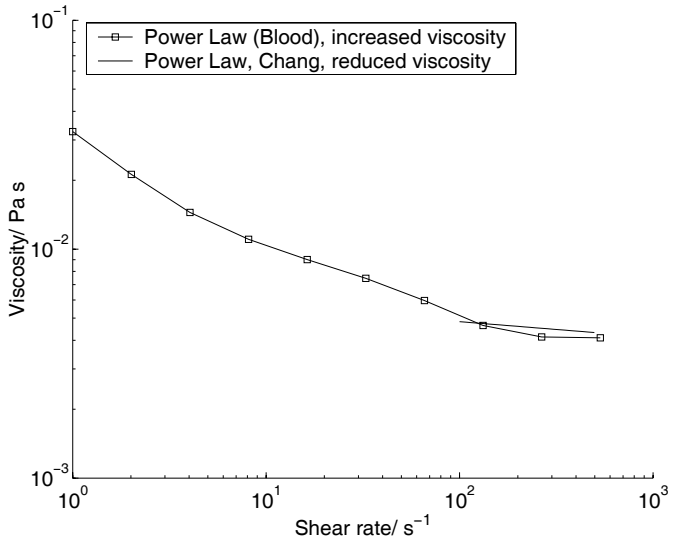

Figure 5.15: The figure shows Chang's equation after it has been corrected for the Fahreaus effect according to Fig. 3.11(a). The default CFD-ACE+ power law blood has been changed in order to fit the other curve. The parameters were set as seen in 5.1 with the exception $\mu_{inf} = 0.41$ and $\Delta\mu = 0.3$.

timated. In the case of the simple channel there were a fine agreement between simulations and experiments. Therefore, one of the intentions of the following simulations was to investigate, if the two mentioned effects could cancel each other.

A tube with a radius of 62 μm corresponds to the cross sectional area for the channel used by Chang. They used defibrinated blood from a sheep with a hematocrit at 41%. If we assume that Fig. 3.11(a) is a good approximation to sheep blood we would have a 10 % reduction in the hematocrit. Figure 5.15 shows Chang's measurements after the reduction. In the figure is also shown the power law blood model, where the default parameters have been changed in order to make a better fit. Figure 5.16 shows the simple rectangular channel, with the lineprobe where I extracted velocity profiles for different flow rates.

Figure 5.17 shows that we can produce the expected blunted velocity profile with the power law blood model. In other words the model seems to be implemented correctly in the CFD-code. However, within the time limits of this project, it was not investigated thoroughly to what extent the two mentioned effects will cancel each other.

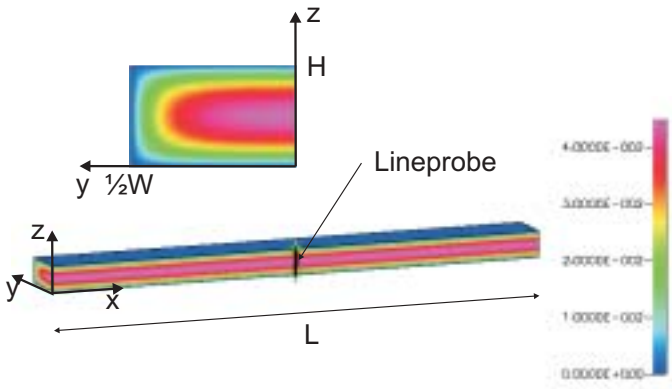

Figure 5.16: The figure shows a simple channel with cross sectional area $200 \times 60\,\mu\text{m}^2$ and length 12 mm. The colorbar shows the magnitude of the velocity in the x-direction for a pressure drop at 5000 Pa. The lineprobe is used to extract velocity profiles in CFD-VIEW. Because of the rectangular shape and small dimensions, the velocity profiles will be distorted from the parabolic shape.

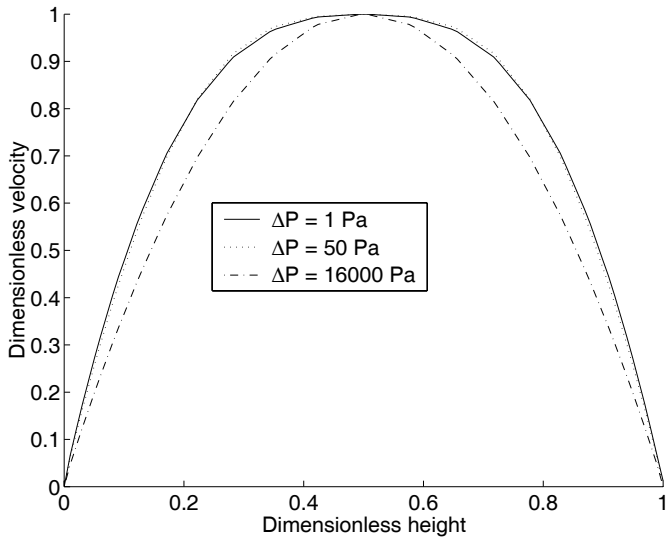

Figure 5.17: Velocity profiles for the lineprobe shown in Fig. 5.16. The profiles are obtained by simulations with the power law (Blood) model for different pressures. The figure shows that the model works as expected, as the profiles are blunted at low flow rates, i.e., small pressure gradients.

Chapter 6

Discussion and Conclusion

In this study we attempted to find by experiments a relation in a blood constitutive equation explaining the dependency on the dimensions of a microchannel. However, due to uncertainties of a skewed rotating disk, it was not possible to investigate the problem using this geometry.

In other studies of blood flow in microchannels the viscosity is obtained in an oscillating tube [5]. It was therefore the intention to establish a relation between the viscoelastic properties of blood and the steady state shearing viscosity. This was done by means of Thurstons theory of a degradation formula, which modelled the break down of aggregates or rouleaux.

Since an oscillating disk, in contrast to a rotating, is measuring over the same point, we hoped that we could decrease the influence of the disk's skewness. This hypothesis was, however, never tested due to other instrument problems.

Another output of oscillating measurements is the information about time relaxation parameters for blood in an almost stationary state, but their relevance to modelling of blood flow have not been investigated.

From the shearing viscosity measurements, we obtained a constitutive equation described by a power law, with a shear thinning power law index. It is believed that the equation is valid, as the same result was obtained in two different geometries. Still, the equation only expresses the properties of blood at large gap sizes.

Chang et al. [5] have obtained some very fine results on simulations of blood flow in simple microfabricated geometries. Even though their results seems to estimate the quantitative relation between flow rate and pressure drop, there is still some questions that should be addressed. Why does the prediction break down for complex geometries, and is the simple power law applicable at high shear rates? For blood flow, measured velocity profiles are blunted at low flow rates, whereas it becomes more parabolic at higher shear rates. This is a behavior, which is not contained in the power law. Fung [10] suggest that a Newtonian model should be applied at high shear

rates near the wall, and a non-Newtonian model at lower shear rates. This was not tried in the simulations.

In the CFD-ACE+ package the power law(Blood) model is non-Newtonian at small shear rates, and it reduces to Newtonian model, as the shear rate is increased. However, the simulations with the model did not show the expected blunted velocity profile. Meaning, there is s problem with the implementation.

In more complex geometries normal forces may affect the flow and flow resistance. In the theory section we discussed the CEF-equation, which models normal forces, however the problem was not addressed in this project but it might be a topic for further investigations on blood blow.

From the review on blood flow, we also learned that blood can not be considered as a continuum at very small length scales. Due to the high shear rates, cells migrate away from the wall towards the center. In this way plasma lubricates the flow of the cellular content. As plasma is a Newtonian liquid, this observation speaks for Fung's solution that the liquid near the wall should be expressed with a shear-independent viscosity.

Furthermore, for future and better results of rheological experiments on blood, it will require that we can measure the hematocrit. This is done in a microhematocrit centrifuge . The hematocrit is a very important rheological parameter. At hematocrits below 8% blood behaves Newtonian, and, in general, the viscosity is an increasing function of the hematocrit. Also, to address the Fahraeus effect it is necessary to measure hematocrits, and have a good laboratory practice.

Chapter 7

Outlook and Ideas

Microfluidic systems is a new field to me, and after 8 months of study it is difficult not to be overwhelmed by the possibilities. The ultimate goal of a microfluidic system is a fully integrated low cost disposable chip, which is capable of processing and analyzing a body fluid in order to give a full diagnosis. Microtechnology is a field where a range of new opportunities have been discovered, and it is also a field where it is allowed to utter visions and ambitious ideas. Therefore, it is sometimes difficult to remember what is actually possible at present time and what is the ultimate goal. In that perspective, I will take the liberty of expressing some of the thoughts that emerged during this project.

In this section I will present ideas for two kinds of microfluidic systems that both processes blood. The first example is a microreactor used for organic synthesis using enzymes as a catalytic agent. The second is a micro rheometer used to continuously study the rigidity of individual cells, as a chemical is added. In this way it would be possible to screen for the effect of a large variety of drugs.

Microreactor

In general microreactors have the advantage of large heat and mass transport due to the increased surface to volume ratio [13]. They use smaller amounts of reactants, and are more efficient than conventional macroscopic reactors.

Many drugs are organic molecules resembling substrates, which are naturally found in the body. They deviate, however, slightly from the natural substrates as they inhibit an enzyme or receptor instead of starting a cascade of biochemical reactions, which control the physiological state.

This device, which could be referred to as a microbioreactor, should be able of converting a plasma protein into a peptide that regulates a physiological mechanism. A bioreactor can just be thought of as a shallow microchannel, where enzymes are immobilized on the walls.

To illustrate the idea of this reactor I have picked out an example as advised by Lars Ole Simonsen [20] from the University of Copenhagen. However, I will emphasize that this is just a suggestion, but it would be possible to develop more appropriate examples in cooperation with people having a larger insight into pharmacology.

Renin is a proteolytic enzyme released from specific cells in the kidney and acting on a plasma protein angiotensinogen. A reaction scheme could be expressed as

$$\begin{aligned} \text{Angiotensinogen} &\xrightarrow{\text{Renin}} \text{Angiotensin I} \\ \text{Angiotensin I} &\xrightarrow{\text{ACE}} \text{Angiotensin II} \\ \text{Angiotensin II} &\xrightarrow{\text{Chemical Modification}} \text{ARA}. \end{aligned}$$

Angiotensinogen discard the N-terminal decapeptide angiotensin I, whereafter an angiotensin converting enzyme (ACE) converts angiotensin I into the active octapeptide Angiotensin II. In the body, Angiotensin II binds to a receptor (AR) and stimulates an increase of the blood volume, and blood pressure. The effects of Angiotensin II is a complex matter, however high levels of Angiotensin II over longer periods is damaging for the health. The Angiotensin II receptor antagonist (ARA) binds to the Angiotensin II receptor, however, it does not stimulate to an increase in blood volume. A known receptor antagonist is for example Losartan, which is distributed on the Danish market.

A microfluidic system for this purpose would consist of a filter, and three reactors. First a filter to remove the blood cells, whereafter the plasma enters the reactors with immobilized enzymes and a chemical reactor corresponding to the steps in the scheme.

This kind of process would not be convenient in a conventional reactor, as the protein substrate is a reactant of limited resource. In the microreactor, high surface to volume ratio ensures that the distance between immobilized enzymes on the reactor wall and the substrate is short, which results in high efficiency. Furthermore, as enzymatic reactions are very specific, it would be possible to eliminate side reactions. Computational fluid dynamics would be a very powerful tool in designing such a reactor, and CFD-ACE+ has already a build-in biochemical module to handle enzymatic reactions.

Device for measuring blood cell deformability

The second example is inspired by Poul Bennekou [2], and his experience with sickled red cells. People suffering from sickle cell anemia, are very vulnerable to changes in blood viscosity, which is determined by the rigidity of the red cells. Many drugs affects the red cell membrane and can therefore have a critical consequence for sickle cell anemia patients. Therefore, it would be convenient with a small device for continuous monitoring of the rigidity of the red cells as a drug is added. This instrument could be thought

off as a scaled down rotational rheometer, where a small rotational disk relates the strain of a blood cell with an applied force. Viscosity measurements of blood in conventional rheometers have been used for clinical purposes for a while [15]. However, micromachined devices for measurements on the deformability of individual cells are under development [26].

It will take a lot of effort to turn these ideas into functional products, and it was after all not the intention of this project. These ideas should serve as an illustration of some of the possible applications of microfluidic systems manipulating blood, and the importance of interdisciplinary research on this particular field.

Bibliography

[1] Arfken, F. B. and H. J. Weber: *Mathematical Methods for Physicists*. Harcourt/Academic Press 2001.

[2] Bennekou, Poul Assoc. Prof, Lic. tech., the August Krogh Institute, Copenhagen University: private correspondence.

[3] Bird, R. Byron , Robert D. Armstrong and Ole Hassager: *Dynamics of Polymeric Liquids*. John Wiley & Sons (1987).

[4] Casey, Michael and Torsten Wintergerste *Quality and Trust in Industrial CFD* Fluid Dynamics Laboratory Sulzer Innotec, version 1.0 January 2000.

[5] Chang, Wesley, David Trebotich, Luke P. Lee and Dorian Liepmann: *Blood Flow in Simple Microchannels*. First Annual International IEEE-EMBS Special Topic Conference on Microtechnologies in Medicine and Biology October 12-14, 2000, Lyon, France.

[6] Christensen, Klaus, Bio-Array, MIC, Lyngby: private correspondence.

[7] CFD Research Corporation: *CFD-ACE(U)* User Manual Version 6.6.

[8] CFD Research Corporation, 215 Wynn Drive Huntsville, AL 35805, USA

[9] Evans, D.F. and H. Wennerstrom: *The Colloidal Domain, Where Physics, Chemistry, Biology, and Technology Meet* 1994 VCH Publishers, Inc.

[10] Fung, Y.C.: *Biomechanics, Mechanical Properties of Living Tissues*. Springer Verlag, Second Printing, 1984.

[11] Fung, Y.C.: *A First Course in Continuum Mechanics*. Prentice Hall, Englewood Cliffs, New Jersey 07632 third edition (1994).

[12] Giridharan, M. G., S. Krishnamoorthy and Anantha Krishnan: *Computational Simulation of Microfluidics, Electrokinetics and Particle Transport in Biological MEMS Devices*. CFD Research Corporation 215 Wynn Drive Huntsville, AL35805.

[13] Jensen, Klavs F.: *Microreaction engineering - is small better?* Chemical Engineering Science 56 (2001) 293-303.

[14] Liepsch, D., G. Thurston, M. Lee *Studies of Fluids Simulating Blood-Like Rheological Properties and Applications in Models of Arterial Branches.* Biorheology, 28: 39-52, 1991.

[15] G.D.O. Lowe and J.C. Barbenel: *Plasma and Blood Viscosity.* Clinical Blood Rheology, vol 1, ed. by G.D.O. Lowe, Boca Ration, Florida, 11-44, (1988).

[16] Pedersen, Fl. Bo: *Hydraulik for bygningsingenioerer.* Den private Ingenioerfond Danmarks tekniske Hoejskole, Lyngby 1988.

[17] Rigshospitalet, H:S Blodbank, Blegdamsvej 9 2100 Copenhagen East, Denmark

[18] Probstein, Ronald F.: *Physicochemical Hydrodynamics, An Introduction.* John Wiley & Sons, 1994.

[19] Response online, the digital magazine from Akzo Nobel Surface Chemistry:
The Science of Flow. Webpage, www.responseonline.com/tech/science.htm.

[20] Simonsen, Lars Ole, Assoc. Prof., Cand. Med., the August Krogh Institute, Copenhagen University.

[21] Solomon, E.P., L.R. Berg, D.W. Martin and C. Villee: *Biology, fourth edition* Saunders College Publishing, 1996

[22] Stryer, Lubert: *Biochemistry, Fourth Edition* W.H. Freeman and Company, New York, 1995.

[23] TA Instruments AR 2000 Rheometer Hardware Manual, Issued September 2000.

[24] Thurston, George B.:
Plasma Release-Cell Layering Theory for Blood Flow Biorheology, 26, 199-214, 1989.

[25] Thurston, George B.: *Rheological Parameters for the Viscosity Viscoelasticity and Thisxotropy of Blood.* Biorheology Vol. 16, pp. 149-162,

1979.

[26] Tracey, Mark C., Richard S. Greenaway, Arindam Das, Paul H. Kaye, and Adrian J. Barnes: *A Silicon Micromachined Device for Use in Blood Cell Deformability Studies*. Biomedical Engineering. Vol. 42 No. 8 August 1995.

[27] Versteeg, H. K. and Malalasekera: *An Introductin to Computational Fluid Dynamics*. Longman Group 1995 Ltd.

[28] Vilastic Scientific, Inc: *Plasma Viscosity and Blood Viscoelasticity*. Webpage, www.vilastic.com/tech10.html.

[29] Walburn, F.J. and D.J. Schneck:
A Constitutive Equation for Whole Human Blood Biorheology, 1976, Vol. 13, pp. 201-210. Pergamon Press.

[30] West, Edward Staunton and Wilbert R. Todd: *Biochemistry* Third Edition, The MacMillan Company, New York, 1961.

[31] Zhang, Jian-Bao, Zhen-Bang Kuang: *Study on Blood Constitutive Parameters in Different Blood Constitutive Equations*. Journal of Biomechanics 33 (2000) 355-360.

Appendix A

Viscosity and Torque Measurements

This appendix is a collection of all the viscometer measurements from the gap size dependency study in the parallel disk geometry. In the figures are shown the viscosity and corresponding torque. The valid torque range for the rheometer is from 0.1 to 2×10^5 μNm, and close to these limits the uncertainty of the measurements increases.

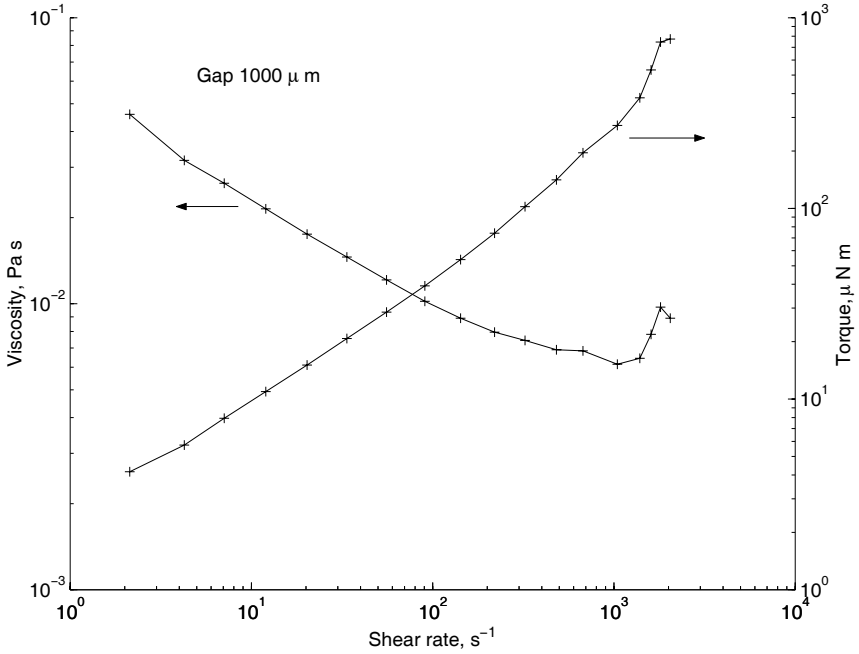

Figure A.1: Gap size measurements: parallel disk geometry.

.

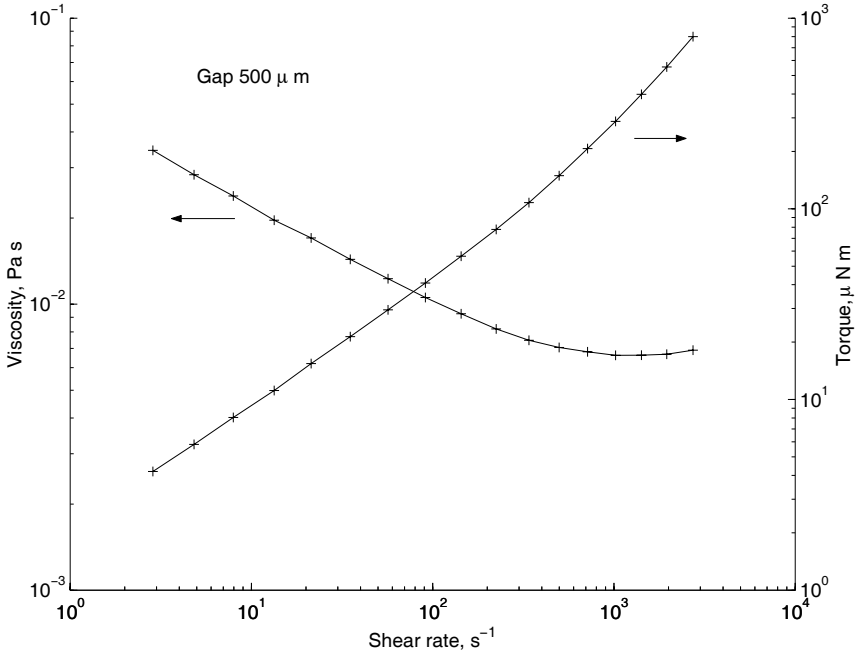

Figure A.2: Gap size measurements: parallel disk geometry.

.

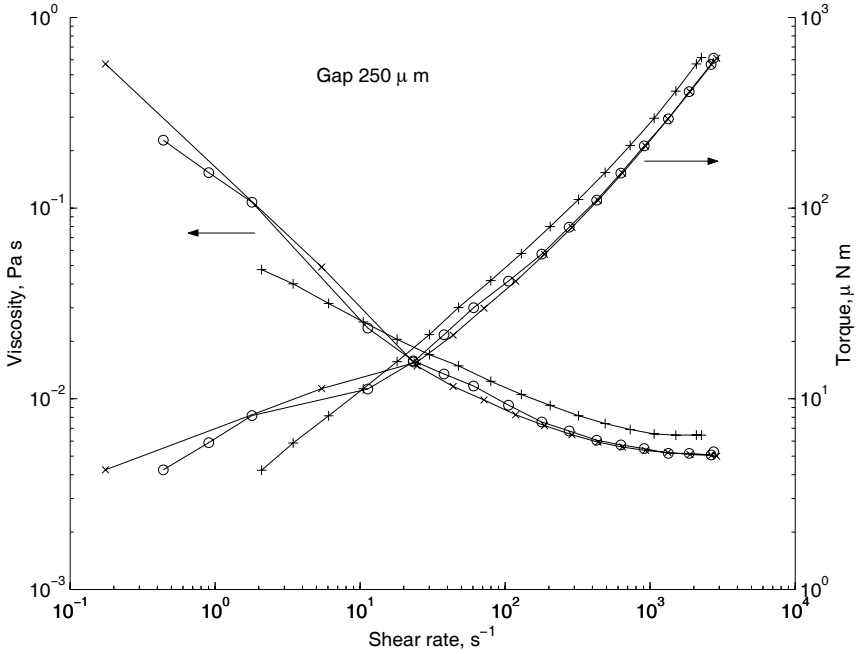

Figure A.3: Gap size measurements: parallel disk geometry.

.

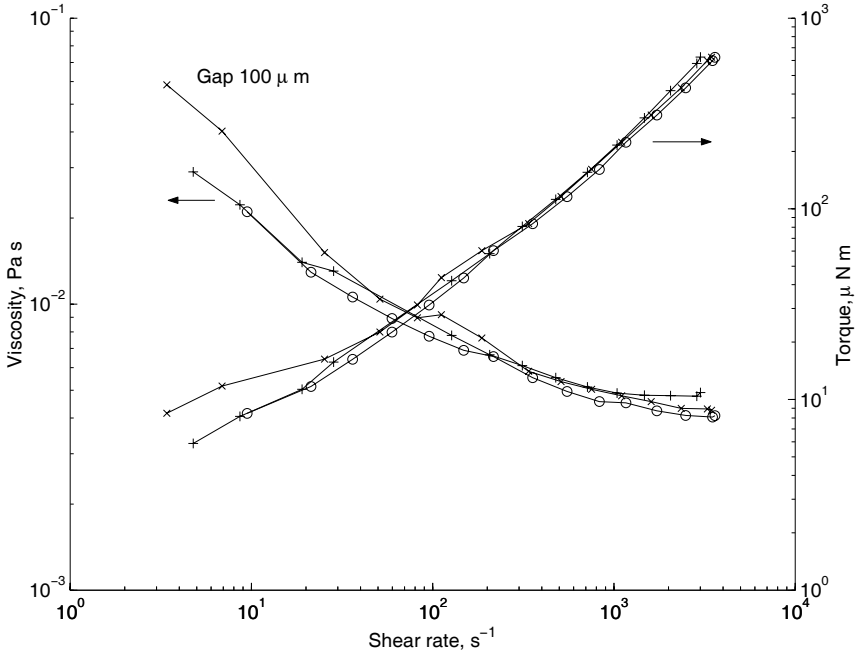

Figure A.4: Gap size measurements: parallel disk geometry.

.

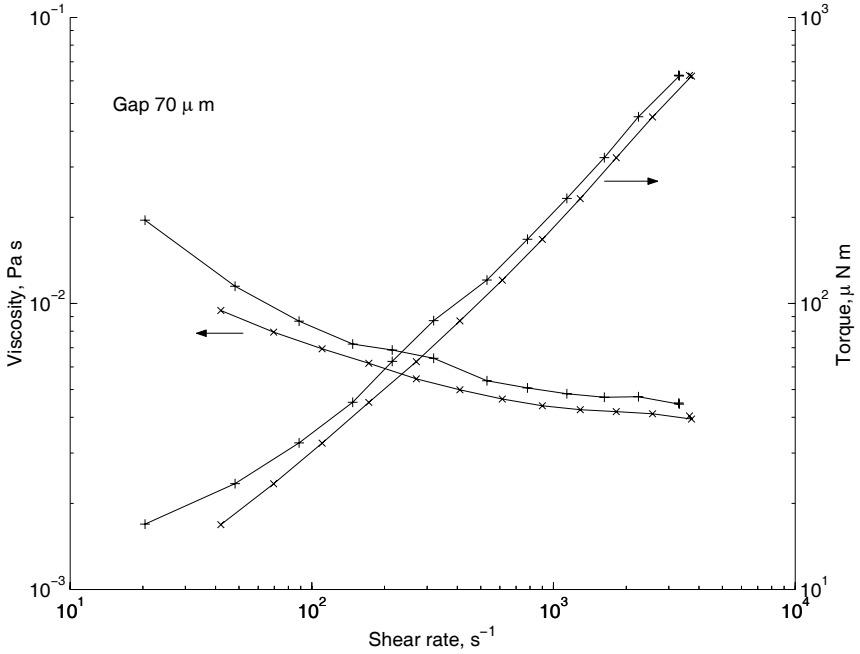

Figure A.5: Gap size measurements: parallel disk geometry.

.

Appendix B

Matlab Source Code: Calculation of Eq. 5.12

Script file:

```
%this program calculates the angular velocity in the
%rz-plane of a parallel disk rheometer
omega=2;    %angular velocity
a=0;        %lower integration boundary
R2=0.04;    %meter
H=0.001;    %meter
el=R2/H     %dimless parameter
R1=0.03     %meter
d=R1/R2;    %fraction between radius of upper plate divided
            %by the radius of the spill, and upper
            %integration boundary in calculation of constants
filename = 'vthetasum_l20_R103.txt' r=linspace(0,1,100);
z=linspace(0,1,50);
%z=1;
testkm=kn; %gets a vector with the first
           % 1000 zeros of the BesselJ_1 function
km=testkm(1:1000); tic; vthetasum=zeros(100, 1);

%vthetasum represents the velocity profiles as a finite sum of n terms
for j=1:50,
    for i = 1:100,
                vtheta=An(km, a, d, el).*BesselJ(1,km.*r(i)).*...
                sinh((km/el).*z(j));
                vthetasum(i, j) = sum(vtheta);
    end
end
```

```
toc;
%figure(1);
hold; plot(r,vthetasum(:,j)); xlabel('r'); ylabel('v_{\theta}')
hold;

fid = fopen(filename,'a');
fprintf(fid, '%s', '%R1 R2 H el');
fprintf(fid,'%12.4f %12.4f %12.4f %12.4f\n', R1, R2, H, el);
fprintf(fid,'%12.4f %12.4f %12.4f %12.4f %12.4f %12.4f %12.4f...
%12.4f %12.4f %12.4f %12.4f %12.4f %12.4f %12.4f %12.4f %12.4f...
%12.4f %12.4f %12.4f %12.4f %12.4f %12.4f %12.4f %12.4f %12.4f...
%12.4f %12.4f %12.4f %12.4f %12.4f %12.4f %12.4f %12.4f %12.4f...
%12.4f %12.4f %12.4f %12.4f %12.4f %12.4f %12.4f %12.4f %12.4f...
%12.4f %12.4f %12.4f %12.4f %12.4f %12.4f %12.4f\n',vthetasum');
fclose(fid);
```

Function files:

```
function y=An(fkm, fa, fd, fel)

y=(2.*fd./fkm.^2.*BesselJ(1,fd.*fkm)...
    -fd.^2./fkm.*BesselJ(0,fd.*fkm))...
    .*2./(fd.*BesselJ(2,fkm).^2.*sinh(fkm./fel));

---------
function y=kn y=load('BesselZero.txt');

% BesselZero.txt contains the first
% 1000 zeroes of Bessel J_1
```

Appendix C

Answer from CFD Research Corporation

This appendix is a fraction of an email from Sekhar Radhakrishnan from CFD Customer Support. On a question about the implementation of the power law(Blood) model I received this answer, which states that the parameters in the non-Newtonian model are in cgs units.

.....

3. Also, the thing to note is that all the values that you enter for viscosity and density for the non-Newtonian viscosity models should be in cgs units, because the code converts these into SI units internally. This is a remnant of the old structured code which will be rectified soon so that the user can enter everything in SI units for these models. I will let you know when this gets fixed. In the meanwhile you can use the cgs units whenever you use the non-Newtonian models. This is true just for the non-Newtonian viscosity models. All other viscosity models take SI units.

....

Best regards.

Sekhar

Sekhar Radhakrishnan Customer Support Group EMAIL:
mailto:support@cfdrc.com WEB: http://www.cfdrc.com TEL:
256-726-4900 FAX: 256-726-4806